ABSTRACT

CUSTOMIZED BORON AND MAGNESIUM-BASED REACTIVE MATERIALS PREPARED BY HIGH ENERGY MECHANICAL MILLING

by
Xinhang Liu

New reactive materials need to be developed having biocidal combustion products. When ignited, such material can add chemical biocidal effects to the common effects of high temperature and pressure. Biocidal combustion products are capable of deactivating harmful spores or bacteria, which can be released by targets containing biological weapons of mass destruction. Research showed that halogens, especially iodine, are effective as biocidal components of reactive material formulations. Recently, magnesium combustion product MgO is also found to have a biocidal effect. Thus, advanced formulations containing both magnesium and iodine are of interest; such formulations are prepared and investigated here.

Reactive materials for biological agent defeat, despite containing iodine, must be stable at room temperature and in ambient conditions, so that they can be handled, mixed with other components, and stored prior to their deployment. Due to the required properties, thermite systems are often considered. However, it is difficult to develop a suitable fuel for such thermite, which generates a lot of energy, reacts rapidly, while remaining safe to handle.

In present work, boron based composites and magnesium are investigated as potential fuels. Thermites are prepared by high-energy mechanical milling the fuels with $Ca(IO_3)_2$ as an oxidizer to produce reactive materials with high iodine concentrations. It is found that boron's natural oxide layer, which hinders the boron ignition can be partially

removed by washing the powder in acetonitrile and toluene. Such washed boron powders remain stable in room conditions. Up to 30 wt% of iodine can be stabilized in a boron matrix in materials prepared by high-energy milling. For a baseline comparison, combustion of magnesium in different oxidizers is investigated. Air is found to be a more effective oxidizer than mixtures of CO, CO_2, and H_2O. Mg oxidation occurs very near to the boiling Mg surface and the rate is controlled by both oxygen diffusion and surface kinetics. A binary Mg·B composite is then prepared by milling; it has a reduced ignition temperature compared to boron. When washed boron serves as a starting material, the composite ignites more readily at high heating rates.

Two thermites, a ternary $B{\cdot}I_2{\cdot}Ca(IO_3)_2$ and a binary $Mg{\cdot}Ca(IO_3)_2$ are prepared and tested. The fuel and oxidizer are mixed on a micron scale. $B{\cdot}I_2{\cdot}Ca(IO_3)_2$ contains 57.6 wt% of iodine and has a lower ignition temperature than $B{\cdot}Ca(IO_3)_2$. $Mg{\cdot}Ca(IO_3)_2$ contains 29 wt% of iodine. At low heating rates, iodine release steps in that material correlate with the decomposition of $Ca(IO_3)_2$. Both thermites burn more rapidly in air than in air-C_2H_2 flame. The iodine release behavior of $Mg{\cdot}Ca(IO_3)_2$ in premixed air-C_2H_2 flame is simulated theoretically and compared with the experimental data using infra-red absorption measurements. The results show that iodine release at a constant rate during the entire particle combustion time is an acceptable assumption for describing the process theoretically. However, the directly measured iodine concentrations are lower than the predictions because of the metastable iodine-bearing combustion products discounted in the calculations.

CUSTOMIZED BORON AND MAGNESIUM-BASED REACTIVE MATERIALS PREPARED BY HIGH ENERGY MECHANICAL MILLING

by
Xinhang Liu

A Dissertation
Submitted to the Faculty of
New Jersey Institute of Technology
in Partial Fulfillment of the Requirements for the Degree of
Doctor of Philosophy in Chemical Engineering

Otto H. York Department of
Chemical and Materials Engineering

December 2019

APPROVAL PAGE

CUSTOMIZED BORON AND MAGNESIUM-BASED REACTIVE MATERIALS PREPARED BY HIGH ENERGY MECHANICAL MILLING

Xinhang Liu

Dr. Edward L. Dreizin, Dissertation Advisor Date
Distinguished Professor, Assoc. Chair, Grad. Stud. Chemical Engineering, NJIT

Dr. Mirko Schoenitz, Committee Member Date
Associate Research Professor, Chemical Engineering, NJIT

Dr. Xianqin Wang, Committee Member Date
Associate Professor, Chemical Engineering, NJIT

Dr. David C. Venerus, Committee Member Date
Professor, Chemical Engineering, NJIT

Dr. Philip M. Guerieri, Committee Member Date
Research Scientist, US Army Research Laboratory, Adelphi, MD

BIOGRAPHICAL SKETCH

Author: Xinhang Liu

Degree: Doctor of Philosophy

Date: December 2019

Undergraduate and Graduate Education:

- Doctor of Philosophy in Chemical Engineering,
  New Jersey Institute of Technology, Newark, NJ, 2019

- Master of Science in Chemical Engineering,
  New Jersey Institute of Technology, Newark, NJ, 2014

- Bachelor of Science in Chemical Engineering,
  Lanzhou University, Gansu, P. R. China, 2011

Major: Chemical Engineering

Publications:

Liu, X., A.Sims, C. Murzyn, N. G. Glumac and E. L. Dreizin (2019). “Iodine Release by Combustion of Composite Mg·Ca(IO3)2 Powder.” Combustion Science and Technology, 1-13.

Liu, X., M. Schoenitz and E. L. Dreizin (2019). "Preparation, Ignition, and Combustion of Magnesium-calcium Iodate Reactive Nano-composite Powders." Chemical Engineering Journal 359: 955-962.

Liu, X., M. Schoenitz and E. L. Dreizin (2018). "Combustion of Mg and Composite Mg·S Powders in Different Oxidizers." Combustion and Flame 195: 292-302.

Liu, X., K.-L. Chintersingh, M. Schoenitz and E. Dreizin (2018). "Reactive Composite Boron–Magnesium Powders Prepared by Mechanical Milling." Journal of Propulsion and Power 34: 1-8.

Liu, X., J. Gonzales, M. Schoenitz and E. L. Dreizin (2017). "Effect of Purity and Surface Modification on Stability and Oxidation Kinetics of Boron Powders." Thermochimica Acta 652: 17-23.1

Liu, X., M. Schoenitz and E. L. Dreizin (2017). "Boron-based Reactive Materials with High Concentrations of Iodine as a Biocidal Additive." Chemical Engineering Journal 325: 495-501.

Monk, I., R. Williams, **X. Liu** and E. L. Dreizin (2015). "Electro-Static Discharge Ignition of Monolayers of Nanocomposite Thermite Powders Prepared by Arrested Reactive Milling." Combustion Science and Technology 187(8): 1276-1294.

Wang, S., **X. Liu**, M. Schoenitz and E. L. Dreizin (2017). "Nanocomposite Thermites with Calcium Iodate Oxidizer." Propellants, Explosives, Pyrotechnics 42(3): 284-292.

Presentations:

X, Liu., M. Schoenitz and E. L. Dreizin (2016). "Boron-based Reactive Materials with High Concentrations of Iodine as a Biocidal Additive" Presented at Defense Threat Reduction Agency (DTRA), Waterford, VA. (Poster)

X, Liu., S, Wang,. M. Schoenitz and E. L. Dreizin (2016). "Nanocomposite Thermites with Calcium Iodate as an Oxidizer." AIChE Annual Meeting, San Francisco, CA

X, Liu., S, Wang,. M. Schoenitz and E. L. Dreizin (2017). "Effect of Flow Conditions on Burn Rates of Magnesium and Magnesium-Containing Reactive Material Particles. " AIChE Annual Meeting, Minneapolis, MN.

X, Liu., M. Schoenitz and E. L. Dreizin (2018). "Ignition and Combustion Mechanisms of Mg-$Ca(IO_3)_2$ Reactive Nanocomposites" AIChE Annual Meeting, Pittsburgh, PA.

X, Liu., M. Schoenitz and E. L. Dreizin (2017). "Combustion of Magnesium Particles in Different Oxidizing Environments" MRS Fall Meeting, Boston, MA.

谨以此论文献给我的父亲刘时权，我的母亲王晓玲。
感谢你们一直以来的支持，鼓励和包容。

This thesis is dedicated to my beloved father Shiquan Liu, mother Xiaoling Wang.

For their support, encouragement and unconditional love.

ACKNOWLEDGMENT

First of all, I would like to express my gratitude to Prof. Edward Dreizin for his continuous guidance and support. Whenever I encountered difficulties in my research, you were always been there and helped me with your immense knowledge. You are not only my advisor in research, but also my life mentor who teaches me how to treat the others with lov e and patience. I am truly blessed by having you as my dissertation advisor.

A special thanks to Prof. Mirko Schoenitz. Thank you for providing your brilliant comments and suggestions. You enlightened my research direction with your professional guidance. Also, I really appreciate your help with my analysis skills.

I would like to thank the committee members: Prof. Xianqin Wang, Prof. David Venerus, Dr. Philip Guerieri for attending my PhD thesis defense. All your questions and comments have improved my thesis a lot.

Finally, I would like to extend my appreciation to my colleagues: Amy Corcoran, Ani Abraham, Hongqi Nie, Rayon Williams, Ian Monk, Siva Kumar, Song Wang, Oleg Lagoviyer, Daniel Hastings, Kerri-Lee Chintersingh, Ci Huang, Mehnaz Mursalat, Ashvin Vasudevan, Shomik Mukhopadhyay, Elif Senyurt. It is my pleasure to work with you. The friendships and memory will be valued through my lifetime. I especially want to express my thanks to Rayon Williams, Song Wang and Kerri-Lee Chintersingh who showed me all the details of the experiments. I would have a rough time without your help with my researches.

TABLE OF CONTENTS

TABLE OF CONTENTS
(Continued)

Chapter **Page**

TABLE OF CONTENTS
(Continued)

Chapter **Page**

TABLE OF CONTENTS
(Continued)

Chapter **Page**

LIST OF FIGURES

LIST OF FIGURES
(Continued)

LIST OF FIGURES
(Continued)

LIST OF FIGURES
(Continued)

LIST OF FIGURES
(Continued)

LIST OF FIGURES
(Continued)

LIST OF TABLES

CHAPTER 1

INTRODUCTION

1.1 Background

Agent defeat weapons are designed to target and destroy stockpiles of chemical or biological weapons without dispersing or releasing them to surrounding areas (Eneh 2012). Bio-agent defeat often relies on halogens released by an explosive charge. Iodine-containing additives to energetic materials are shown to be effective in producing biocidal combustion products (He, Zhang, and Shreeve 2013a; Vo et al. 2013). Harmful spores and bacteria can be deactivated by both thermal and chemical effects when these additives are included in formulation of explosive charges (Nakpan et al. 2018). A quantitative model was proposed to link both effects to the rate of destruction of aerosolized spores serving as surrogate of anthrax (Wang, Schoenitz, et al. 2018).

Extensive studies focused on development of new materials capable to serve as fuel additives and releasing the biocidal products (Abraham, Schoenitz, and Dreizin 2013; Wang et al. 2016; Wang et al. 2017b; Smith, McCollum, and Pantoya 2016; Clark and Pantoya 2010; Farley and Pantoya 2010; Wang, Kline, et al. 2018; Wu et al. 2017; Wang et al. 2015). Advanced energetic materials for biological agent defeat applications must be stable at room temperature and in ambient conditions, so that the material can be handled, mixed with other components, and stored prior to its deployment. A high burn rate is also required to release heat and iodine quickly (Henderson et al. 2015). Targeting these characteristics, novel thermite compositions and alloys with high iodine concentration have been synthesized and characterized (Wang et al. 2015; Ruz-Nuglo and Groven 2015b;

Oxley et al. 2017; Wang et al. 2016; Zhang, Schoenitz, and Dreizin 2010a; Wang et al. 2017b).

For thermites generating biocidal products, various iodine bearing materials can serve as potential oxidizers, including I_2O_5 and metal iodates (Smith, McCollum, and Pantoya 2016; Oxley et al. 2017; Wang, Kline, et al. 2018; Clark and Pantoya 2010; Wang et al. 2017b; Feng et al. 2013; Farley and Pantoya 2010). However, I_2O_5 is hygroscopic and make the thermites very hard to handle in ambient air. Among different iodates, calcium iodate was reported to be more stable than others, remaining intact at 60 ^oC and 75% humidity, making it a suitable oxidizer for the thermite compositions (Ruz-Nuglo and Groven 2015b).

Metals serve as fuels in thermites. Due to high volumetric energy density of metal oxidation, metals and metalloids, such as boron or magnesium, are widely used in energetic applications as fuels or fuel-additives (King 1972, 1982; Hsieh et al. 1991; Arnold and Rottenkolber 2009; Young et al. 2012; Young et al. 2013). This explains why metal combustion attracted significant interest and was widely studied in recent decades. Boron's gravimetric and volumetric heats of combustion exceed those of other metals (Gremyachkin, Istratov, and Leipunskii 1979; Karmakar et al. 2013); it is thus attractive as a fuel for a broad range of energetic formulations, including air-breathing propellants and enhanced blast explosives. However, boron is known to have long ignition delays and low burn rates (Ulas, Kuo, and Gotzmer 2001; Hussmann and Pfitzner 2010; Maček 1973; Maček and Semple 1971; Yeh and Kuo 1996; Young et al. 2009) making it difficult to take advantage of the released combustion heat in many practical devices. Alloys or thermite systems using boron as a fuel were explored, in particular, focusing on improving boron combustion and ignition rates and reducing its ignition delays (Xi, Liu, Wang, Liang, Li, et al. 2014; Liu et al. 2014; Rosenband and Gany 2011). It was also found that boron-iodine alloys and some boron-containing thermite compositions may generate biocidal combustion products; such materials release halogen upon heating, which is of interest for destroying aerosolized harmful biological spores or bacteria, e.g., for biological weapon defeat applications (Wang et al. 2017b; Wang et al. 2016).

In a recent study, Mg combustion products were also found to have a biocidal effect, likely due to the generated smoke of ultrafine MgO particles (Nakpan et al. 2018). Magnesium ignites readily and typically burns in a vapor phase. It releases less heat than boron or aluminum, and thus it is mostly used in pyrotechnic devices (Pivkina et al. 2004; Price 1984a), where the rate of ignition is important rather than the released heat of reaction. However, due to the biocidal effect of MgO, Mg can potentially serve as a fuel or fuel additive in biocidal thermites and alloys; such material could combine the bio-defeat effects of halogens and MgO. Combustion mechanisms of magnesium were studied extensively (Dreizin 2000; Legrand et al. 2001; Florko et al. 1986; Valov, Kustov, and Shevtsov 1994); the experimental efforts were mainly focused on coarse size magnesium particles. In biocidal material, due to the requirement of reactivity, fine size fuel is preferred. Combustion mechanism of fine Mg becomes crucial for understanding more complex, Mg-based biocidal reactive material compositions.

1.2 Challenges

To develop a high-performance biocidal thermite, boron is attractive to serve as a fuel due to its high energy density. However, boron, as other metals and metalloids, has a naturally grown surface oxide layer. Commonly, this oxide is hydrated and forms boric acid. The surface coating hinders oxygen diffusion to boron surface, thus making it difficult to ignite boron particles (Chen et al. 1991; Foelsche, Burton, and Krier 1999; Yeh and Kuo 1996). Alternatively, diffusion of boron towards the external surface may similarly be hindered, also causing an ignition delay. Mechanism and kinetics of oxygen diffusion to boron surface have been studied (Yeh and Kuo 1996; King 1972; King 1973; Yeh et al. 1997). Despite the efforts, mechanism of boron combustion remains unclear. For example, recent work suggested that two oxidation regimes occurred depending on the surrounding temperature (Liang et al. 2017). Oxygen diffused through oxide layer to boron surface at low temperature, after temperature reached 700 ^{o}C, interior boron particle became porous, and oxygen diffused through oxide layer to both boron particle surface and interior. Since the oxide layer is an important obstacle to boron ignition, lots of efforts have been made to reduce initial oxide layer by using metal additives or surface coatings (Xi, Liu, Wang, Liang, Li, et al. 2014; Liu et al. 2014; Rosenband and Gany 2011; Xi, Liu, Wang, Liang, and Zhou 2014). Also, other simple and practical approaches used water or acetonitrile to dissolve the oxide layer by washing boron powders; the results showed that the ignition of boron improved (Conkling and Mocella 2010; Chintersingh, Schoenitz, and Dreizin 2016). However, the washed boron normally is unstable and re-oxidizes quickly when it is exposed to air. Thus, an approach is needed to wash boron effectively and stabilize its surface after it has been cleaned of boric acid and boron oxide.

Magnesium oxidation products recently found to be an effective biocidal material at short exposure times (Nakpan et al. 2018). Magnesium can be used as a fuel additive to reduce ignition delay of boron. Thus, magnesium as a component of a new reactive material offers dual benefits: it ignites and burns more readily upon heating than other metals, and its combustion products are biocidal. Thus, magnesium-based alloys or thermite systems could be potential candidates for application involving biological agent defeat. Such materials have never been studied before and are addressed in this dissertation. Combustion mechanism of magnesium was studied extensively by C.K. Law (Law and Williams 1974; Law 1976, 1973). It was focused on magnesium particles with size coarser than ca. 100 µm. However, fine magnesium powders are generally used in applications. Recently, combustion behavior for fine magnesium in air-acetylene and hydrogen-oxygen flame was explored (Wang, Corcoran, and Dreizin 2015; Corcoran et al. 2015). Since most applications employ magnesium burning in turbulent flows and using air as an oxidizing environment, it is essential to explore combustion of fine magnesium powders under different flow conditions. Using air as an oxidizing medium for magnesium powder is also of significant interest.

Further, for agent defeat applications, a high iodine (or other halogen) concentration is desired in a reactive material (Henderson et al. 2015; Wang et al. 2017b). Boron-based thermite compositions, especially, with calcium iodate as an oxidizer, were found to be suitable as reactive materials for agent defeat applications recently (Wang et al. 2017b). By mechanically milling the material, iodine could be stabilized in the metal matrix (Wang et al. 2016). The calcium iodate and boron thermite system provides a more rapid iodine release comparing to mechanically alloyed boron-iodine powder. It was also observed that boron-calcium iodate composite is more stable in room air than a similar thermite using aluminum as a fuel. Unfortunately, experiments with calcium iodate – containing composites showed that the boron-based thermite becomes unstable when concentrations of calcium iodate higher than 80 wt% are introduced into the system (Wang et al. 2017b). Characterizing this stability and improving it while maximizing the amount of iodine available in the reactive material is another important challenge.

Finally, quantifying the biocidal effect of combustion of different reactive materials is an important challenge. Aerosolized spores are being destroyed by their exposure to both elevated temperatures and specific chemicals released by the combustion products. A quantitative model is designed to predict the rate of inactivation of spores and bacteria as a function of temperature and iodine concentration. The temperature profile can be obtained by simulating the heat transfer during reactive material combustion and verifying with laboratory experimental data (Wang, Mohan, and Dreizin 2016; Wang, Schoenitz, and Dreizin 2017). Predicting iodine concentration profile requires one to assume how iodine is released by burning particles. In previous work, it was simply assumed that iodine is released at a constant rate during the entire particle burn time. However, no experimental iodine concentration data has been available to validate this assumption. ICP-MS is often used to measure iodine concentration (Andrey et al. 2001; Judprasong, Jongjaithet, and Chavasit 2015), however, it is not available for measuring iodine concentration at high temperature as a function of time in millisecond scale. Recently, tunable diode laser absorption spectroscopy has been developed as a method suitable of real time measurements of iodine concentration (Murzyn et al. 2018). Combining this new diagnostics with the experimental setup used to develop the model (Wang, Schoenitz, et al. 2018) is proposed as a viable approach to justify or improve the above assumption and thus increase fidelity of the proposed model.

1.3 Objectives

This work has three main objectives.

The first goal is to remove or mitigate the effect of the natural boron oxide layer to enhance boron ignition and combustion as a fuel combined with calcium iodate to form a thermite generating biocidal products.

In one approach, dissolution of natural boron oxide layer was also studied using different experimental protocols. Acetonitrile, toluene and hexane were used as washing solvent in this path, ultrasonic was the mixing method. Stability, oxide composition and oxidation kinetics of boron treated by different methods were explored and compared to a commercial 99% pure boron. In another approach, adding a readily oxidizing magnesium is explored. A mechanically alloyed Mg·B powder was prepared by high-energy mechanical milling under different conditions. Ignition, oxidation, combustion and explosion behaviors of materials were tested, and effects of different milling condition on B·Mg alloys were explored.

The second goal is to increase the iodine concentration in $B \cdot Ca(IO_3)_2$ thermite system.

Mechanically alloyed boron-iodine powders with different compositions were prepared by high-energy mechanical milling, and the most stable material was then milled with calcium iodate to make boron-iodine-calcium iodate ternary system. $B \cdot I_2 \cdot Ca(IO_3)_2$ was compared with $B \cdot Ca(IO_3)_2$ in terms of ignition and combustion performance.

The third goal is to explore magnesium and magnesium based biocidal material's combustion behavior and mechanism in different oxidizing environments and flow conditions.

Fine magnesium and mechanically milled $Mg{\cdot}S$ powders were prepared and burned in air, CO_2-H_2O or H_2O environments. Flow conditions were varied in air to produce a laminar or turbulent flow patterns. Combustion behavior under such conditions was analyzed and correlated with powder particle size distribution. Combustion of $Mg{\cdot}Ca(IO_3)_2$ was also studied and the iodine release is quantified to enable quantitative modeling of biocidal effects achieved using these new materials.

CHAPTER 2

EFFECT OF PURITY AND SURFACE MODIFICATION ON STABILITY AND OXIDATION KINETICS OF BORON POWDERS

2.1 Abstract

A commercial 95-% pure boron was ultrasonicated in acetonitrile and then in toluene to remove the surface layer of boron oxide and boric acid. The powder suspended in acetonitrile forms stratified layers, with the bottom layer containing most of the material with the least amount of boron oxide and boric acid. The surface of the processed boron powder was modified with a protective layer, making it more stable in room temperature humid oxidizing environment than the reference 95-% pure commercial boron. The stability of different powders was characterized using isothermal calorimetry employing a thermal activity monitor TAM III with a perfusion ampoule. Oxidation of the surface modified boron powders was studied using thermal gravimetry and compared to oxidation of both 99 and 95-% pure commercial powders. At room temperature, the 99-% pure boron powder was the most stable. Upon heating, the 99-% boron begins oxidizing at a lower temperature than all the 95-% pure powders. However, the apparent activation energy of oxidation at elevated temperatures obtained using a model-free isoconversional methodology for the 95-% pure powder processed in both acetonitrile and toluene is lowest among all tested powders and is close to 100 kJ/mol. It is expected that the latter powder is the most attractive as a fuel, which will be characterized by the shortest ignition delays.

2.2 Introduction

Boron is a thermodynamically attractive fuel for propellants, explosives, and pyrotechnics (King 1972, 1982; Hsieh et al. 1991; Arnold and Rottenkolber 2009; Young et al. 2012; Young et al. 2013). However, boron fuel performance is hampered by long ignition delays caused by slow heterogeneous reactions involving removal or modification of the natural oxide layer coating boron particles (Chen et al. 1991; Foelsche, Burton, and Krier 1999; Yeh and Kuo 1996). Despite extensive research spanning several decades, the processes governing boron ignition delays are poorly understood. These processes involve oxidation of heated boron powders, which is rate-limited by transport of reactants through the evolving boron oxide coating. Surprisingly, there are only limited studies addressing kinetics of such oxidation (Chen et al. 2009), while multiple efforts focused on modifying the surface of boron powders, e.g., by using reactive additives (Xi, Liu, Wang, Liang, Li, et al. 2014) or coatings (Liu et al. 2014; Rosenband and Gany 2011). The simplest approach involves washing boron in water prior to its use (Conkling and Mocella 2010), which removes water-soluble oxide film; however, such water-washed boron is unstable in air and re-oxidizes quickly. Recently, it was shown that washing boron powder in acetonitrile followed by rinsing in toluene yields a powder that has a much thinner oxide coating, is stable in air, and ignites faster than regular commercial boron powder (Chintersingh, Schoenitz, and Dreizin 2016). In this work, the methodology of boron surface modification by organic solvents is refined and oxidation kinetics are compared for commercial boron powders of different purities, as well as for a powder with modified surface.

2.3 Materials

An amorphous boron powder, SB95 by SB Boron, which is nominally 95 % pure was used both as a reference material and as a starting component to prepare powders with modified surfaces; this material is referred to as B_{95}. A nominally 99 % pure powder representing a mix of amorphous and crystalline boron, provided by Alfa Aesar, also served as a reference material; it is referred to as B_{99}.

Powders with modified surfaces were prepared by washing B_{95} powder with acetonitrile (99.5% pure by Alfa Aesar) and toluene (99.5% by Chempur). A 9-g load of a boron powder (B_{95}) was placed in a 250-mL beaker together with 170 mL of acetonitrile. The mixture was agitated using a 20-kHz Branson 910BC ultrasonic system with a titanium horn. The horn with a 5.08 cm (2 in) diameter vibrating surface was inserted in the liquid and operated at 75% of its maximum power. During sonication the suspension stratified forming two layers with a lighter-colored layer at the top. In preliminary experiments, the powder samples were collected from each of the two layers. Each sample was then heated in a thermo-gravimetric (TG) analyzer, TA Instruments model Q5000IR, with the objective of quantifying the mass loss due to de-hydration of boric acid. The samples were heated in argon to 400 °C at 5 °C/min. It was observed that the measured mass loss is substantially lower for the powder recovered from the bottom layer; the bottom layer generally also contained more powder by mass. Further process optimization was aimed to achieve the most attractive powder in the bottom layer, which can be readily separated from the rest of the sample. It was observed that the mass loss from the powder collected from the bottom layer was minimized after 3 minutes of sonication, when the stratified layers were well separated. Powder was agglomerated after longer sonication time; the mass loss measured in TG experiment also increased. Thus, 3 minutes was considered as the optimized sonication time.

To recover the material, the stratified layers were separated; powder from each layer was collected by centrifugation and dried in argon. In addition, the acetonitrile separated by centrifugation from each layer, was gathered and dried in argon. A solid residue was collected for ensuing TG measurements. All samples, including reference powders, were characterized by TG, as illustrated in Figure 2.1.

As received powder B_{95} lost 6.0% of its mass at 250 °C, consistent with previous observations (Chintersingh, Schoenitz, and Dreizin 2016). This two-step mass loss is associated primarily with dehydration of $B(OH)_3$ (Sevim et al. 2006). The powder collected from the bottom layer of the stratified sample exhibited the lowest mass loss upon heating (ca. 0.8%), suggesting the smallest amount of hydrated boron oxide. The powder collected from the top layer lost about 9.6% of its mass, suggesting that this material contained disproportionally large fraction of the boron hydroxide. The washed powder comprising samples from both top and bottom layers mixed together lost about 3.3% of its mass (not shown in Figure 2.1), which is comparable to the mass loss reported for the boron washed in acetonitrile in Ref. (Chintersingh, Schoenitz, and Dreizin 2016). Finally, the residue collected from the dried acetonitrile lost more than 40 % of its mass, suggesting that it contained 91% of $B(OH)_3$.

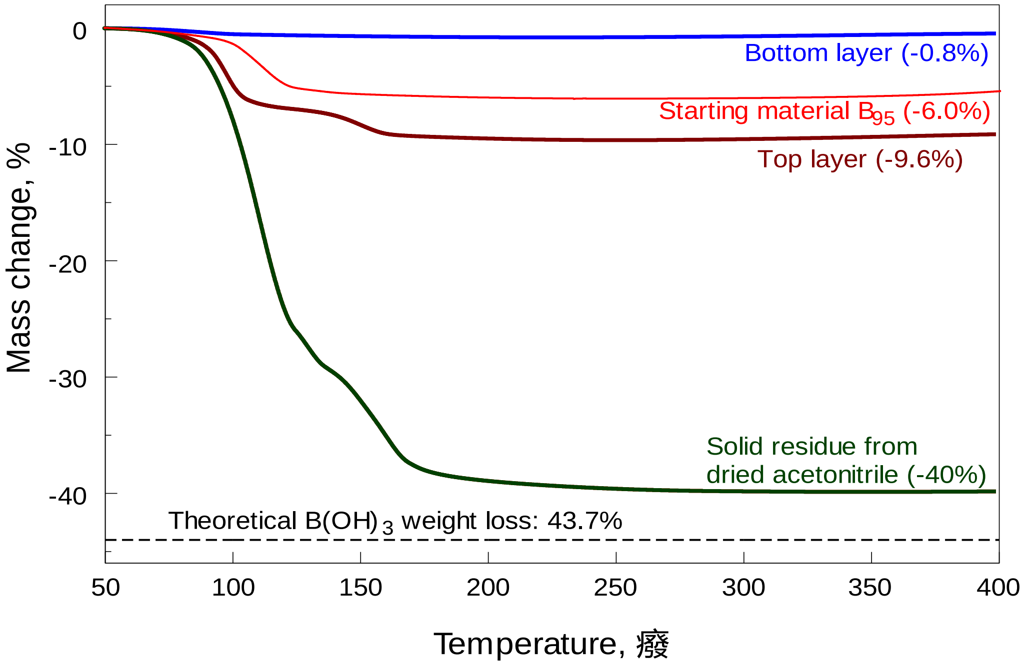

Figure 2.1 TG traces for different boron samples heated in argon at 5 °C/min

The effect of additional washing cycles on the measured mass loss of boron samples was further investigated. The processing involved the powder recovered from the bottom layer of the stratified sample. This powder was separated from acetonitrile by centrifugation. It was then mixed with 170 mL of fresh acetonitrile in the 250-mL beaker. It was observed that during the second wash, the suspension stratified again after 2 minutes of sonication. The powder from the bottom layer was again separated, dried, and exhibited a mass loss reduced further compared to the sample washed once. The twice-washed powder was mixed with acetonitrile and washed for the third time. No stratification was observed and no further mass loss reduction in TG experiments was noted. Therefore no additional washing cycles were attempted. The powder recovered was of black color. It was removed from acetonitrile by centrifugation and then dried in argon for 12 hours. This material washed in acetonitrile three times is further referred to as B_{ACN}. The mass loss measured for this sample by TG was 0.15%. Previous work suggested that an additional processing boron in toluene makes it more stable in air (Chintersingh, Schoenitz, and Dreizin 2016). Respectively, samples of B_{ACN} were mixed with 170 mL of toluene and sonicated for 2 minutes. After sonication, the solid phase in the mixture settled down quickly. Once again, centrifugation was used to extract the solid phase from the suspension. The recovered powder was dried in argon for 12 hours; it is referred to as B_{Tol}. The mass loss measured for B_{Tol} in TG experiments was close to that measured for B_{ACN}. A set of two commercial powders along with B_{ACN} and B_{Tol} were used in following experiments. The materials are listed in Table 2.1 along with mass loss measured for each of them using TG runs, similar to those described above and illustrated in Figure 2.1.

To further characterize the materials used here, SEM images and elemental analysis were obtained using a Field Emission Scanning Electron Microscope with Oxford Energy Dispersive Spectroscopy detector, FESEM-EDS, model LEO 1530. The SEM images for B_{tol} are shown in Figure 2.2, while B_{95} has been shown elsewhere (Chintersingh, Schoenitz, and Dreizin 2016). Agglomeration appears in both, B_{tol} and B_{95}. Results of elemental analysis of an area covering many particles, and taken as representative of the whole sample, are also shown in Table 2.1. Oxygen and magnesium are found in all samples, but in B_{95} based samples, the amount of magnesium is much higher than in B_{99}. The amount of oxygen was reduced after washing. In addition, the surface areas are shown measured for each powder using a Quantachrome NOVA 3000a High Speed Gas Sorption Analyzer. The degassing condition was set to one hour at 200 ^{o}C. The surface areas for all powders are comparable to one another, although B_{95} appears to be the most agglomerated with the lowest surface area.

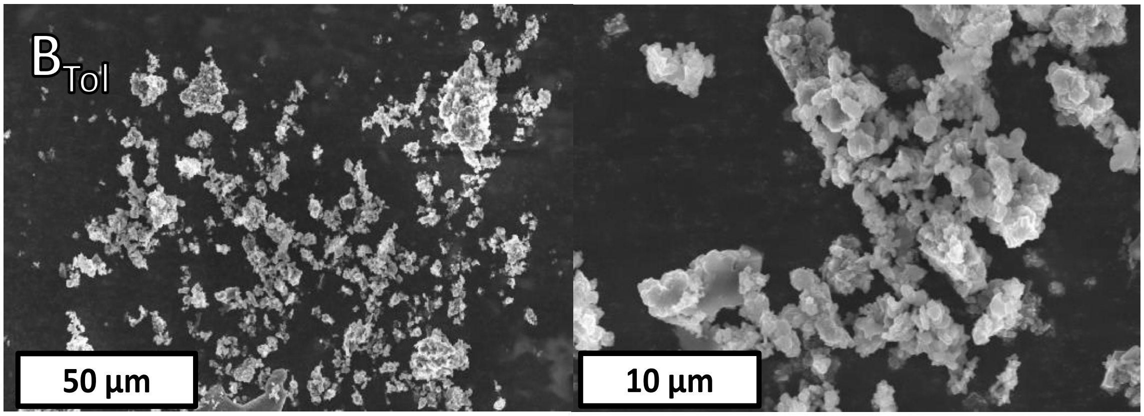

Figure 2.2 Secondary electron images for B_{tol}.

Table 2.1 Materials Used in Experiments

Sample ID	Preparation	TG mass loss, %	Surface Area, m^2/g	Oxygen, wt-%	Magnesium, wt-%
B_{99}	99% pure boron, obtained from Alfa Aesar	0.4	12.08	1.82 ± 0.17	0.22 ± 0.05
B_{95}	95% pure boron, obtained from SB Boron	6.0	5.81	7.07 ± 0.18	0.67 ± 0.04
B_{ACN}	B95 washed three times in acetonitrile	0.15	8.51	5.68 ± 0.28	0.73 ± 0.07
B_{Tol}	B_{ACN} washed in toluene	0.14	9.98	4.12 ± 0.22	0.91 ± 0.07

To verify the reproducibility of the present processing for boron powder, several batches of B_{ACN} were prepared. For all of them, TG measurements were made showing the mass loss to be reproducible within ±0.1 %.

2.4 Material Stability

Prepared and reference materials were exposed to humid oxidizing environments at relatively low temperatures of 40 and 70 °C, which could occur in applications during storage and handling. A TAM III analyzer by TA Instruments equipped with a perfusion ampoule was used for these experiments. The results are summarized in Table 2.2. For both 40 and 70 °C temperature settings, the gas environment consisted of an O_2/Ar mixture with the mole ratio of 1/4. Water vapor was mixed in with the oxygen flow to achieve relative humidity of 70%. The samples were first thermally equilibrated in a dry argon flow at a pre-selected temperature. Then, oxygen mixed with water vapor was introduced. The samples were initially hydrated absorbing water and exhibiting an exothermic peak. The hydration is expected to involve primarily boron oxide coating the powder particles. The hydration peak was stronger for the samples with thicker oxide layer, for which more boron oxide could be converted to boric acid. The exothermic peak corresponding to absorption of moisture was also stronger for a B_{95} sample that was initially dried, so that the water was removed from its oxide layer, while the amount of boron oxide was not reduced, unlike for the washed samples B_{ACN} and B_{Tol}.

Once the water absorption process ended, the measured heat flow did not return to the original zero level; instead, a finite, nearly constant heat flow was measured, caused by a slow reaction of the sample in the humid oxidizing environment. This steady heat flow depends on the sample, indicating differences in the material stabilities. A higher steady heat flow rate indicates a less stable sample, which ages faster and vice versa. The measurements are presented in Figure 2.3. The exothermic peaks corresponding to the sample hydration are cut to better show the steady heat flows measured after the hydration peaks. For B_{Tol} trace, shown in Figure 2.3, after a steady heat flow rate is measured, the oxygen and water vapor flows are turned off, so that the sample dehydrates in argon. This causes an endothermic peak partially shown in Figure 2.3. The measurement sequence involving shutting down oxygen and water vapor flows and causing the endothermic peaks was repeated for some but not all samples. The amounts of heat absorbed in the recorded endothermic dehydration peaks are close to those released in the hydration peaks for the same materials.

Table 2.2 gives a summary of all the measured heats of hydration and dehydration reactions and of values of the measured steady heat flow rates for all samples. Clearly, both B_{ACN} and B_{Tol} show lower values of heat desorbed/adsorbed during their hydration/dehydration, respectively, compared to B_{95} and even to B_{99}. This suggests a smaller amount of oxidized boron in these, surface modified powders, compared to commercial materials. Using the measured heat effect of water absorption and assuming that all boron oxide was hydrated at 70 °C, forming $B(OH_3)$, the amount of boron oxide present in each sample was calculated accounting for the measured specific surface (Table 2.1), density of B_2O_3, and heats of formation of B_2O_3, $B(OH)_3$, and H_2O (Chase 1998). These calculated values are also shown in Table 2.2. The thickness close to 4 nm obtained for the commercial B_{95} is reasonable. It is interesting to see how much the oxide thickness is reduced for the processed powders, B_{ACN} and B_{Tol}.

The measured specific surface does not appear to correlate with the rate of steady reaction observed at constant temperatures of 40 and 70 °C for different samples. The most reactive sample appears to be B_{95}, which has the lowest specific surface and the thickest oxide layer. Despite a greater surface area and thinner oxide layers, materials with modified surfaces, B_{ACN} and B_{Tol} are less reactive and thus more stable at these relatively low temperatures. Interestingly, B_{Tol} is more stable than B_{ACN}, which is in agreement with preliminary observations reported earlier (Chintersingh, Schoenitz, and Dreizin 2016). The most stable material is B_{99} according to the present measurements.

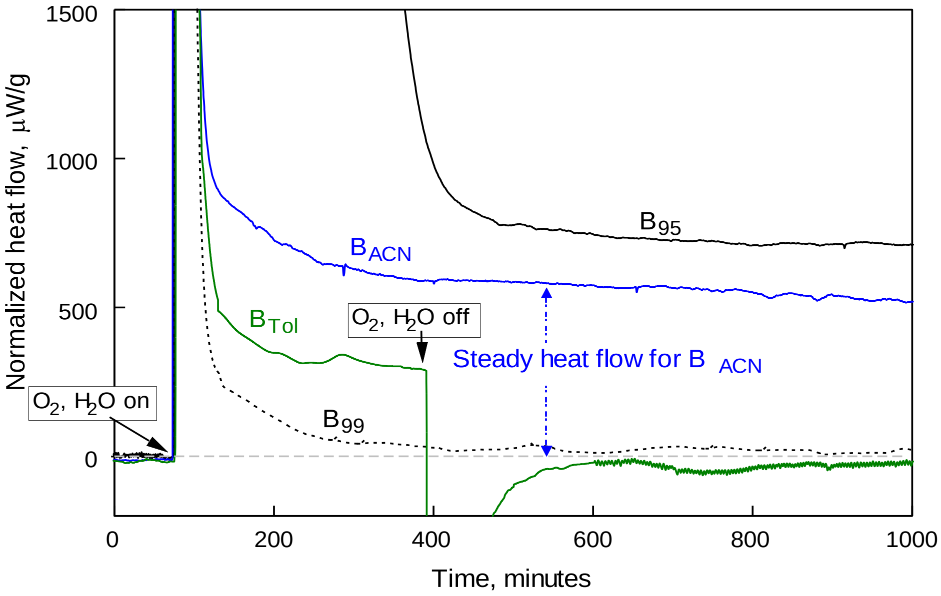

Figure 2.3 Heat flow traces measured in TAM III experiments at 70 °C.

Table 2.2 Summary of TAM III Measurements Performed with Different Materials at 40 and 70 °C

Material	Measurements at 70 °C				Measurements at 40 °C	
	Hydration heat (J/g)	Dehydration heat (J/g)	Steady heat flow (μW/g)	Calculated oxide thickness (nm)	Hydration heat (J/g)	Steady heat flow (μW/g)
B_{99}	29.6	26.5	40	0.36	25.63	6.9
B_{95}	88.42				33.5	140
Dried B_{95}	156.49		712	3.96		
B_{ACN}	18.47		525	0.32	9.92	100
B_{Tol}	11.86	11.95	318	0.18	11.73	90

Additionally, the effect of aging on the prepared samples was assessed by exposing them to argon and air for several days and repeating the TG measurements, as shown in Figure 2.1 and in Table 2.1. Specifically, B_{ACN} sample was dried in argon for 12 hours and then exposed to argon for 7 days or to laboratory air for 20 days prior to the TG measurements. The mass loss measured in the TG experiments, where the samples were heated to 400 °C at 5 °C/min did not change as a function of the sample age.

2.5 Oxidation at Elevated Temperatures

Powders were oxidized in a TG analyzer (TA Instruments model Q5000IR). The materials were heated up to 900 or 1000 °C at 2, 5, and 10 °C/min. Gas flows were set to 20 mL/min for oxygen (sample flow) and 10 mL/min for argon (balance purge flow). TG traces recorded at 2 °C/min for all materials are presented in Figure 2.3. The onset of the sharp mass gain step occurs at a substantially lower temperature for B_{99} compared to other samples, which is unexpected based on its lower reactivity shown by TAM III measurements (cf. Figure 2.3 and Table 2.2). At least partially, the lower-temperature onset of oxidation may be explained by a greater specific surface measured for B_{99}, see Table 2.1. However, the difference in the specific surface does not result in the appreciable difference in the onset temperature of oxidation between B_{95} and surface modified B_{ACN} and B_{Tol}. The oxidation onset occurs at nearly the same temperatures for all three powders based on the 95-% pure boron, B_{95}, B_{ACN}, and B_{Tol}. However, the mass loss due to dehydration of boric acid is only observed for B_{95}, in agreement with data in Figure 2.1 and Table 2.1. The mass gains observed by the end of the present heating program were higher for B_{ACN}, and B_{Tol} than for B_{95}. This could be associated with the reduced initial oxide layers for the surface-modified powders as well as with their less significant agglomeration upon heating. None of the materials reached the maximum mass change corresponding to the complete oxidation of boron, 222%. An additional oxidation step occurs at higher temperatures; however, it is likely that the ignition of boron particles is completely defined by the first oxidation step, shown in Figure 2.4. Therefore, characterizing oxidation that occurs in TG experiments at higher temperatures was beyond the scope of the present effort.

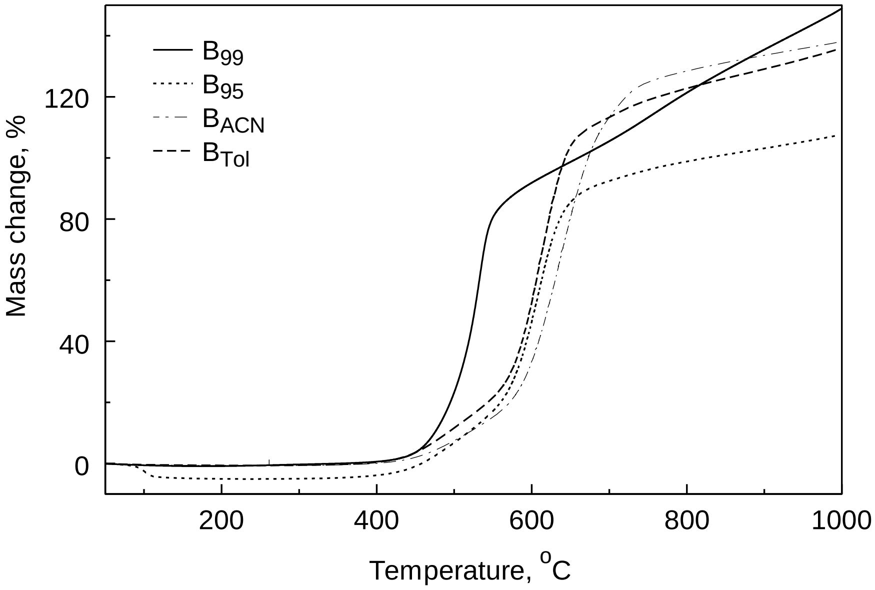

Figure 2.4 TG curves showing oxidation of different materials heated at 2 °C/min.

To describe the oxidation kinetics, measurements recorded at different heating rates and shown in Figure 2.5 were processed using a model-free isoconversional method introduced by Vyazovkin (Vyazovkin 2001; Vyazovkin et al. 2011; Vyazovkin and Wight 1999). The calculated apparent activation energy as a function of the reaction progress expressed directly as the sample mass change is shown in Figure 2.6. As the initial stages of oxidation are of the most interest for ignition processes, a logarithmic axis was chosen for the mass change in order to magnify the low-mass region. An increase in the apparent activation energy observed for all materials at the mass change of oxidized sample approaching 20% is likely associated with agglomeration of the oxidized particles. Loss of reactive surface cannot be adequately accounted for in the calculation and results in an apparent increase in the apparent activation energy. For B_{99}, the apparent activation energy increases slower than for other materials, which probably explains an earlier onset of the oxidation step for this material, cf. Figure 2.5. Among other materials, at the mass change around 10%, the apparent activation energy is lowest for B_{Tol}, consistent with the observed higher rate of oxidation seen in Figure 2.5 as compared to B_{95} and B_{ACN}. Therefore, B_{Tol} is the most reactive powder among those based on 95-% pure boron. Based on its apparent activation energy at the mass change around 10%, the oxidation rate of B_{Tol} is also more sensitive to temperature change than that of B_{99} .

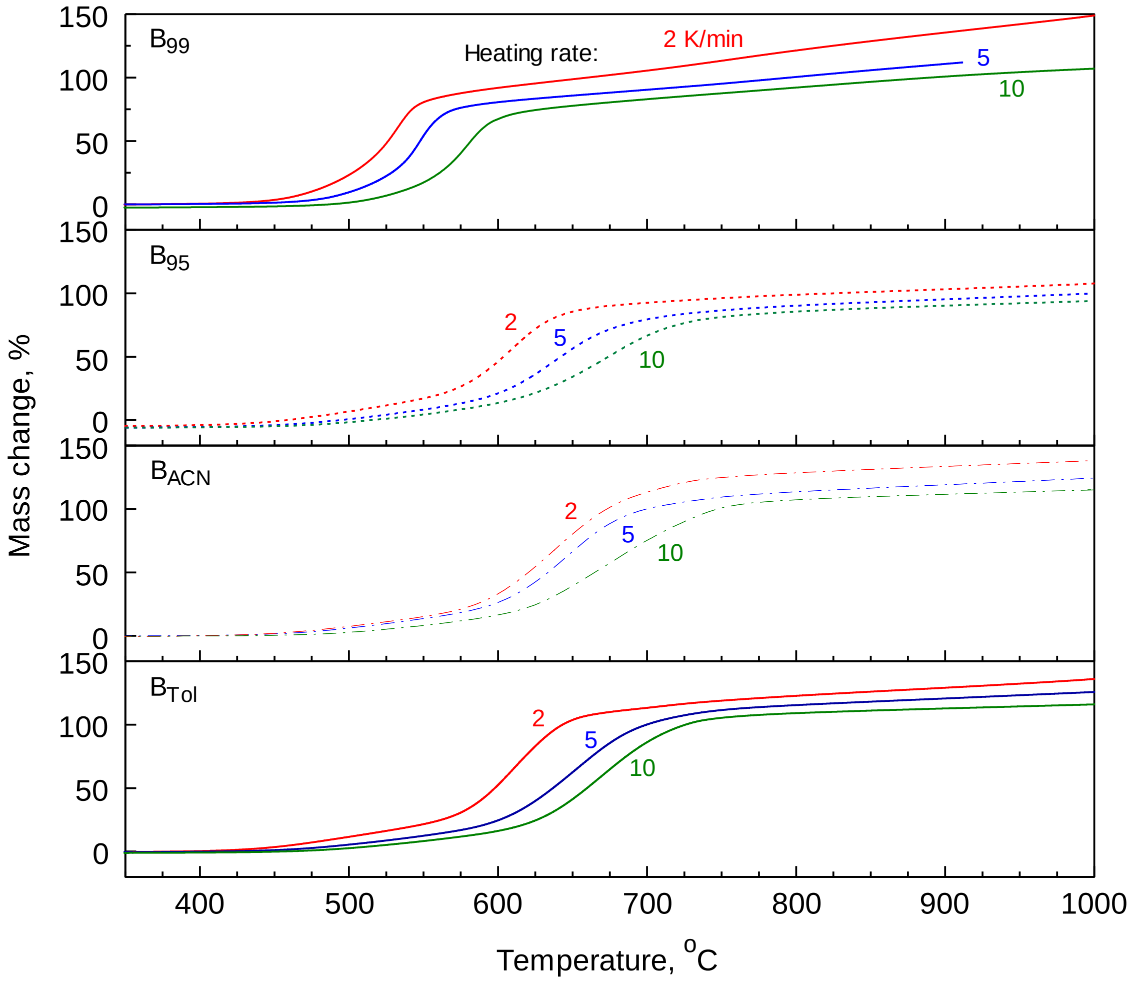

Figure 2.5 TG traces measured at different heating rates for different boron samples.

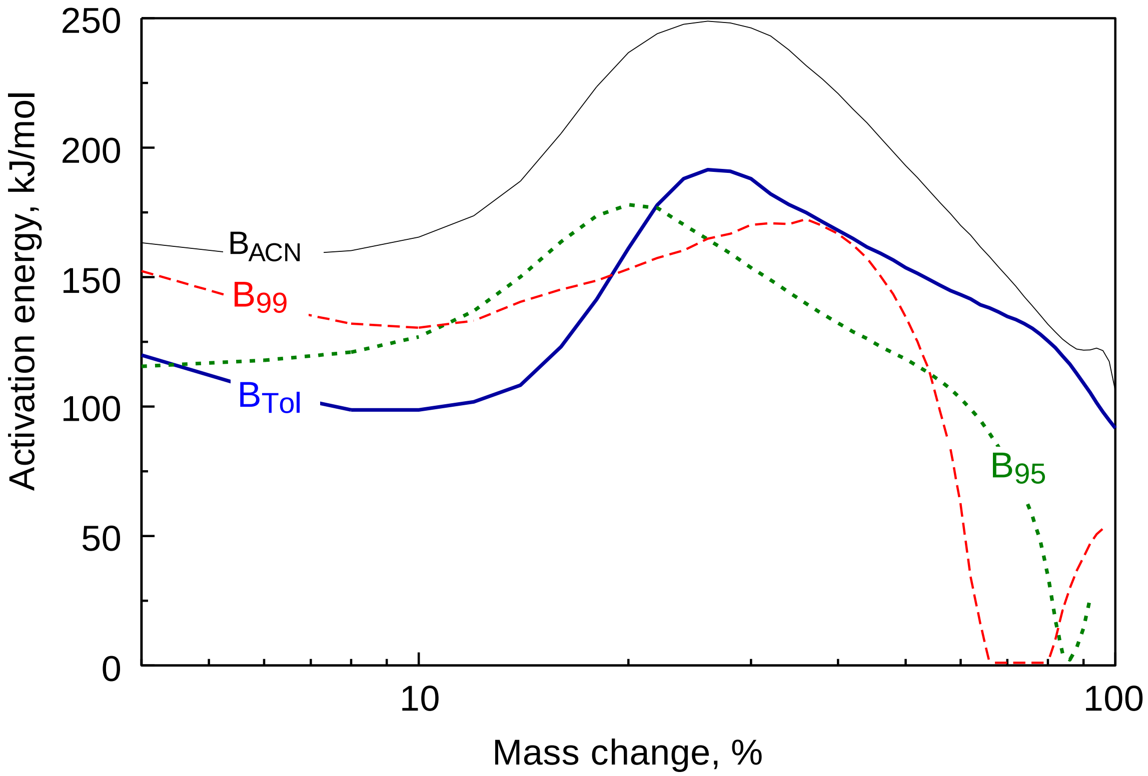

Figure 2.6 Apparent activation energy for different materials calculated by model-free isoconversional method as a function of the reaction progress for the oxidation step occurring between 450 and 750 °C.

2.6 Discussion

Commercial boron powder consists of agglomerated micron-sized primary particles; the agglomerates are likely held together by van der Waals interaction of the particle surfaces coated with hydrated oxide. The agglomerates can thus be broken when the oxide layer is fully or partially dissolved. Stratification of the boron powder agitated ultrasonically in acetonitrile is most likely associated with enhanced re-agglomeration of particles with dissolved boric acid and partially dissolved boron oxide layers. Produced agglomerates are readily broken apart when the powder is re-suspended and ultrasonically agitated in a fluid (either acetonitrile or toluene), possibly, because of dissolution of the remaining oxide layer. This explanation is consistent with the observed reduced mass loss signifying dehydration upon heating for powders washed repeatedly (compare data in Figure 2.1 and Table 2.1). Ultrasonic agitation employed in the present study removed substantially more of the oxidized material than could be achieved in the previous work (Chintersingh, Schoenitz, and Dreizin 2016), where boron-acetonitrile suspension was stirred using a shaker mill without milling media.

The material remaining in the top layer of the stratified suspensions includes highly oxidized boron and fine oxide particles, which could have separated from the initial boron agglomerates. The formation of loose agglomerates by boron particles with partially removed oxide layer processed in acetonitrile causing their settling at the bottom of the container makes it easier to separate such particles from the suspension; this effect can be used in a practical process for preparation of surface-modified boron powders.

TAM III measurements suggest that the surface oxide layer is not simply removed from boron, but is replaced by a different layer, protecting boron from oxidation, making the prepared materials even more stable in air than as-received, oxide-coated commercial boron powder. The stability is particularly improved for the samples processed in toluene, B_{Tol}. Formation of a new surface layer is also in agreement with the observed changes in the oxidation at elevated temperatures and in the different apparent activation energy for the processed B_{ACN} and B_{Tol} powders compared to the starting material B_{95}. The more pure boron powder, B_{99} remains the most stable material at low temperatures, while it starts oxidizing at a lower temperature upon its heating, suggesting that the permeability of the surface boron oxide is strongly affected by the impurities present in boron. One of the most common impurities in boron is magnesium (Gaulé 2013). This is corroborated by the elemental analysis results shown in Table 2.1. We assume that formation of porous MgO inclusions in the B_2O_3 layer covering particles can make it easier for boron and oxygen to diffuse through the oxide film at a low temperature, and thus accelerate boron oxidation as observed in TAM III measurements (see Figure 2.3 and Table 2.2). From data for B_{99} and B_{95} in Table 2.2, it appears, however, that the oxide film formed on boron particles with more impurities (B_{95}) is thicker than that on a higher purity boron, requiring more heat for B_{95} hydration. A thicker oxide layer, present on a less pure boron becomes more protective at elevated temperatures, as seen from Figure 2.3. These results suggest that the mechanism of oxidation changes for B_{95} and materials derived from it (B_{ACN} and B_{Tol}) as a function of temperature. At low temperatures, the preferred diffusion paths lie through MgO inclusions in the surface oxide. Because of the limited number of MgO inclusions, this process results in a slow reaction and thickening of boron oxide layer near the initial MgO inclusions. At higher temperatures, when the oxidation rate increases, boron oxide starts to melt and form a continuous layer on the particle surface, the diffusion through the growing B_2O_3 film becomes the rate-limiting process.

Previous research on boron powder oxidation kinetics (Jain et al. 2011) suggested apparent activation energies near 200 kJ/mol, which is broadly consistent with our results at the later oxidation stages. However, results were contradictory for measurements at constant heating rate vs. isothermal, and no clear conclusion could be reached. In addition, current results emphasize initial oxidation stages, which are unaffected by the presence of liquid boron oxide, and most relevant for boron ignition.

The apparent activation energy obtained from the present measurements and shown in Figure 2.6 may be useful for prediction of ignition behaviors for different boron powders. The growth of the apparent activation energy at high reaction progress, which is most likely caused by agglomeration of the powders, should be discarded when considering ignition of individual boron particles. Thus, the apparent activation energy corresponding to the mass gain of around 10 % in Figure 2.6 should be used in practical ignition models. This analysis suggests that B_{Tol} has the lowest apparent activation energy, and thus is expected to be the most reactive material.

Unfortunately, the nature of the new layer formed on surface of the modified powders, B_{ACN} and B_{Tol}, is not yet well understood; additional work aimed at characterization of such layers is desired in the future.

2.7 Conclusions

Ultrasonic agitation of 95-% pure boron in acetonitrile followed by its processing in toluene yields a powder that has substantially less oxide than the commercial material, is more stable in room air, and oxidizes more readily upon its heating. Although the nature of the passivating layer produced by boron powder treatment in hydrocarbon fluids is not understood, such surface-modified powders are expected to be attractive for practical systems using boron as a fuel. The apparent activation energy of oxidation at elevated temperatures is lowest for the powder surface modified in acetonitrile and toluene (ca. 100 kJ/mol), suggesting that this powder will have the shortest ignition delay upon its thermal initiation. The results suggest that the oxidation mechanisms of boron powders change as a function of temperature. At room temperature, slow oxidation (aging) is governed by enhanced diffusion of the reacting species through impurities in the surface boron oxide, such as MgO. At elevated temperatures, the reaction rates accelerate and the diffusion through the growing layer of B_2O_3 becomes the rate limiting process.

CHAPTER 3

COMBUSTION OF MG AND COMPOSITE MG·S POWDERS IN DIFFERENT OXIDIZERS

3.1 Abstract

Micron-sized, spherical magnesium powders were ignited by a CO_2 laser beam and by injecting them in the products of air-C_2H_2 and air-H_2 flames. The same experiments were performed with composite Mg·S powders prepared by mechanical milling magnesium and elemental sulfur powders. The non-spherical Mg powder used to prepare composites was also explored in selected combustion tests. Flow conditions were varied in experiments performed in air with all materials. The combustion products were collected for particles burning in air; the products were studied using electron microscopy. Optical emission produced by burning particles was recorded using filtered photomultipliers. The emission pulses were processed to recover the particle burn times and their temperatures. Fine Mg particles burn in air very rapidly, with the burn times under 1 ms for particles finer than ca. 10 µm. The apparent trend describing burn time as a function of the particle size for such particles is $t{\sim}d^{0.5}$. The particles burn without generating a detectable standoff flame zone or producing smoke; combustion products are particles of MgO with dimensions comparable to those of the starting Mg powder particles. Both the particles burn times and their measured flame temperatures decrease slightly when particles are carried by faster air flows. The present experimental results is interpreted qualitatively assuming that the reaction occurs at or very near the boiling Mg surface and its rate is limited by the inward diffusion of oxygen. It is further proposed that the fine, solid MgO particles formed in the flame are deposited onto the liquid Mg, causing little change in the overall Mg droplet

dimension despite evaporation of the boiling Mg. Combustion of Mg in air-C_2H_2 and air-H_2 flames occurs much slower than in air, suggesting that CO_2 and H_2O are less effective oxidizers for Mg than O_2. Combustion of composite Mg·S particles follows a two-step process. In the first step, sulfur is evaporated. When the particles are heated by a CO_2 laser beam, rapid evaporation of sulfur leads to a sudden change in the particle velocity. Once sulfur is removed, the particles burn similarly to the pure Mg.

3.2 Introduction

Powders of metals and metallic composites or alloys are commonly used as high energy density fuel additives or primary fuels in pyrotechnics, explosives, and propellants (Price 1984b; Pivkina et al. 2004; Koch 2011). This explains the sustained interest in metal combustion over many decades. Combustion of metal particles is also fascinating visually, producing bright luminous streaks with distinct spearpoints and/or micro-explosions (Nelson 1965; Dreizin 2000; Overdeep et al. 2015). Very early models of metal particle combustion were similar to that of a droplet of a hydrocarbon fuel, involving evaporation of the fuel from the particle surface and combustion occurring in the standoff flame and rate limited by gas phase diffusion processes (Davis 1963). For some metals, like boron, zirconium, titanium and others, this approach was found to be simply inappropriate as indicated by the Glassman criterion, comparing the boiling or saturation temperatures for the metals and their combustion products, metal oxides (Glassman 1960). For such metals, primary oxidation reactions were found to occur directly on the metal surface. For metals with relatively low boiling points, such as Mg, the hydrocarbon-like combustion model seemed more fitting. In his seminal papers (Law 1973, 1976), C.K. Law, analyzed an effect unique to combustion of such metals. The model proposed by Law accounted for the formation of condensed combustion products or smoke particles, which distinguishes fundamentally combustion of volatile metals from that of hydrocarbon droplets. The condensation of products was analyzed as well as their migration from the flame zone both towards and away from the burning particles. Such effects were found to be affecting the heat and mass transfer for the burning particles and thus the particle burn rates. Later it was recognized that similar effects might be responsible for the observed irregularities in metal particle combustion, causing micro-explosions (Dreizin 2000, 2003).

Despite substantial progress in understanding metal combustion in recent years, catalyzed lately by development of nano-sized and nanocomposite metal fuels (Dreizin and Schoenitz 2009; Yetter, Risha, and Son 2009; Sundaram, Yang, and Yetter 2017), there were only a few studies focused on combustion of Mg powders, all dealing with coarse particles (Florko et al. 1986; Valov, Kustov, and Shevtsov 1994; Dreizin, Berman, and Vicenzi 2000; Legrand et al. 2001). Primary applications of Mg as a fuel have been in pyrotechnic devices, although recently, there was interest in its combustion as a component of reactive materials designed for agent defeat applications (Wang, Corcoran, and Dreizin 2015; Wang et al. 2016). Under most circumstances, Mg is expected to primarily burn in the vapor phase, generating refractory condensed MgO particles. While the early studies by C.K. Law (Law 1973, 1976; Law and Williams 1974) have established a general approach to analyzing such combustion systems, the results and models are verified and relevant for particles coarser than ca. 100 µm, whereas most applications use finer powders. Effects associated with fine particle sizes as well as those caused by varying flow conditions, involving, for example, turbulent flow, or effect of different oxidizing environments, e.g., air vs. steam vs. mixture of carbon dioxide and steam, remain largely unexplored. Detailed experimental data, necessary to justify further models are scarce. One of the main difficulties in quantifying the metal particle burn times experimentally is associated with broad size distributions of most metal powders, including Mg. Previously, it was common to assign the average measured burn time to the average particle size; however, this methodology could be misleading. Recently, an approach was proposed enabling one to quantify the particle burn times correlating particle size distributions with the statistical distribution of the measured burn times (Wang, Schoenitz, and Dreizin 2017; Chintersingh et al. 2016b; Wang, Corcoran, and Dreizin 2015; Corcoran et al. 2013a). Results were published for combustion of fine Mg powders in laminar flames produced by hydrogen and oxygen (Corcoran et al. 2013a) and by air and acetylene (Wang, Corcoran, and Dreizin 2015). Here, this approach is further exploited to characterize combustion of particles of Mg and Mg·S composite powders in air at different flow conditions. In addition, the database for combustion of both materials in air-hydrogen and air-acetylene flames is extended.

3.3 Materials

Three powders are investigated in this paper: two commercial magnesium powders and a custom-prepared composite of magnesium and sulfur. A spherical, 99.8% pure magnesium powder was obtained from Hart Metals. Its nominal particles sizes vary in the range of 1-11 µm. Scanning electron microscopy (SEM) images of this powder were shown in an earlier publication (Wang, Corcoran, and Dreizin 2015). SEM images confirmed that the particles were spherical and their sizes varied within the range specified. The second, non-spherical, 99.8% pure, -325 mesh magnesium powder used was by Alfa Aesar Stock

#10233. Its SEM image was shown in Ref. (Corcoran et al. 2013a). The latter powder was used as a starting material to prepare composite Mg·S powders by mechanical milling and thus it was added as an extra reference material for selected experiments in the present study. A SPEX Certiprep 8000D shaker mill was used to prepare the composite Mg·S powder. The powder was prepared in hardened steel milling vials using +100-170 mesh glass beads as milling media. Each vial was charged with 2.15 g of Mg and 2.85 g of sulfur, with a total powder mass of 5 g, comprising the stoichiometry of MgS. The milling media to powder mass ratio was 5. The milling time was 1 h. Images of this powder taken by a LEO 1530 SEM are shown in Figure 3.1. A phase contrast enables one to readily distinguish between darker surfaces of Mg and lighter surfaces of S. Using glass beads resulted in effective coating magnesium particles with sulfur rather than in a fully-dense composite, for which both components would be mixed volumetrically. At the same time, using glass beads minimized the probability of initiating the reaction between Mg and S mechanically, which was shown to occur readily when Mg and S were milled using steel balls (Abraham et al. 2016). The particle shapes are somewhat similar to those of the starting, -325 mesh Mg powder, although some particles are flattened during the milling. Whereas the sulfur coating is discontinuous, it is well mixed with magnesium and no uncoated Mg particles or separate S fragments were detected.

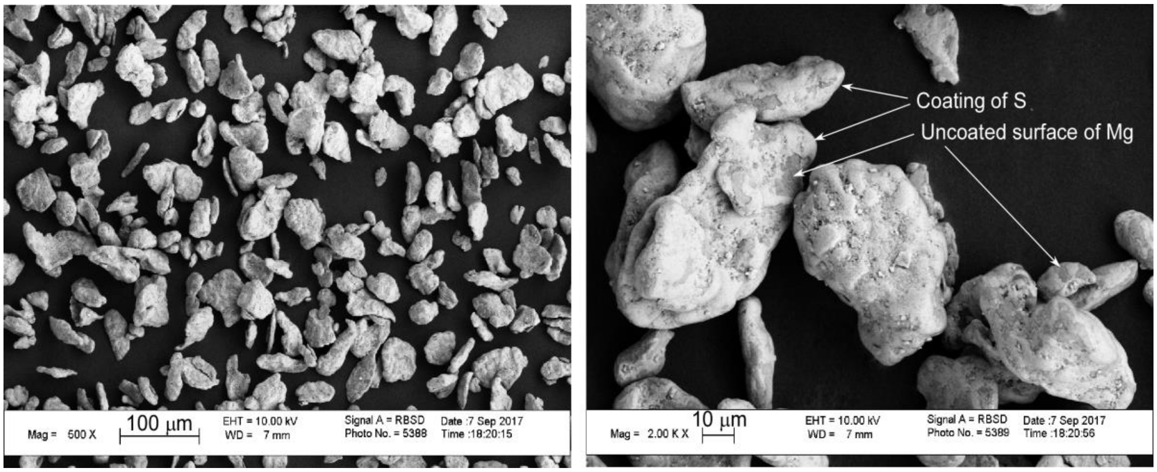

Figure 3.1 SEM images of the prepared Mg·S composite powder particles. Left: overview; right: particle closeup.

Particle size distributions for all three powders are shown in Figure 3.2. These size distributions were correlated, as discussed further, with the measured distributions of the particle burn times; the correlations yielded the effect of particle size on its burn time for each material. For both magnesium powders, the particle size distributions were reported previously (Corcoran et al. 2013a; Wang, Corcoran, and Dreizin 2015). These same size distributions recast in terms of particle numbers rather than volume fraction were used here and shown in Figure 3.2 for these powders. For Mg·S composite, the powder was fed through the feeder, as in combustion experiments (see below), and collected on a double sided carbon tape placed above the feeder's nozzle. This way, the particle sizes analyzed were corrected for possible agglomeration and/or size classification of the powder by the feeder. SEM images of the collected powder particles were taken at different magnification and particle size distributions for each magnification were obtained using image processing. The different size distributions were combined, accounting for the difference in the number of particles within individual size bins per unit of the substrate area observed for each magnification. Details of such analysis were discussed elsewhere (Chintersingh et al. 2016b).

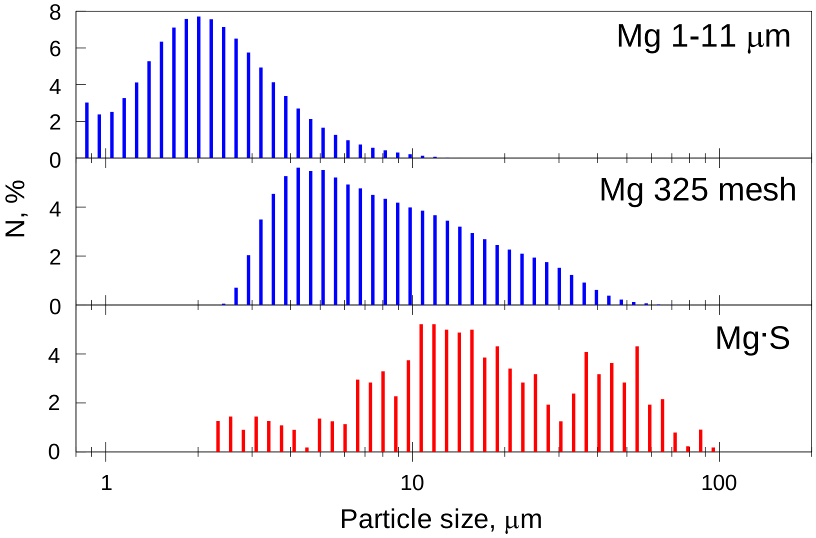

Figure 3.2 Number-based particle size distributions for the powders used in experiments.

3.4 Experimental Details

Combustion of all materials was experimentally characterized in three oxidizing environments: room temperature air, combustion products of an air-acetylene flame, and combustion products of air-hydrogen flame. In all experiments, the same, custom built powder screw-feeder was used descried in detail elsewhere (Corcoran, Hoffmann, and Dreizin 2013). The emission of the burning particles was recorded using two R3896-03 Hamamatsu photomultipliers (PMTs) equipped with 700 and 800 nm interference filters. The signals were saved and processed using a 16-bit PCI-6123 data acquisition board by National Instruments and Lab-view software.

The combustion experiments are illustrated in Figure 3.3. For experiments in air, see left panel of Figure 3.3, particles exited the nozzle moving up and crossed the focused CO_2 laser beam directed horizontally. SEM stubs with double sided sticky carbon tape and with an aluminum foil (particle collection substrates in Figure 3.3) were placed above the particle jet to collect combustion products. The products were examined using SEM. The air flowrate for feeding particles was initially set to 1.25 L/min. It was varied in subsequent experiments between 0.23 and 3.4 L/min. Variation in the air flowrate resulted in different velocities of the particles crossing the laser beam. These velocities were measured using images of particles moving in a modulated green laser sheet. The measurement results are shown in Figure 3.4. It is observed that particles moved with velocities in the range of 0.2 – 2.5 m/s. The laser power was set to 87.5 W, which reliably ignited particles in all experiments. It was noted that at the laser power of ca. 50 W, Mg powders did not ignite. The beam was focused using a ZnSe lens to about 250 μm diameter. Thus, the maximum time for the particles to cross the laser beam varied from 0.2 to 1.25 ms, for the slowest and fastest moving flows, respectively. In a set of experiments, a cylindrical air knife was used to create a turbulent flow pattern just above the laser beam, where particles were expected to burn. Details of the experiments with the turbulent flow patterns were described earlier (Wang, Mohan, and Dreizin 2016; Wang, Schoenitz, and Dreizin 2017).

In different experiments, particles were axially injected into flames, as schematically shown in the right panel in Figure 3.3. Two flames were used: a diffusion air-hydrogen flame served to produce steam as an oxidizing medium (Corcoran et al. 2013a; Quijano, Corcoran, and Dreizin 2015); a premixed air-acetylene flame generated a gas mixture, primarily comprising carbon dioxide and steam as oxidizers (Corcoran et al. 2015; Wang, Corcoran, and Dreizin 2015).

For experiments with air-acetylene flame, conditions used in Ref. (Wang, Corcoran, and Dreizin 2015) were reproduced here: acetylene and air were mixed and fed through the burner at 0.425 and 4.72 L/min, respectively. Results for combustion of Mg in air-acetylene flame were reported in Ref. (Wang, Corcoran, and Dreizin 2015); thus, only experiments with Mg·S composite powders were performed here. Particles were injected into the flame by nitrogen fed at 0.944 L/min. As reported earlier (Wang, Corcoran, and Dreizin 2015), an adiabatic flame temperature calculated using NASA CEA code (McBride and Gordon 1996) was close to 2610 K. Mole fractions of CO_2 and H_2O in the predicted equilibrium products were ca. 0.05 and 0.07, respectively. The other oxidizing species present in the products included CO and OH with mole fractions of 0.18 and 0.004, respectively.

For air-hydrogen flame, the flowrates were set to reproduce the conditions used in an earlier study (Chintersingh, Schoenitz, and Dreizin 2017). Particles were fed into the flame with nitrogen flown at 0.94 L/min. The gas flowrates were set to 0.28 L/min for H_2 and 0.71 L/min for O_2. Air and oxygen mixed with a central hydrogen jet forming a diffusion flame. Metal particles were injected along the flame's axis. Mole fractions of H_2O and N_2 in the equilibrium products were 0.32 and 0.63, respectively. OH and O_2 also present in the products, the mole fractions were 0.008 and 0.004, respectively. The adiabatic flame temperature was calculated to be 2410 K (Corcoran et al. 2015).

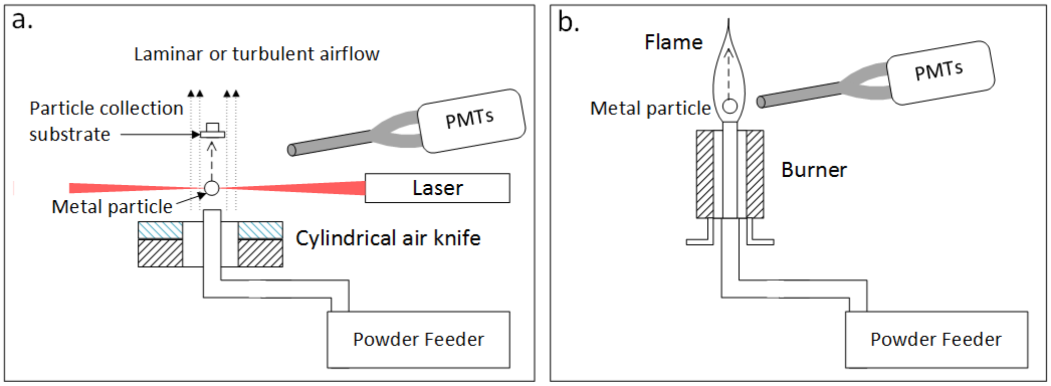

Figure 3.3 Simplified schematic diagrams of combustion experiments: *a*. tests in air with the laser-ignited particles; *b*. tests in products of air-acetylene and air-hydrogen flames.

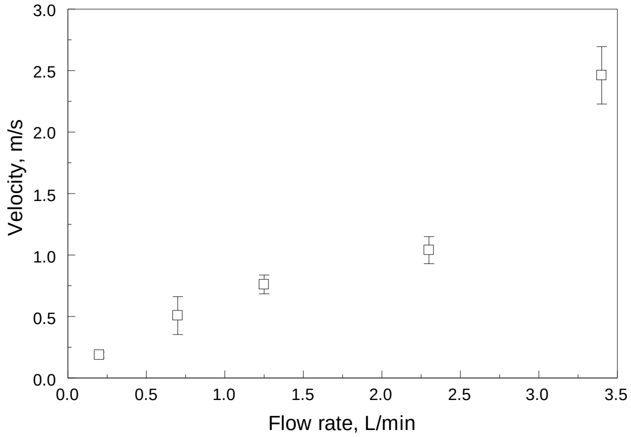

Figure 3.4 Effect of the gas flow rate for the powder feeder on the velocities of the powder particles crossing the laser beam for 1-11 µm Mg powder.

3.5 Results

Spherical 1-11 µm Mg powder in laminar flows

Particles passing the laser beam produced a clearly distinguished but relatively dim optical emission. Their streaks were very short and directed vertically, as the initial particle velocity. Substantially longer luminous streaks were observed for the particles injected in both flames. In each experiment, thousands of individual emission pulses produced by burning particles filtered at 700 and 800 nm were recorded and processed. Several 8-s records were obtained for each experimental condition; each record contained hundreds of individual emission pulses. In the first processing step, overlapped pulses were removed from the dataset. The remaining pulses were used to obtain statistical distributions of the burn times and temperatures, as discussed below. Typical emission pulses recorded with the 700-nm filter for the burning particles are shown in Figure 3.5. The pulses were extremely short for the particles passing the laser beam in air; thus the time scale is logarithmic for direct comparison of such short pulses and much longer emission pulses observed in steam (or in the air-H_2 flame). In steam, many (but not all) pulses had a structure including a stronger initial peak and a weaker, decaying tail. No distinct pulse structure was observed in air. Experiments performed for the same powder injected in air-C_2H_2 flame (Wang, Corcoran, and Dreizin 2015) were used for comparisons below.

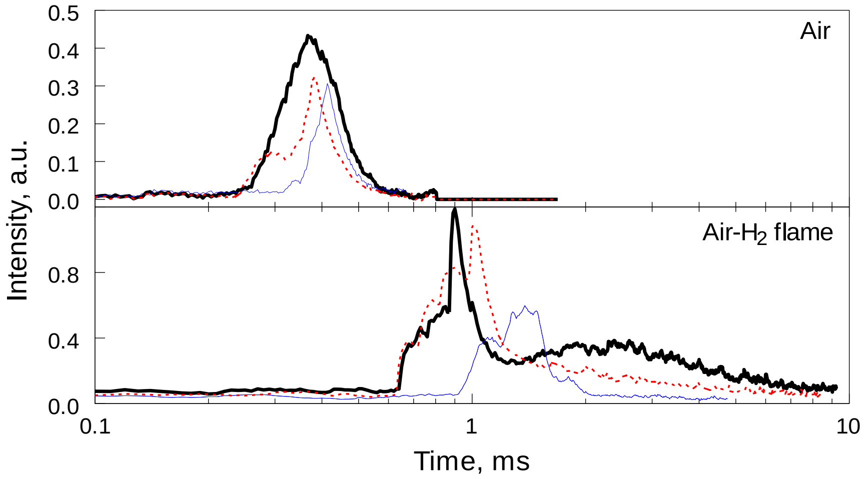

Figure 3.5 Characteristic emission pulses filtered at 700 nm produced by spherical 1-11 µm diameter Mg particles burning in air and in air-H_2 flame.

Because durations of pulses produced by ignited Mg particles in air were comparable to the time required for the particles to cross the laser beam, it was likely that the laser heating contributed to the combustion heat release of the burning particles. To assess this effect experimentally, the flow rate of the air feeding the particles through the beam was changed, as shown in Figure 3.4. It was expected that faster moving particles will spend less time in the laser beam and thus will have a greater fraction of their burn time unaffected by the laser energy. The results are shown in Figure 3.6 in terms of statistical distributions of the measured burn times for particles in different experiments. The burn times were determined automatically from such pulses as shown in Figure 3.5 by measuring the time while the signal was greater than 10% of its peak value for each pulse. Unexpectedly, faster moving particles produced shorter emission pulses. Note that for the highest flowrate, the maximum time a particle can be crossing the laser beam is close to 0.2 ms. Vast majority of emission pulse durations are substantially longer, suggesting that the particles did, indeed, burn outside of the laser beam.

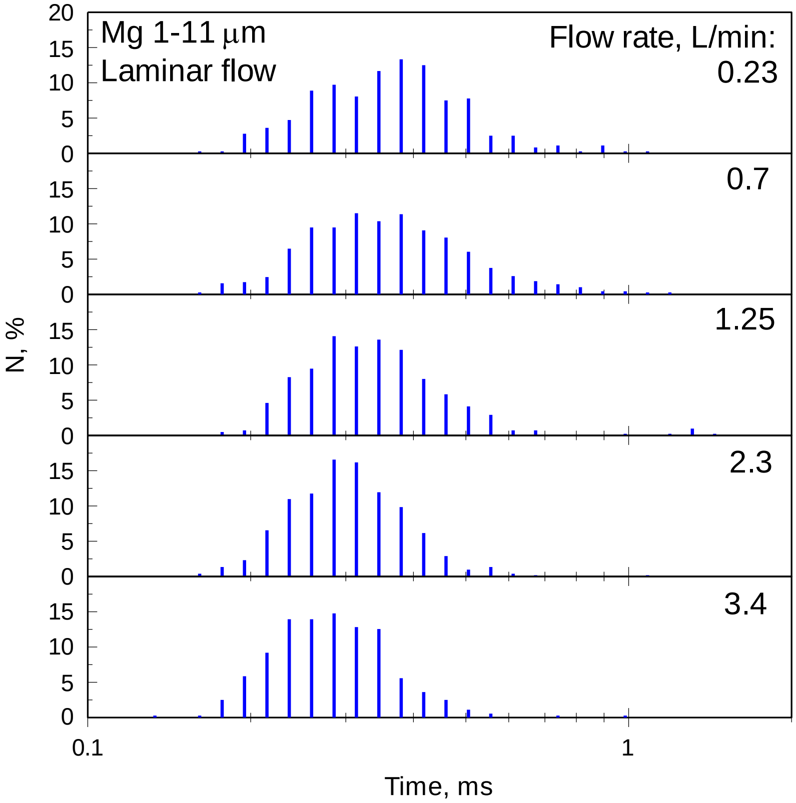

Figure 3.6 Effect of flowrate of air carrying the spherical 1-11 µm Mg powder through the CO_2 laser beam on the powder particle burn times in air. Particles were ignited by passing through a CO_2 laser beam.

Burn time distributions for the spherical 1-11 µm powder in different oxidizing environments are shown in Figure 3.7, where results from Ref. (Wang, Corcoran, and Dreizin 2015) are included for the air-C_2H_2 flame. In agreement with a qualitative assessment from Figure 3.5, the burn times for this fine Mg powder are dramatically shorter in air compared to those in air-H_2 and air-C_2H_2 flames.

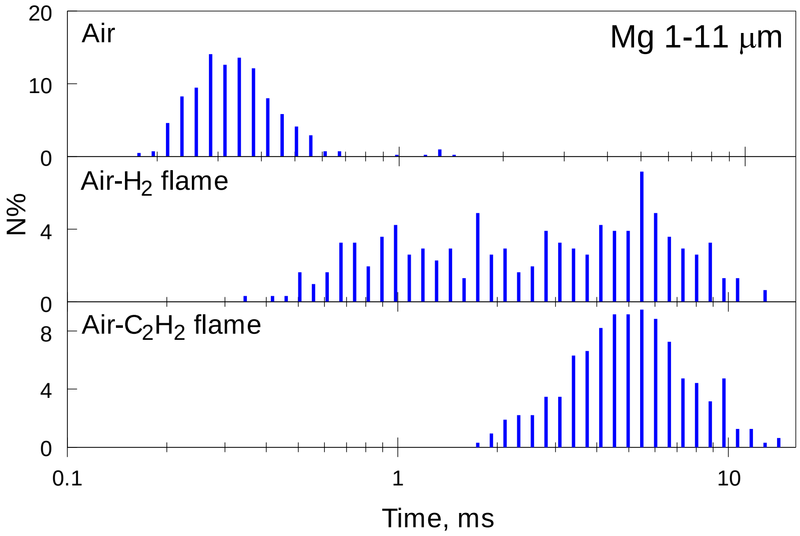

Figure 3.7 Effect of oxidizer on burn times for 1-11 μm spherical Mg powder particles. All experiments employed laminar gas flow. In air, particles were ignited by passing through a CO_2 laser beam (air flow rate 1.25 L/min). Results for the air-C_2H_2 flame are from Ref. (Wang, Corcoran, and Dreizin 2015).

Correlating the measured distributions of the burn times with the particle size distributions shown in Figure 3.2 yields plots shown in Figure 3.8 for the effect of particle diameters, *d*, on their burn times, *t*. Fits representing $t \sim d^n$ trends are shown for the particles in air-H_2 flame ($n_{H2O} \approx 1.6$), air-C_2H_2 flame ($n_{CO2+H2O} \approx 0.75$), and for the highest and lowest powder feed air flow rates for combustion in air, ($n_{air\ min} \approx 0.47$ and $n_{air\ max} \approx 0.69$, respectively).

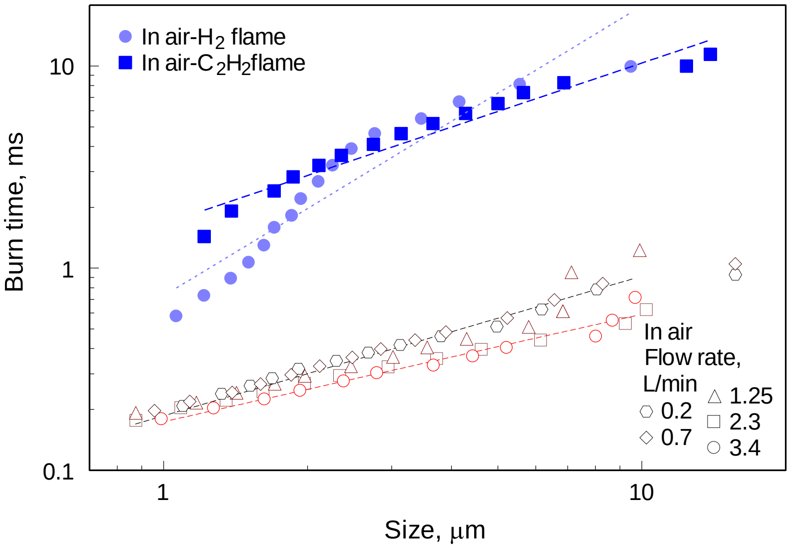

Figure 3.8 Effect of particle size on the burn time for spherical 1-11 µm Mg powder in different oxidizers and at various flow conditions.

An example of a temperature trace produced by a spherical Mg particle ignited by laser and burning in air is presented in Figure 3.9. Two filtered emission traces used to calculate the temperature are shown as well. The emissivity is assumed independent of the wavelength; in other words, the emission is assumed to be produced by a gray body. The temperature is relatively stable during the emission pulse, despite substantial changes in the amplitude of individual signals. For the pulse shown, which is typical, the temperature is just under 2000 K.

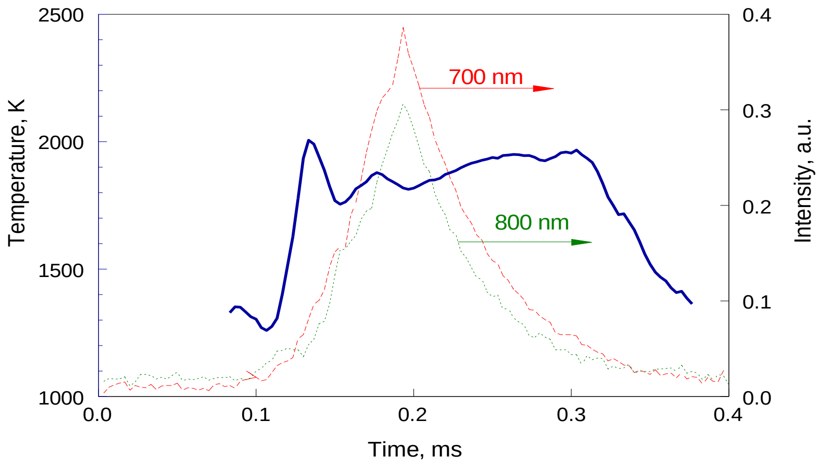

Figure 3.9 Emission pulses filtered at 700 and 800 nm and the respective temperature trace for a Mg particle (1 – 11 µm spherical powder) ignited by the CO_2 laser beam in a laminar air flow.

Similar temperature traces were obtained for all recorded emission pulses produced by the burning particles. To characterize combustion temperatures in a statistically meaningful way, an average temperature value was calculated for a portion of each emission pulse, while the emission intensity of the 700-nm channel exceeded 50% of its peak value for the same pulse. Resulting temperatures were sorted among 50-K wide bins and plotted as histograms for different experiments in Figure 3.10. For particles injected in the flame, an additional background emission due to the flame radiation caused uncertainties in the temperature calculations. These uncertainties were most critical for smaller pulses, for which they led to a systematic error and unrealistically high temperatures. Thus, for the particles burning in the flame only pulses with the amplitude exceeding a threshold value were processed to find the average temperature. The threshold value was approximately 30% of the strongest individual particle peak observed in each specific run. Then, the same processing was applied as described above and the results are included in Figure 3.10.

For Mg burning in air, temperatures histograms are shown for experiments performed with different flow rates used to feed the powder through the laser. The temperatures are slightly higher for the particles fed slower, although the difference in the measured temperatures is not dramatic. For Mg burning in the air-H_2 flame combustion products, the temperature is somewhat higher than observed for Mg in air.

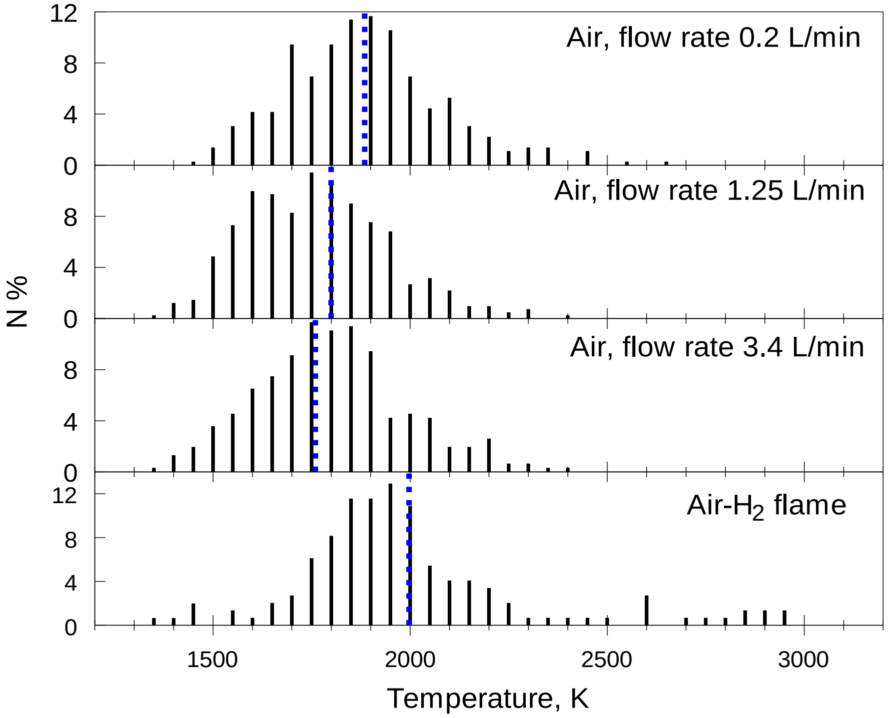

Figure 3.10 Average temperatures calculated for the portions of the emission pulses with the amplitude exceeding 50 % of its peak value for 1 – 11 µm Mg particles burning in different environments.

When collecting combustion products (in experiments performed in air), essentially no particles could be found on the double-sided sticky carbon tape, although unburned particles readily adhered to such a tape, as was observed in preliminary tests. Combustion products could be collected when the substrate was aluminum foil. Characteristic SEM images of the collected particles are shown in Figure 3.11. No smoke particles could be identified. Generally, all collected product particles had particle sizes close to those of the original 1-11 µm Mg powder. The product particles were not spherical, however. All collected particles were analyzed using energy-dispersive x-ray spectroscopy (EDX) and were found to contain MgO only. No unburned or partially oxidized particles could be found.

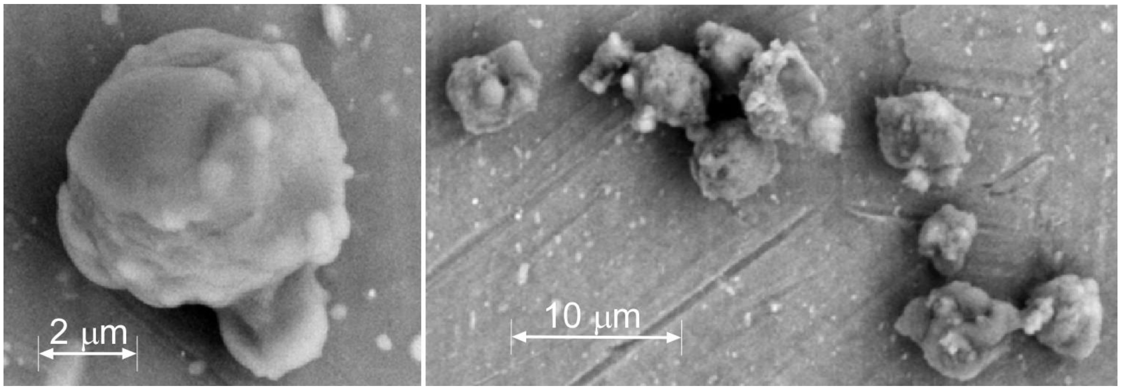

Figure 3.11 Combustion products of 1-11 µm Mg powder collected on an aluminum foil above the laser beam in a laminar air flow (1.25 L/min).

Mg·S composite powder and -325 mesh Mg powder burning in laminar flow

Composite Mg·S particles entering the CO_2 laser beam ignited and burned, while their streaks were directed horizontally, at about 90 ° angle compared to their initial velocity coming from the feeder. All particles moved away from the laser, suggesting quite clearly that evaporating sulfur generated reactive force moving particles in that direction. Thus, once again, the laser energy interfered with the combustion heat release, although the particles quickly left the focal spot of the laser and thus were exposed to an increasingly unfocused beam, as they moved away from their initial injection location.

Characteristic emission traced filtered at 700 nm for Mg·S powder burning in different environments are shown in Figure 3.12. Similar to the results in Figure 3.5, the burn times in air are markedly shorter than those in steam and steam/carbon dioxide mixtures. For many pulses of particles burning in both flames, double-peak shapes are observed; however, the pulse features are indistinguishable for the particles burning in air. Pulses produced by burning -325 mesh Mg powder are qualitatively similar to those shown in Figure 3.12 and thus omitted for brevity.

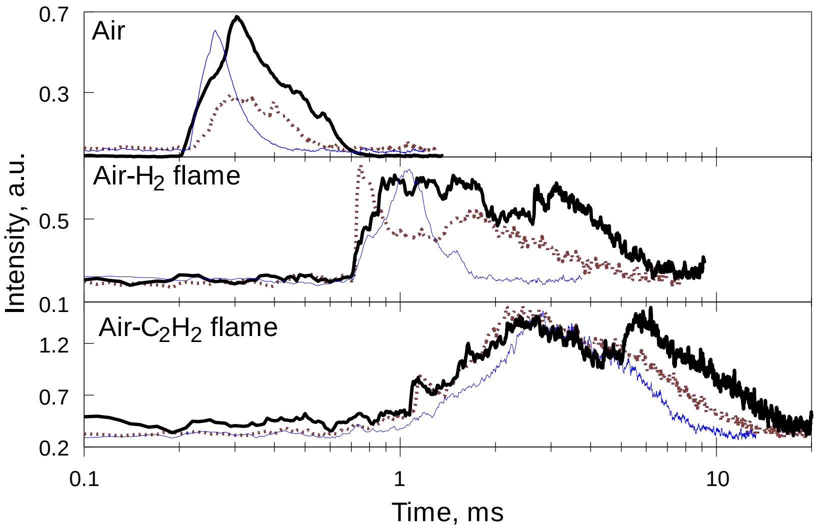

Figure 3.12 Characteristic emission pulses produced by composite Mg·S particles burning in air (1.25 L/min), air-H_2 and air-C_2H_2 flames.

Statistical distributions of the measured burn times are shown in Figure 3.13. As for Mg, the durations increase from air to air-H_2 flame and to air-C_2H_2 flame. Again, the distributions of the burn times for -325 mesh Mg are similar to those shown in Figure 3.13 and thus omitted here.

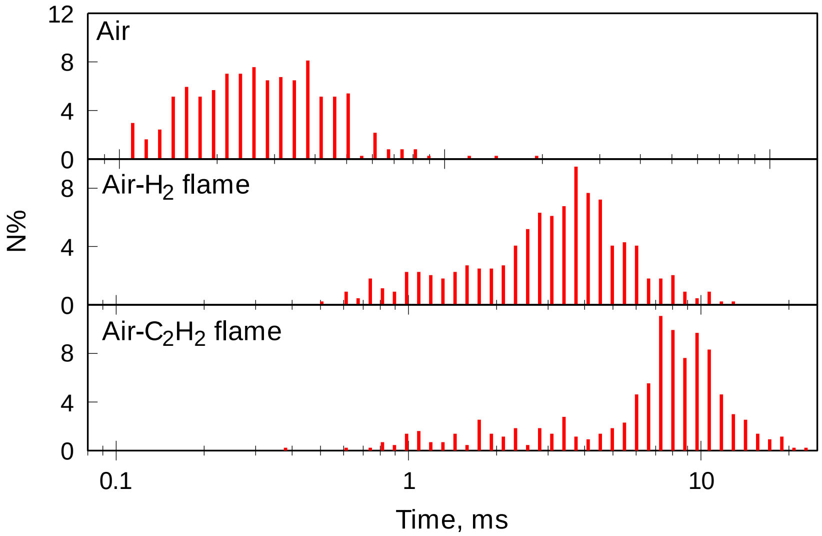

Figure 3.13 Effect of oxidizer on burn times for composite Mg·S powder particles. All experiments employed laminar gas flow. In air (flowrate 1.25 L/min), particles were ignited by passing through a CO_2 laser beam. Other oxidizing environments were formed as combustion products of air-H_2 and air-C_2H_2 flames.

Combining the statistical distributiosns of the burn times with particle size distributions for both Mg·S and -325 mesh Mg powders yields trends shown in Figure 3.14 for the burn times as a function of the particle sizes for both materials. Considering experimental uncertainties, the burn times for both materials are essentially the same for air and steam/carbon dioxide mixtures, for which direct comparisons are available. Although not shown in Figure 3.14, the $t \sim d^n$ fits were found for all experimental trends shown. For Mg·S composite powder, the values of n for the combustion in steam, carbon dioxide/steam mixture, and air were 0.74, 0.84 and 0.74, respectively. For -325 mesh Mg powder, $n_{CO2+H2O} \approx 0.8$ and $n_{air} \approx 0.5$.

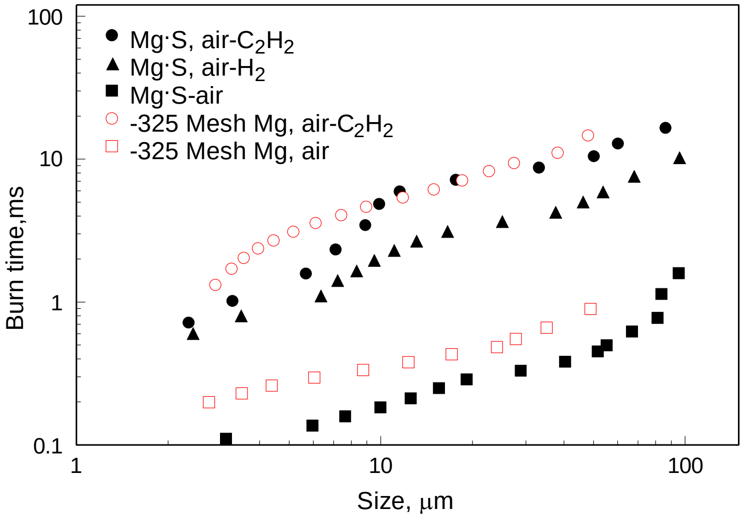

Figure 3.14 Effect of particle size on the burn time for -325 mesh Mg and composite Mg·S powders in different oxidizers. In air, flowrate was 1.25 L/min.

A characteristic temperature trace produced by the burning composite Mg·S particle is shown in Figure 3.15. When the amplitudes of the emission pulses are close to their peak values, the temperature is close to 2000 K. The temperature appears to increase when the emission decays; however, that apparent increase may be affected by a substantial noise in the emission traces. For statistical analysis, as noted above, only the temperatures obtained from the signals exceeding 50% of the peak intensity were considered; with that analysis, the average temperature for the trace shown in Figure 3.15 is close to 1980 K. Note that both emission pulses and the individual temperature traces for Mg·S composite particles were very similar to those observed for the -325 mesh Mg powder, serving as a starting material to prepare the composite. The temperature traces for -325 mesh Mg are omitted for brevity.

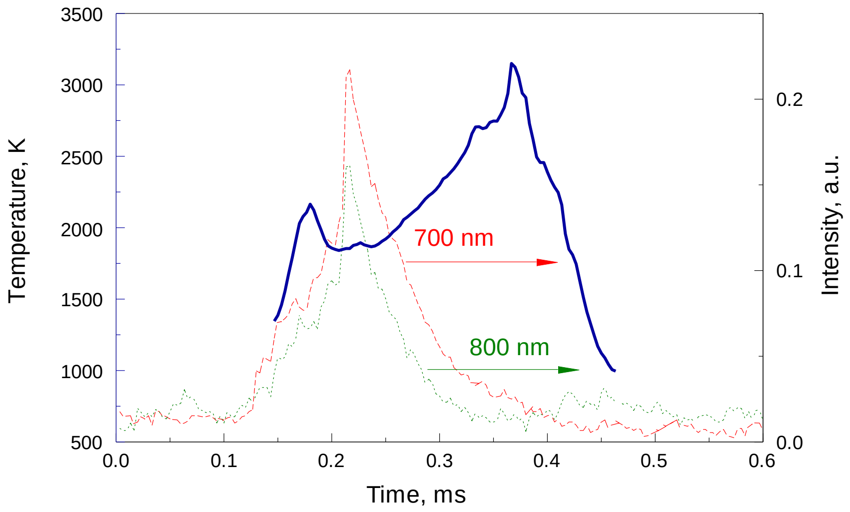

Figure 3.15 Emission pulses filtered at 700 and 800 nm and the respective temperature trace for an Mg·S composite particle ignited by the CO_2 laser beam in a laminar air flow.

Histograms of the average temperatures for multiple emission pulses for both -325 mesh Mg and for the composite Mg·S powder are shown in Figure 3.16. In air, the temperatures for -325 mesh Mg are close to 2000 K, just slightly higher than those for 1 – 11 µm Mg powder shown in Figure 3.10. For the composite Mg·S powder burning in air, the temperatures are spread over a broader range, including some much higher temperatures around 3000 K. For air-acetylene flame, the temperatures for the composite Mg·S powder are quite high, with most particles exhibiting ca. 2800 K. For the air-hydrogen flame, the measured temperatures are distributed in a broad range, with most particles having temperatures in the range of 2000 – 2500 K.

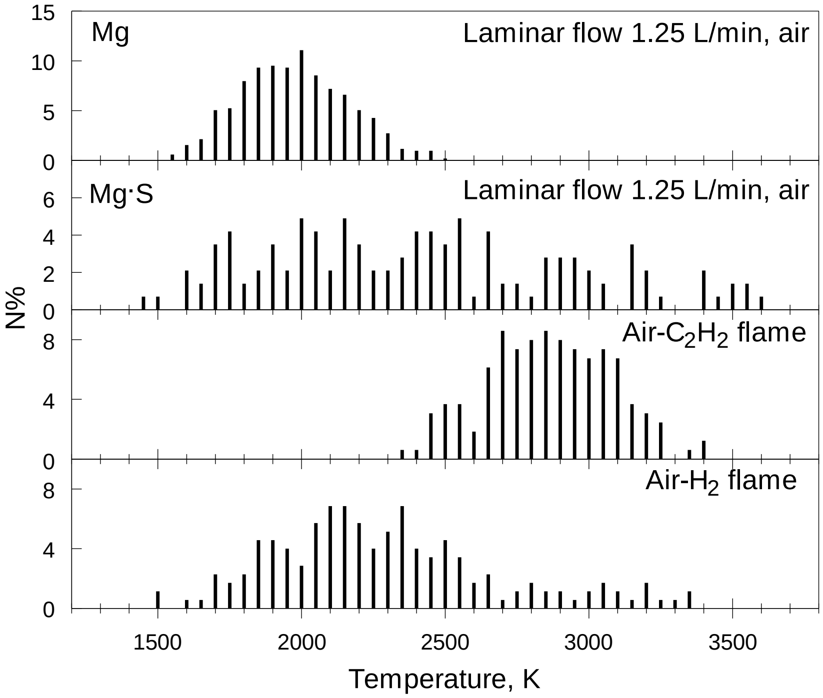

Figure 3.16 Average temperatures calculated for the portions of the emission pulses with the amplitude exceeding 50 % of its peak value for composite Mg·S particles burning in different environments.

Particles collected in combustion experiments above the laser beam are shown in Figure 3.17. It was easier to collect the particles on Al foil compared to the double-sided carbon tape. However, because burning particles were all directed horizontally, the collected particles comprised the unburned material, which passed in vicinity of the laser beam but did not ignite. The particle shapes are markedly different from the starting composite (see Figure 3.1). These shapes might serve to provide some insight into ignition of such composite powders. Sulfur is clearly molten; in some particles, such as inset *a*, sulfur appears to be lost. In others, such as insets *b*, *c*, and *d*, sulfur is significantly redistributed. In some cases, such as inset *d*, the frozen boiling pool of sulfur is observed with spherical voids, presumably formed by escaping bubbles. Except for selected few particles, Mg was unoxidized. One exception is shown in the inset *c*, where EDX shows partial oxidation of Mg.

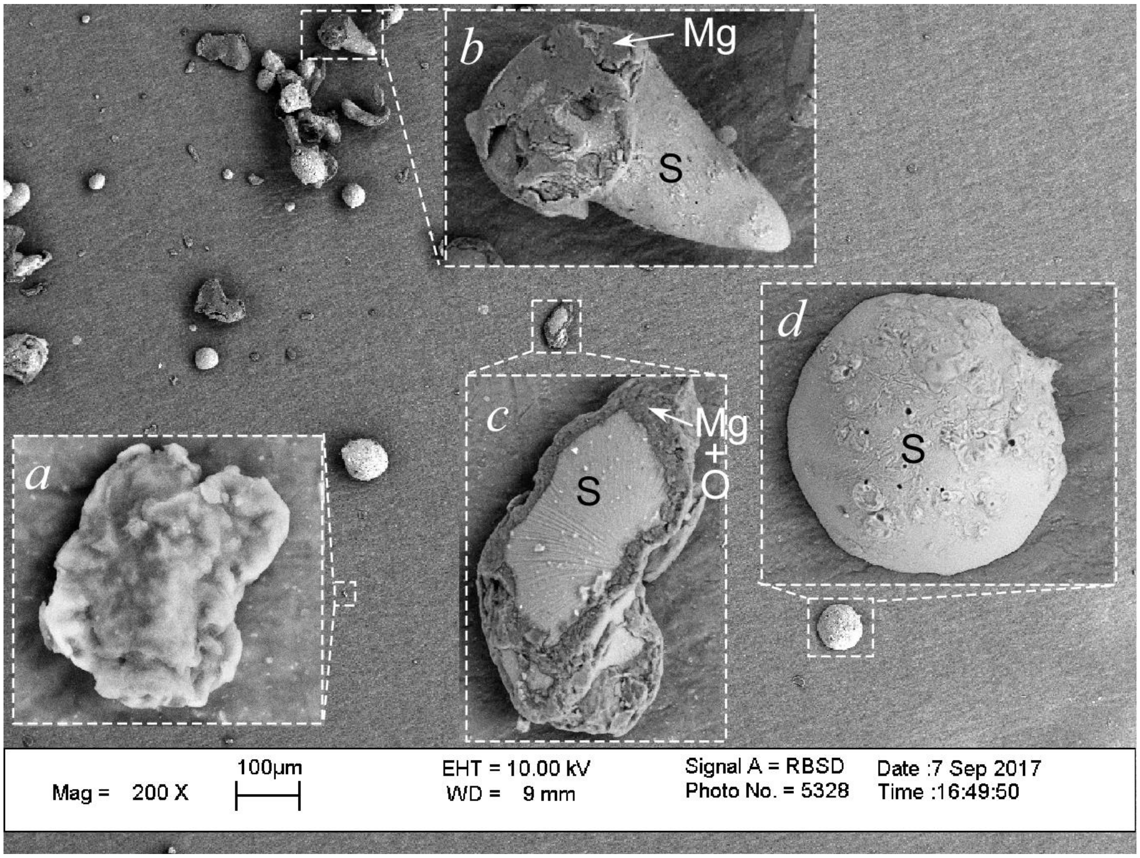

Figure 3.17 Particles collected above the laser beam in a laminar air flow during the combustion experiment with a composite Mg·S powder.

Effect of flow turbulence on the burn rates of different powders in air.

The turbulent flow was produced using a cylindrical air knife, as described in detail earlier (Wang, Mohan, and Dreizin 2016). The same flow conditions are analyzed previously, with the turbulence flow kinetic energy of 0.136 m^2/s^2 were reproduced. The results for all materials in terms of statistical distributions of the measured burn times are shown in

Figure 3.18. It is apparent that the turbulent flow was not affecting the burn rates for any of the powders tested here.

Additional observations that can be made from Figure 3.18 is that the burn times are very similar to each other for both -325 mesh Mg and Mg·S composite prepared using this same Mg powder as a starting material. However, surprisingly, the burn times are somewhat longer for the spherical 1-11 µm Mg, which has smaller particle sizes.

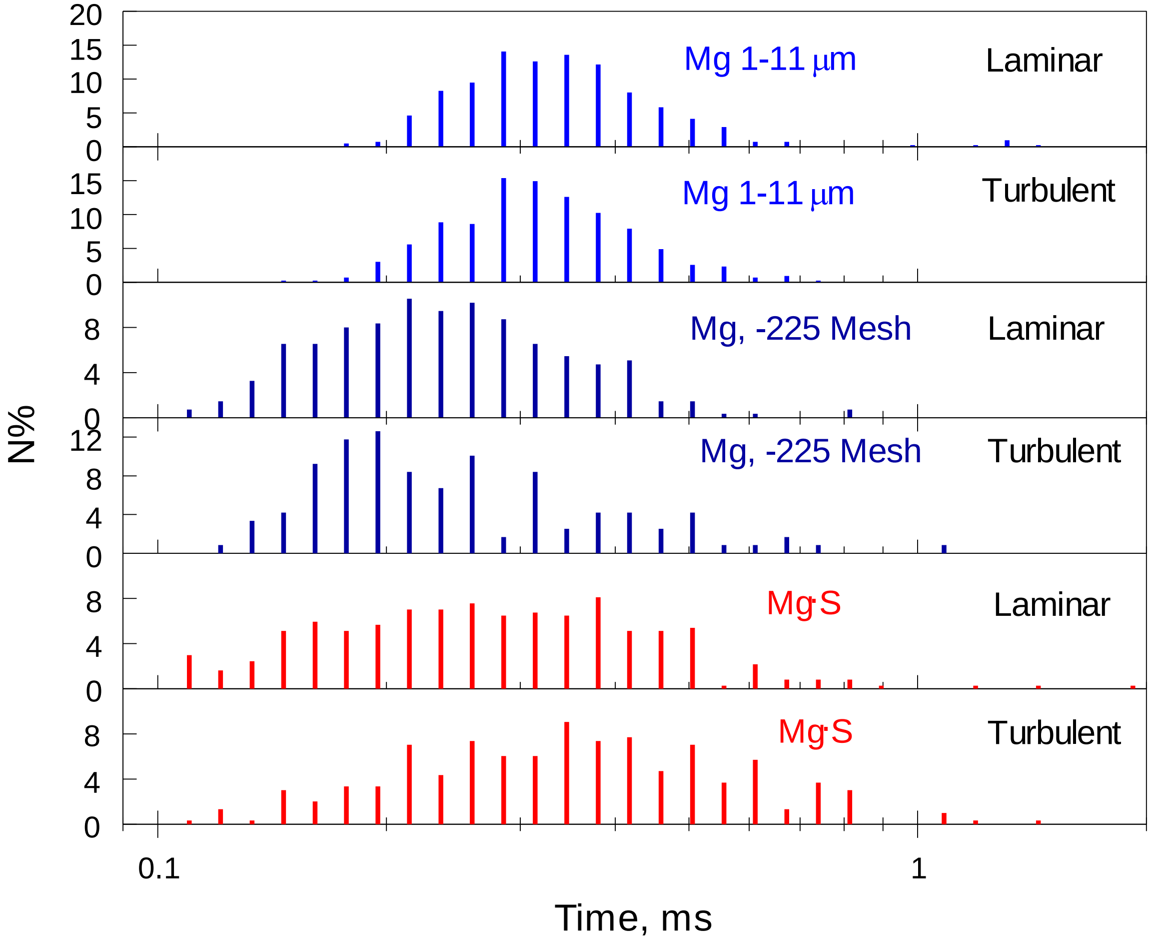

Figure 3.18 Effect of flow conditions on burn times of different Mg and Mg·S powder particles. All experiments were performed in air (feeder airflow was 1.25 L/min), particles were ignited by passing through a CO_2 laser beam.

3.6 Discussion

Combustion of fine Mg particles in air

Combustion products analyzed for Mg particles ignited by the laser and burnt in air suggested complete oxidation. The absence of smoke suggested that the reaction occurred at or very close to the particle surface. The above scenario is somewhat unexpected, because of the high vapor pressure of magnesium; however, the absence of smoke around quenched spherical Mg particles is consistent with the observation reported in Ref. (Wang, Corcoran, and Dreizin 2015), where combustion products for the same powder were captured from the air-C_2H_2 flame. Thus, very short emission pulses observed here for Mg particles ignited in air represent complete combustion events.

As mentioned earlier, in the present experiments the time a particle spent crossing the laser beam was comparable to the very short Mg combustion time measured. Thus, it is important to evaluate the effect of continuing laser irradiation on the burn rates reported here for Mg in air. Consider a 2-µm diameter particle, corresponding to the peak of the measured number-based size distribution for 1 – 11 µm powder (Figure 3.2). This particle size, incidentally, is close to that absorbing the CO_2 laser power most effectively (Mohan, Trunov, and Dreizin 2007). Assuming that the burn time for this particle in air is approximately 0.3 ms (in agreement with results shown in Figs. 3.7, 3.8), and that the heat release equals to the theoretical heat of Mg oxidation, it is estimated that the power produced by its combustion is 0.6 mW. At the same time, when this particle crosses a 250-µm diameter laser beam, the power of the laser absorbed can be estimated accounting for the absorption efficiency of about 0.06 following Ref. (Mohan, Trunov, and Dreizin 2007). This absorbed power cannot exceed 0.34 mW. Thus, the ratio of the combustion power to the absorbed laser power is no less than ca. 1.8. The effect becomes weaker for both smaller and larger particles, for which the absorption efficiency for the laser energy drops rapidly. In addition, for larger particles, a smaller fraction of the burn time is spent while crossing the laser beam. Based on this estimate, it can be concluded that the laser emission is not negligible, but it is not dominating the observed combustion events.

The above conclusion is further consistent with the results presented in Figure 3.6. The particles fed with a slower air flow spent longer time crossing the laser beam. If laser heating were controlling combustion, it would be expected to accelerate the reaction and lead to shorter burn times. Conversely, shorter burn times were observed for particles moving faster, and thus spending less time crossing the laser beam. One explanation for this can be that the reaction was rate limited by transport of oxygen to the particle surface. Thus, the hydrodynamic boundary layer adhered to the particle surface became smaller for faster moving particles, leading to an accelerated mass transfer of oxygen towards them.

It is further interesting to consider the implication of the present temperature measurements. Note first that the measured temperature is based on the optical emission produced by both the particle surface and by the surrounding flame zone, where smoke MgO particles were forming. Thus, the measured temperature depends on the relative dimensions of the particle and the standoff flame zone and on the temperature difference between these diverse emitters. The particle surface must remain at the Mg boiling point, 1364 K. If no standoff flame exists, this temperature must be measured. Assuming that the temperature in the standoff flame is close to the adiabatic flame temperature, independently of the flame location, the dimension of the standoff zone formed in different experiments is proportional to the increase in the measured flame temperature. With this background, consider the present temperature measurements for Mg burning in air, which all point to a temperature well above the Mg boiling point, but well below the adiabatic flame temperatures for Mg exceeding 3000 K and reported to accompany combustion of coarse Mg particles (Dreizin, Berman, and Vicenzi 2000). In air, the maximum adiabatic flame temperature for Mg is estimated to be 3100 K at the equivalence ratio of 1.28 (McBride and Gordon 1996). Thus, the temperatures measured here suggest that the ratio of the particle diameter to that of the standoff flame zone is much smaller in the present experiments with fine particles than that reported for large Mg powders earlier. From results in Figure 3.10, it is observed that the temperatures were higher for particles moving slower, even though such slower moving particles burned longer (Figure 3.6). Thus, the standoff flame approached closer to the particle surface for particles moving with greater speeds.

Assuming, as before, that the oxidizer transport to the particle surface is the rate-limiting step in combustion of fine Mg particles in air, the temperature measurements are readily interpreted, as least qualitatively. For the particles moving faster, a smaller boundary layer would lead to a higher concentration gradient of oxygen over the boundary layer, and thus a greater rate of diffusion of the oxidizer to the fuel. The greater rate of inward diffusion of oxygen will lead to stronger Stefan flows towards the particle surface, which would “compress” the flame zone, pushing the ultrafine MgO particles formed in the flame towards the burning Mg surface. Therefore, higher burn rates would be observed, even though the apparent temperature was reduced because of a narrower boundary layer. Quantitatively, the observed trends may be possible to model considering heat and mass transfer around burning Mg particles; however, such a modeling needs to account for transition heat and mass transfer processes for particles with dimensions comparable to the mean free path of the gas molecules, and it was outside the scope of the present effort.

Consider now the shapes and dimensions of the combustion product particles shown in Figure 3.11. It is interesting that no smoke particles were captured and that the product particles resembled closely the original powder based on their sizes, but not based on their shapes or surface morphology. One scenario explaining formation of such products involves formation of condensed MgO in the flame zone, which is located very close to the burning particle surface. The MgO particles (of very fine, single nm, dimensions) would be carried towards Mg surface by Stefan flow and deposited back into the burning Mg droplet. At the flame temperatures, condensing MgO particles are solid. If such solid particles are absorbed by the boiling Mg droplet, they may not decelerate combustion. Instead, they could enable molten Mg to wick or diffuse out to the droplet surface, where it evaporates and gets transferred to the nearby flame zone. If sufficient amount of MgO is absorbed by the boiling Mg, the particle size will not diminish significantly, despite evaporation of Mg. This would lead to a higher burn rate than would be expected for a droplet with a shrinking core. Note also that high burn rates and short burn times observed here for Mg in air explain the lack of the effect of turbulence on its burn times (Figure 3.18). In the present experiments, the turbulent flow pattern is generated a few mm above the laser beam, where most of the particles were already consumed.

It is also of interest to comment on the apparent difference in the burn times for 1 – 11 µm spherical Mg vs. -325 mesh Mg powders. Despite apparently greater dimensions (Figure 3.2), -325 mesh Mg particles burned faster (Figure 3.18, for example). This observation is consistent to that made in Ref. (Wang, Corcoran, and Dreizin 2015) for the same powders burning in the air-C_2H_2 flame. One may understand this apparent paradox recalling that -325 mesh particles are not spherical. As their SEM images shown in Ref. (Wang, Corcoran, and Dreizin 2015) demonstrate, many particles are flattened and resemble flakes. Thus, the volumes of such particles could be substantially smaller than those of the spheres with the diameters matching their largest dimension. These observations illustrate how one must account for the particle shape, and not only its size obtained from light scattering measurements or even inspection of SEM images, in order to properly interpret the measured burn times.

Finally, it is interesting to compare the burn times measured for a fine Mg powder in air (or with oxygen and the only oxidizer) to those reported earlier for coarse Mg particles. This comparison is shown in Figure 3.19, where the results from this work are represented by the $t \sim d^n$ fits from Figure 3.8 from the highest and lowest laminar air flow rates. The trends for coarse and fine particles appear to cross for particle sizes in the range of 20 – 30 µm. The effect of particle size on the burn time is diminished for the fine powders, leading to a smaller slope of the trend shown. This effect is similar to that observed for aluminum (Badiola, Gill, and Dreizin 2011; Badiola and Dreizin 2012) and other metals (Badiola and Dreizin 2013). It quantitative interpretation must rely on mechanistic models of particle combustion, accounting quantitatively for the rate-limiting processes and evolution of the burning particle composition discussed above.

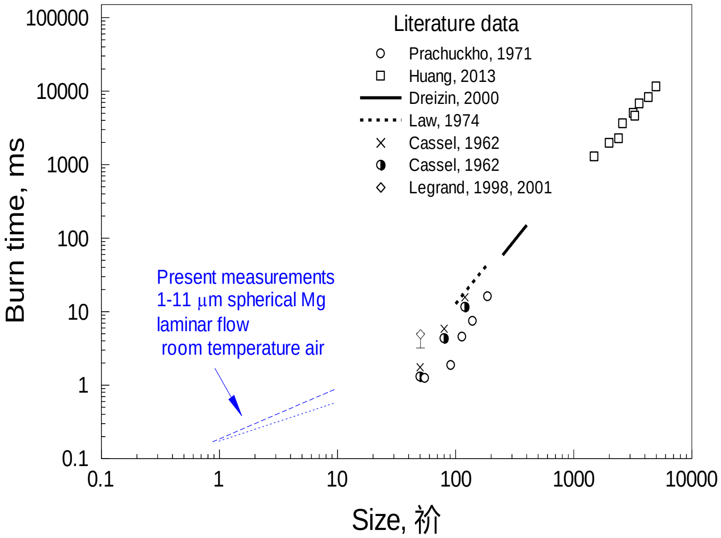

Figure 3.19 Comparison of the presently measured burn times for fine Mg particles burning in air (trends for the highest and lowest feeder flowrates) with previous results reported in the literature for coarser Mg particles.

Combustion of Mg particles injected in flames

The burn times for Mg particles injected in both air-H_2 and air-C_2H_2 flames (Figs. 3.7, 3.8) were substantially longer than those in air. Qualitatively, this shows that oxygen is a much more effective oxidizer for Mg than either H_2O or CO_2. Despite the longer burn times, the measured temperatures for Mg injected in flames are somewhat higher than those in air (Figure 3.10 and results from Ref. (Wang, Corcoran, and Dreizin 2015)). Considering Mg in combustion products of the air-H_2 and air-C_2H_2 flames as in oxidizing environments at their respective adiabatic flame temperatures, it is estimated that the maximum flame temperatures for Mg in air-H_2 and air-C_2H_2 flames are 2833 and 2728 K, respectively (McBride and Gordon 1996). In both cases, the maximum flame temperatures occur at the equivalence ratios close to 1.9. Thus, the measured temperatures are lower than those expected based on the thermodynamic calculations. Assuming, as above, that the increase in the measured flame temperature over the Mg boiling point indicates an increase in the size of the standoff flame zone, the higher temperatures, closer to the adiabatic flame temperatures for these environments, suggest that the reaction zones of Mg vapor with CO_2 and H_2O are broader than that in air. Combustion is observed to occur slower than that with O_2; which is consistent with the greater flame zone, suggesting that even the Mg-rich condition expected in the diffusion flame (generating the maximum temperature) occurs relatively far from the particle surface.

Combustion of composite Mg·S powders

A sudden change in the velocity vector for the composite particles ignited by the CO_2 laser beam, suggests that the sulfur evaporation occurs readily and most likely before Mg ignited. Thus, combustion of such particles can be treated as a two-step process. Sulfur is removed from the material in the first step. In the second step, the powder burns as pure Mg. Indeed, qualitatively, combustion occurred very similarly for -325 mesh Mg and composite Mg·S powder prepared using this same Mg powder. However, the burn rates for the composite Mg·S powder in air was slightly higher than for Mg (Figure 3.14); the temperatures measured for Mg·S particles were also slightly higher than for Mg (Figure 3.16). In both cases, the effect can be associated with the changed direction of the moving Mg·S particles upon crossing the laser beam. Because Mg·S particles moved along the laser beam (away from the laser), it is likely that they remained heated by the CO_2 laser more effectively than pure Mg particles, which crossed the laser beam and continued to burn above it. Thus, it is proposed that the effects of higher burn rates and temperatures for the composite Mg·S particles observed in Figs. 3.14 and 3.16 are superficial and caused by stronger interference of the laser irradiation with their combustion.

3.7 Conclusions

Fine Mg particles burn in air very rapidly, with the burn times under 1 ms for particles finer than ca. 10 µm. The apparent trend describing burn time as a function of the particle size for such particles is $t \sim d^{0.5}$. The particles burn without generating large standoff flame zone or producing much smoke; combustion products are particles of MgO with dimensions comparable to those of the starting Mg powder particles. Both the particles burn times and their measured flame temperatures decrease slightly when they are carried by faster air flows. The present experimental results can be interpreted qualitatively assuming that the reaction occurs at or very near the boiling Mg surface and its rate is limited by the inward diffusion of oxygen. It is further proposed that the fine, solid MgO particles formed in the flame are deposited onto the liquid Mg, causing little change in the overall Mg droplet dimension despite evaporation of the boiling Mg. Combustion of Mg in air-C_2H_2 and air-H_2 flames occurs much slower than in air, suggesting that CO_2 and H_2O are less effective oxidizers for Mg than O_2.

Combustion of composite Mg·S particles follows a two-step process. In the first step, sulfur is evaporated. When the particles are heated by a CO_2 laser beam, rapid evaporation of sulfur leads to a sudden change in the particle velocity. Once sulfur is removed, the particles burn similarly to the pure Mg.

CHAPTER 4

REACTIVE COMPOSITE B·MG POWDERS PREPARED BY MECHANICAL MILLING

4.1 Abstract

Composite reactive material powders combining boron with 40 wt% of magnesium are prepared by mechanical milling of elemental boron and magnesium powders. Commercial boron is washed with acetonitrile to remove surface boron oxide, which can react with magnesium during milling. Thermogravimetric measurements showed two oxidation steps. X-ray diffraction analysis of partially oxidized samples showed that selective oxidation of magnesium occurred during the first step. It was followed by oxidation of boron during the second step. Prepared composite powders were ignited using an electrically heated filament, by electric spark, and in constant volume explosion tests. Ignition is caused by selective oxidation of magnesium. Ignition temperature of the composite powders obtained in heated filament tests was lower than that measured for the pure magnesium. A faster initiation by electric spark was observed for powders prepared using washed boron. This was attributed to an increased effect of heterogeneous oxidation for high heating rates, and thus to an accelerated heterogeneous oxidation for powders achieved after removal of the natural boron oxide and hydroxide surface layers. Following the ignition, boron continued to react, contributing to the released combustion heat and pressure generated by the flame in both constant volume explosion and spark ignition tests.

4.2 Introduction

Boron is an attractive fuel because of its high volumetric and gravimetric heats of combustion although it is difficult to ignite and its burn rates are relatively low. Augmenting boron ignition and combustion by adding magnesium has been considered in previous work (Liu et al. 2014; Liu, Liu, and He 2015; Pace et al. 1993; DeLuca et al. 2010). However, the results are inconclusive, partially because of difficulties distinguishing reactions of individual components. Magnesium-coated boron powders were added to propellant formulations (DeLuca et al. 2010). Burn rates increased compared to the baseline, however substantial aggregation of particles at the propellant surface was observed. It remains unclear whether the improvement in the burn rate was caused by magnesium alone and whether boron combustion was complete and effective. Magnesium coatings used in early work (Pace et al. 1993) might have oxidized selectively early causing premature aging of the coated samples. Interestingly, magnesium borides were proposed as potential fuels (Guo et al. 2013). However, thermodynamically such fuels are inferior to boron-magnesium composites. In composites on the other hand, where boron and magnesium are in close contact, magnesium can reduce boron oxide present on the surface of boron particles (Sundaram, Logan, and Speyer 1997), so that part of magnesium will become oxidized, and thus inactive.

In recent efforts (Liu et al. 2014; Liu, Liu, and He 2015) mixed powders of Mg and B were studied as the most basic form of a composite material. In such materials, elemental powders may separate from each other when processed into an energetic formulation. An early ignition and relatively rapid combustion of magnesium may consume the oxidizer and further delay ignition of boron, despite an elevated temperature generated by combustion of magnesium. Thus, other types of composite materials are desired, in which boron and magnesium would not separate, would not be chemically bonded, and in which selective oxidation of magnesium would not cause extinction of boron. It is further desired to minimize reaction of magnesium with boron oxide, passivating the material.

Here, a composite B·Mg powder is prepared by mechanical milling. Pre-treatment of boron used as a starting material was focused on partial removal of its natural oxide/hydroxide layer, which could delay boron ignition and/or react with magnesium producing excess of magnesium oxide. Obtained powder particles are fully dense, composite structures, in which boron and magnesium are mixed on the scale of ca. 100 nm. Preparation and properties of such new reactive material powders are discussed.

4.3 Material Preparation

4.3.1 Starting materials

The starting materials used were amorphous boron, 95% pure from SB Boron and magnesium: 99% pure, -325 mesh from Alfa Aesar. For all prepared composite powders, the composition was fixed at nominally 40 wt-% Mg. Several substances were used as process control agent (PCA) during milling, including stearic acid, (Fluka, >97%), acetonitrile, (Alfa Aesar, >99.5%), and hexane (Sigma Aldrich, >98.5%). In addition, acetonitrile, hexane, and toluene (Chempure, >99%) were used to wash and functionalize commercial boron powders. In selected tests, the same solvents were used to wash mechanically milled powders.

4.3.2 Material preparation sequence

The material preparation sequence is illustrated in Figure 4.1. In addition to milling both as-received commercial magnesium and boron powders, milling experiments were performed using boron powders subjected to preliminary treatment. This treatment was focused to remove the natural oxide layer from the surface of boron and functionalize the powder surface to prevent or minimize its following re-oxidation upon exposure to an oxidizing environment. Magnesium was used as received. Removal of MgO layer using solvents is possible; however, it is not clear how to passivate an MgO-free magnesium powder to handle it in the laboratory. Milling was performed using two types of ball mills. For each ball mill, a variety of process control agents was used. Dry milling refers to the experiments using stearic acid as PCA. Wet milling indicates that either acetonitrile or hexane was used as PCA. Finally, washing prepared mechanically milled powders was attempted in an effort to further improve its combustion performance. Specific details for different steps used in the material preparation sequence are discussed below. However, washing mechanically milled powders did not affect their properties, and it is not discussed further.

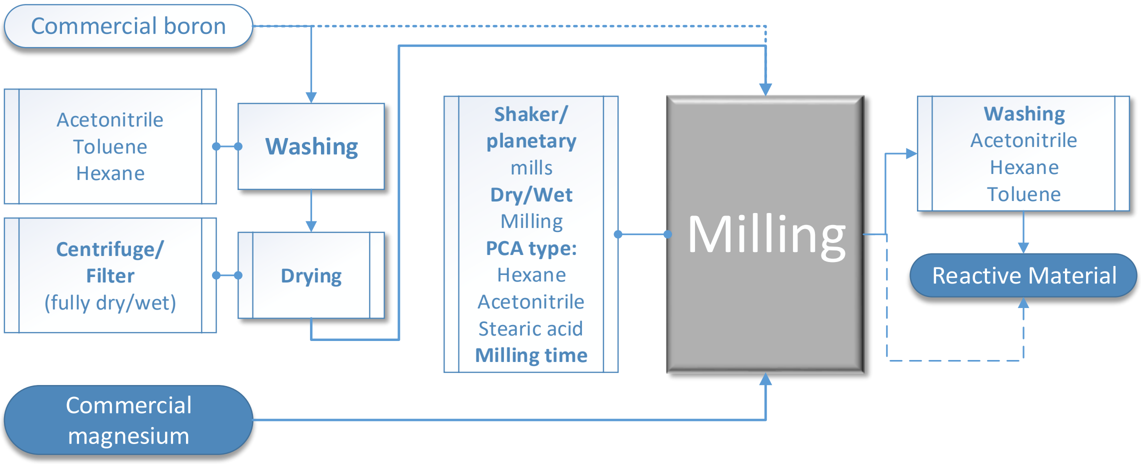

Figure 4.1 Schematic diagram of processes used to prepared mechanically milled B·Mg powders.

4.3.3 Preparation of boron for milling

Acetonitrile was used to wash as-received boron powders in order to partially remove the surface oxide layer following the procedure described elsewhere (Chintersingh, Schoenitz, and Dreizin 2016). Removal of boron oxide or hydroxide was desired in order to minimize their possible reaction with magnesium during milling, and as a result reducing the amount of active magnesium in the composite material. Since boron disperses well in acetonitrile, settling times of the suspensions are unpractically long. Transfer to hexane was desired, as it is chemically similar to alkanes in potential applications (e.g., as part of jet fuels). However, hexane and acetonitrile are immiscible. Therefore, toluene was added, which caused the boron particles to form loose agglomerates and settle rapidly. The solution could then be decanted to separate the dissolved oxide from the powder. The recovered suspension of powder in toluene was finally washed with hexane. For samples to be used in shaker mill experiments, the solvent was removed using a model U8F-1 centrifuge by LW Scientific Inc., operated at 3300 rpm. The sequence included three washing cycles with acetonitrile followed by five cycles with toluene, and two cycles with hexane.

For larger masses required for the planetary mill experiments, the solvent was removed using vacuum filtration. The filtration was conducted using a Büchner funnel (CoorsTek 60240), a 500-ml side-arm flask (PYREX No.5340) and #3 filter paper (Whatman No1033055). Samples were handled under a protective nitrogen environment. The washing sequence included three cycles with acetonitrile and two cycles with toluene. All washed powders were dried in an argon-filled glovebox.

The effectiveness of the described processing for removal of the hydrated boron oxide was assessed earlier using thermo-gravimetric measurements and comparing the mass loss observed at low temperatures (100 – 400 °C) for as received and processed powders (Chintersingh, Schoenitz, and Dreizin 2016). The mass loss, caused by dehydration of $B(OH)_3$ was reduced from 5.7 to 2.6-3.6 %. Assuming that all boron oxide is hydrated, and assuming that no other volatile compounds was present in the processed boron, this implies that the as-received boron contains ca. 7.4 wt.% of oxide; the oxide amount is approximately halved by the present processing. If residual hydrocarbon volatile compounds were present in the ball-milled powder, the weight loss caused by dehydration of the oxide would be smaller than the total measured value, suggesting that even more oxide than estimated above was removed by the processing. The amount of unoxidized boron could not be accessed by the complete oxidation of the powder by thermogravimetry for a combination of reasons. At temperatures above the melting point of boron oxide, a continuous film covers the sample, dramatically reducing the surface area exposed to the gas, and slowing continued oxidation. At the same time, B_2O_3 becomes more volatile at higher temperatures, causing mass loss simultaneous with oxidation. Determining the mass of a completely oxidized material is therefore not feasible: even for the 99% pure boron, the measured mass gain at 1573 K only corresponded to about 58.6% of the expected mass gain for complete oxidation.

4.3.4 Milling details

As-received or washed boron and magnesium in a mass ratio of 60:40 were loaded into milling vials. Case-hardened 3/8" (9.5 mm) diameter carbon steel balls were used as milling media. Materials were prepared in both shaker mill (SM, SPEX Certiprep, 8000 series) and planetary mill (PM, Retsch PM-400 MA) with milling times varied from 1 to 6 hours for each SM and PM. In the shaker mill, the samples were milled in 50-ml flat-end steel vials, cooled by a flow of room air. Each vial contained 5 g of powder, and the ball powder mass ratio was 10. In the planetary mill, samples were milled in 500-mL steel vials; the milling compartment was cooled using an air conditioner. Each vial contained 50 g of powder, and the ball to powder mass ratio was 3. All powders were loaded into the milling vials in an argon-filled glovebox. In different experiments, hexane, acetonitrile, or stearic acid were added as a PCA. For the SM experiments, 15 mL of acetonitrile or 0.1 g of stearic acid were added per milling vial. For PM, the amount of liquid PCA was 140 mL; the amount of stearic acid was 1 g per vial. After milling, all samples were recovered and stored under argon in glass bottles. Milling conditions used for preparation of different samples are summarized in Table.4.1.

Table 4.1 Milling Conditions for B·Mg Composites (B/Mg mass ratio is 60:40)

Sample Identifier	Milling Method	Boron	Milling times, hr	Ball to powder mass ratio
Blend	SM	Commercial	0.5	No balls
SM	SM	Commercial	1 – 6	10
WSM	SM	Washed*	4	10
PM	PM	Commercial	1 – 6	3
WPM	PM	Washed*	4	3

*Different washing sequences were used as discussed for specific samples

4.4 Characterization of the Prepared Powders

Starting materials as well as milled powders were examined using a Field Emission Scanning Electron Microscope model LEO 1530 FESEM with Oxford Energy Dispersive Spectroscopy detector, EDS. A PANalytical Empyrean diffractometer operating at 45 kV and 40 mA and using unfiltered Cu K_a radiation (l = 1.5438 Å) was used for X-ray diffraction (XRD) analysis of compositions of the prepared materials. The patterns were collected between 10 and 90° at a rate of 0.625°/min. Oxidation of B-Mg alloy was studied by thermo-gravimetric (TG) analysis using a TA instruments model Q5000IR TG analyzer and Netzsch Simultaneous Thermal Analyzer STA409 PG. The samples were heated in oxygen to 1000 °C at heating rates of 2 and 5 K/min. The mass of the samples varied from 2 to 7 mg.

Customized experiments used for characterization of ignition and combustion of the prepared powders are illustrated in Figure 4.2. All experiments were performed in air. Ignition temperatures were measured at different heating rates using a heated filament ignition setup (Ward et al. 2006a). Powders were coated and ignited on an electrically heated nickel-chromium filament. The details of the experiment are described elsewhere (Ward et al. 2006a; Aly and Dreizin 2015; Aly, Schoenitz, and Dreizin 2013; Shoshin et al. 2006a; Zhang et al. 2012). The filament was heated by a DC current. Heating rates varied between 2000 and 30000 Ks. The wire temperature was measured by an infrared pyrometer. The time of ignition was identified from videos recorded using a high-speed camera (MotionPro500 by Redlake) at 500 fps or from a separate photo-diode signal produced by the ignited powder.

Powders were burned in a constant volume explosion (CVE) setup described in detail earlier, e.g., (Santhanam et al. 2010). The chamber volume was 9.2 L, and the powder mass load was 4.65 g in each run. A custom igniter using a nanocomposite Al-Fe_2O_3 thermite was mounted at the center of the chamber. The powder was injected into the chamber with an air blast from a high pressure reservoir. The igniter was initiated after a 300-ms delay following the air blast; the pressure produced by the burning powder cloud was measured using a pressure transducer.

Powders were also ignited and burned using an electrostatic discharge (ESD) as an initiation source. The apparatus was described in detail elsewhere (Williams, Patel, and Dreizin 2014). It uses a model 931 Firing Test System by Electro-Tech Systems, Inc. ESD was produced discharging a 10,000 pF capacitor charged to 10 kV. The powder was placed in a sample holder forming a 0.5-mm thick layer. Powder mass removed from the sample holder after each experiment was determined by weighing the loaded sample holder before and after each test. Experiments were performed in a sealed chamber filled with air and equipped with a piezoelectric pressure transducer.

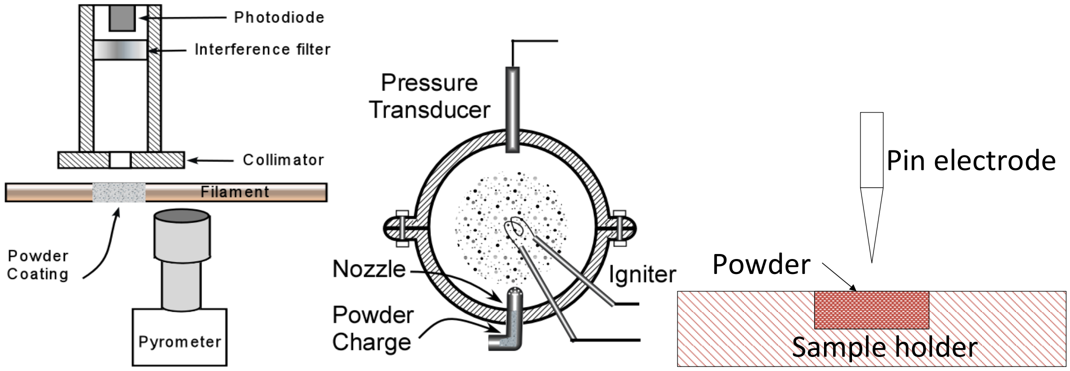

Figure 4.2 Experimental techniques used to assess reactivity of the composite powders: left to right: heated filament ignition, constant volume explosion, electrostatic ignition.

4.5 Results

FESEM images of the starting boron and magnesium powders as well as of a prepared composite material are shown in Figure 4.3. In the images taken with backscattered electrons, magnesium appears brighter than boron.

Boron powder consists of heavily agglomerated submicron sized primary particles. The agglomerate sizes vary in the range of 1 to 20 µm. Magnesium particles are much coarser, varying in size roughly between 10 and 40 µm. The composite powder also consists of agglomerated, submicron sized primary particles, morphologically similar to the starting boron. Magnesium is reduced in size substantially and mixed with boron, so that each agglomerate particle includes well mixed and densely packed boron and magnesium particles, which can be distinguished in Figure 4.3 by their brightness. The sizes of primary boron particles are not reduced noticeably; however, they are homogeneously mixed with magnesium.

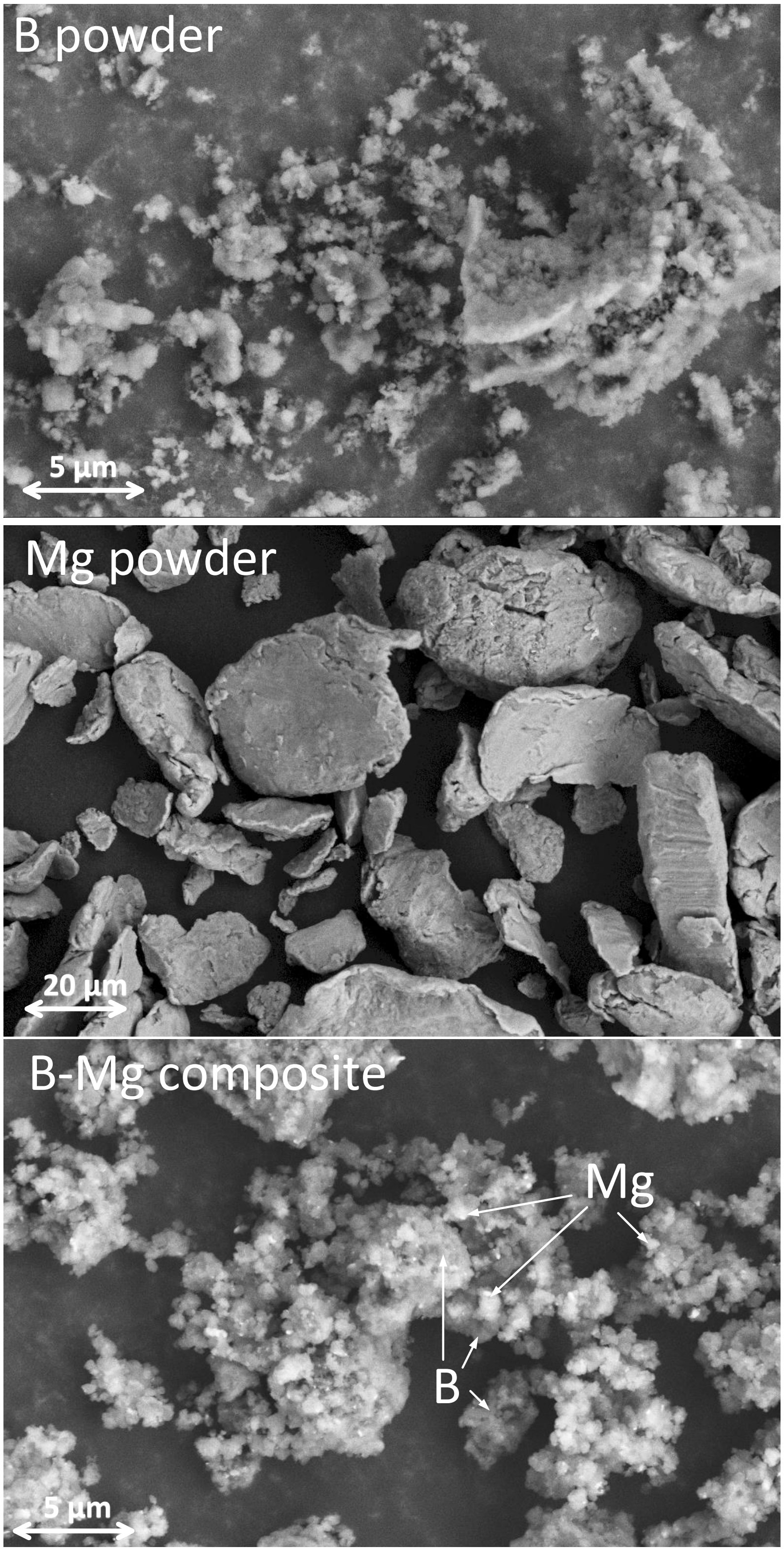

Figure 4.3 SEM images of the starting powders and composite B·Mg powder. The composite powder was milled for 4 hours in the planetary mill using stearic acid.

The structure of the composite materials observed in Figure 4.3 is further supported by images of cross-sectioned particles, such as shown in Figure 4.4. Boron particles, which appear darker, are embedded in a lighter matrix formed by agglomerated magnesium. The boron is distributed nearly homogeneously throughout the cross-section. In addition, fine bright inclusions are apparent, representing iron contamination from the milling media. The presence of iron was unintended but was unavoidable when steel milling tools were used. It could affect ignition and combustion characteristics of the prepared powders.

Elemental maps of boron, magnesium, and oxygen were also taken using energy-dispersive x-ray spectroscopy. The maps are omitted for brevity; they show that the distributions of oxygen and magnesium are well correlated with each other. Boron inclusions appeared to be oxygen-free.

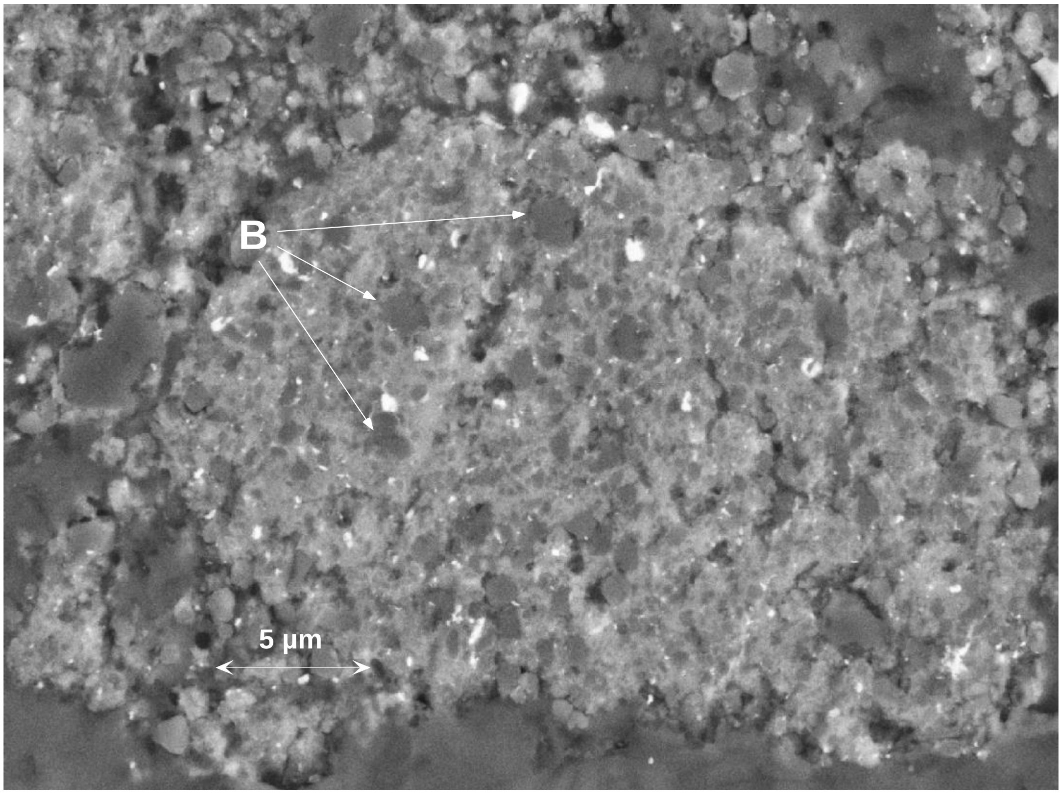

Figure 4.4 An image of cross-sectioned composite B·Mg powder sample. The composite powder was milled for 4 hours in the planetary mill using stearic acid.

XRD patterns for the blended powders and powders milled in the shaker and planetary mills are shown in Figure 4.5. The peaks of magnesium are prominent in the pattern for the blended sample. Residual crystallinity in the amorphous boron used in this work produced weak XRD peaks below 20 °2q. Weak peaks of B_2O_3 indicate small amounts in material from the planetary mill, possibly indicating less effective separation of the solvent by filtration. In the milled samples, peaks of Mg became broader and weaker, suggesting reduced crystallite sizes at longer milling times. In addition, peaks of MgO were detected, most likely produced as a result of reaction between Mg and boron oxide and hydroxide present on surface of the boron powder particles. Formation of MgO is undesirable. Peaks of iron also appear indicating a contamination of the sample by the milling media, consistently with the SEM image shown in Figure 4.4. Such contaminations are common for the materials prepared by ball milling. The iron contamination increased dramatically for the sample milled for 6 hours, with the iron peak becoming stronger than the peaks of magnesium. Note that MgO peaks did not increase substantially at longer milling times, so that they are not well resolved for the pattern for the sample milled in the shaker mill for 6 hours shown in Figure 4.5.

There was no difference between the XRD patterns characterizing composite materials prepared using as received or washed boron powders.

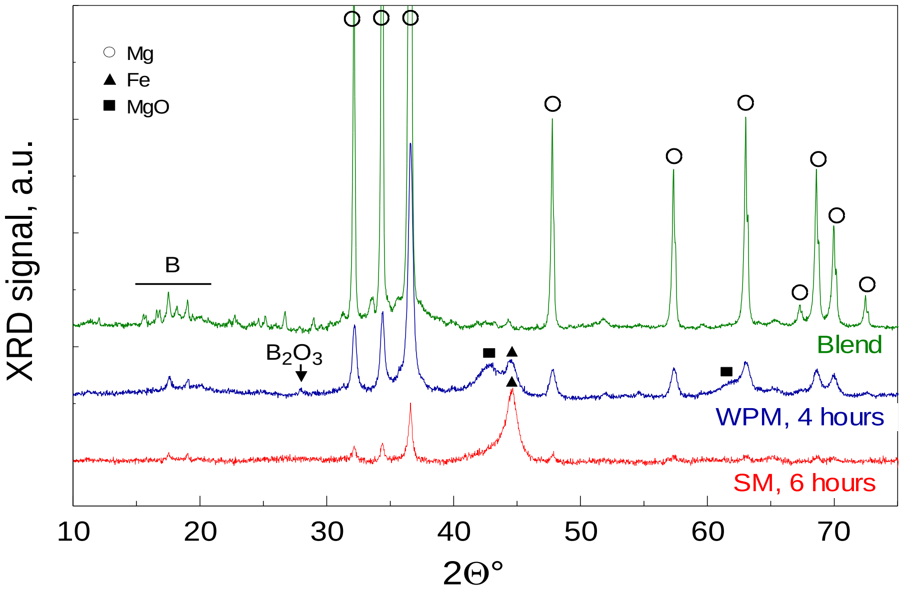

Figure 4.5 XRD patterns for blended and milled B·Mg powders.

Initially, materials were prepared using different milling times in the planetary mill. The milling time necessary to prepare the most promising composite was determined based on comparison of the oxidation TG traces for different samples, as shown in Figure 4.6. For reference, a TG trace measured for the oxidizing powder blend is also shown. For all powders, a mass loss occurs at low temperatures; it is specifically labeled in Figure 4.6 for the sample milled for two hours. It is likely caused by dehydration of boron hydroxide, originally present on the surface of boron particles. The mass loss is followed by a mass gain signifying oxidation, which occurs in two distinct steps for all milled powders. Thus, the first oxidation step likely represents selective oxidation of Mg. The first oxidation step is not well resolved for the powder blend, which is consistent with earlier work, suggesting that the onset of oxidation for micron-sized magnesium powders heated at the same rate occurs at a higher temperature than observed here (Nie, Schoenitz, and Dreizin 2016). The shift of selective oxidation of magnesium to lower temperatures can be associated with an increase in surface area as a result of ball milling. The second oxidation step necessarily involves oxidation of boron, because the mass increase is greater than an estimated 26.3 % caused by the complete oxidation of all magnesium present in the material.

Considering the onset temperatures and respective mass changes for the two observed oxidation steps as a function of the milling time is useful to select the milling time yielding the most reactive composite material. The materials that are more reactive oxidize at lower temperatures and to a greater completeness. Such materials exhibit stronger mass gain steps observed at lower temperatures when heated in an oxidizing environment. An increase in reactivity can be associated with a finer mixing structure achieved in the composite. This structure is expected to be attained at a specific milling time: shorter milling does not yield a well-mixed homogeneous composite; a longer milling can result in partial reaction between milled materials; it also is associated with an increased contamination of the material with iron from the milling tools. Onsets for each oxidation step obtained as inflection points of the measured TG curves along with the respective mass changes are shown in Figure 4.7. The error bars for the temperatures showing onset of the second oxidation step are smaller than the symbol size. Different methods were explored to identify the onset for oxidation steps, including identifying changes in the absolute value or slope of the TG curves. The results were qualitatively similar for all types of processing, while using the inflection point of the TG curve appeared to offer the most objective approach. The onset temperature for the first oxidation step decreases with the increase in the milling time. This is most likely associated with the reduced scale of mixing achieved at longer milling times. The onset temperature for the second step does not change as significantly, but it is the lowest for the sample milled for 4 hours. In addition, the relative mass changes observed for both first and second oxidation steps have peaks for the sample milled for 4 hours. Based on these observations, 4 hours was selected as the preferred milling time for materials used in the following experiments.

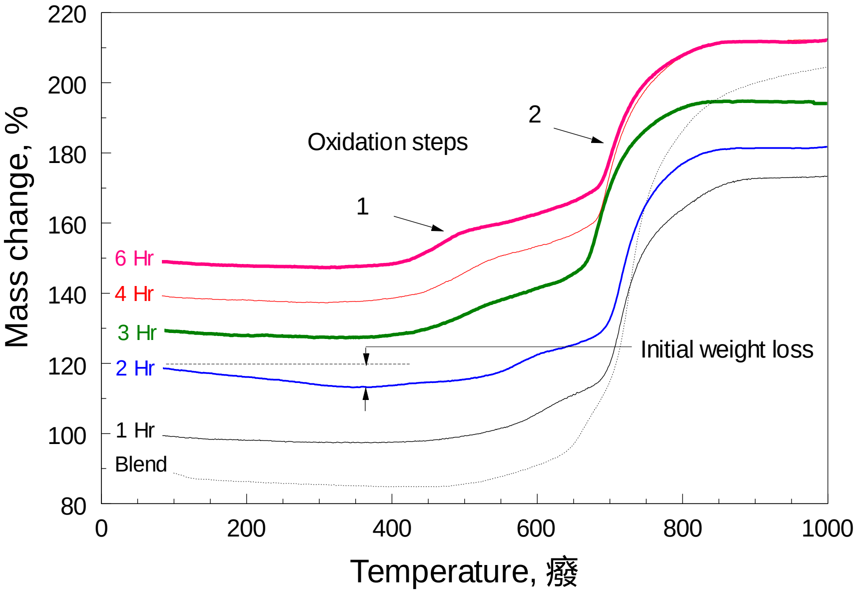

Figure 4.6 TG traces for samples prepared using different milling times and heated at 5 K/min. Materials prepared using planetary mill; as-received boron was used. Stearic acid was used as PCA. The traces are shifted vertically for clarity.

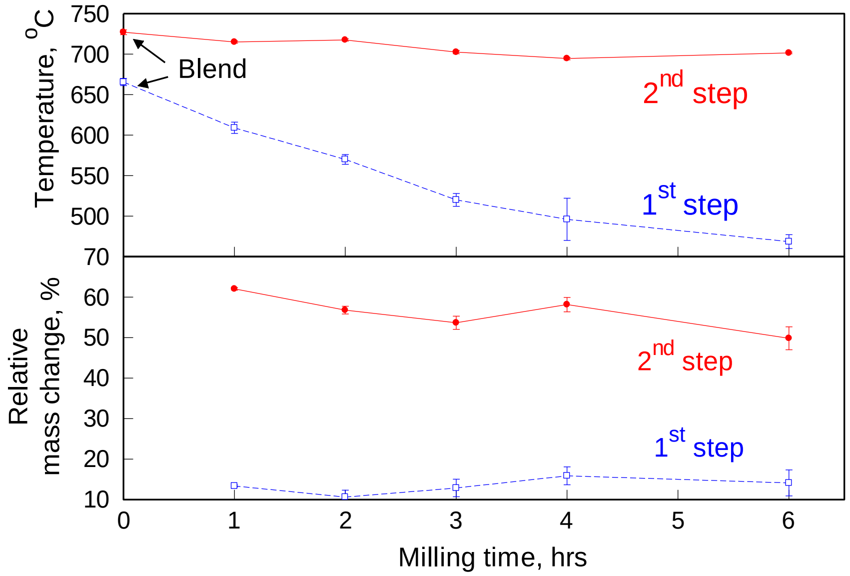

Figure 4.7 Onset temperatures and respective percent of mass change obtained from TG traces for the oxidation steps for samples prepared with different milling times. Materials prepared using planetary mill; as received boron was used. Stearic acid was used as PCA.

TG traces for the samples prepared using both as-received and washed boron are compared to each other in Figure 4.8. The composite material prepared using as-received boron exhibits a mass loss at low temperatures, consistent with that seen in Figure 4.6. No such mass loss is observed for the sample using the washed boron. It is also noted that the first oxidation step is stronger for the material prepared using the washed boron (ca. 22 wt % vs. 17 wt % for the sample using as-received boron). The onset temperature for the first oxidation step is not affected by the type of boron used. The magnitude of the second step is similar for the two prepared samples. These improvements in reactivity may be attributed to a reduction in the amount of boron oxide and/or hydroxide for the washed boron and thus to a smaller amount of Mg reacting with boron oxide and/or hydroxide during milling.

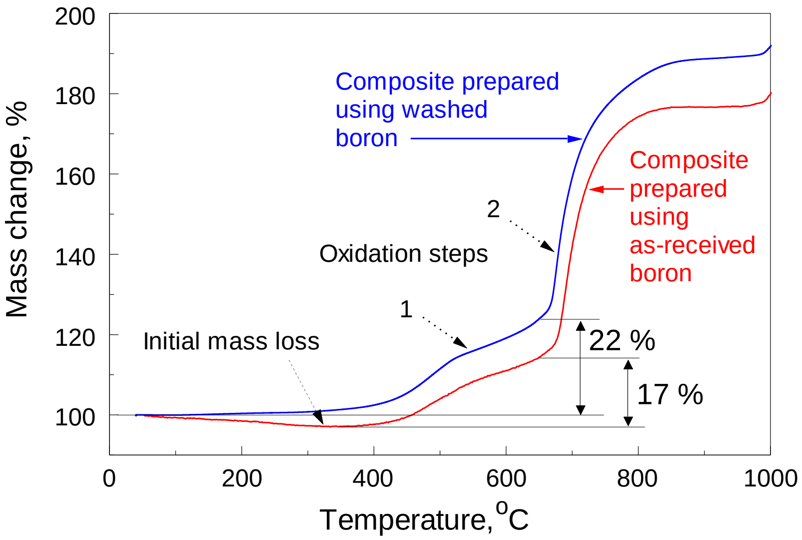

Figure 4.8 TG traces for B·Mg composite powders prepared in the planetary mill using as received and washed boron powders (samples PM and WPM). Milling time is 4 hours, stearic acid used as PCA.

Milling using acetonitrile as a PCA was attempted in order to further reduce the presence of boron oxide in the milled material. The TG traces for the samples prepared using the planetary mill and employing both stearic acid and acetonitrile as PCA are shown in Figure 4.9. Although the second oxidation step was substantially faster for the sample milled with acetonitrile, the initial mass loss was also significantly larger. The same effect was observed for powders prepared using the shaker mill.

The accelerated oxidation suggests that the original boron oxide/hydroxide layer covering the starting boron powder was effectively compromised. However, the increased initial mass loss is likely due to ineffective separation of the dissolved oxides from the milled powder. Interaction between acetonitrile and the milled elements, and the possible formation of complex metal-organic products also can not be ruled out. The separation problem could not be overcome in the present work, and thus no further samples were prepared using acetonitrile as PCA. Both, rates of reaction and the changes in mass were lower for the samples prepared in the shaker mill, compared to those prepared using the planetary mill. Respectively, samples prepared in the planetary mill were used in the ignition and combustion experiments discussed below.

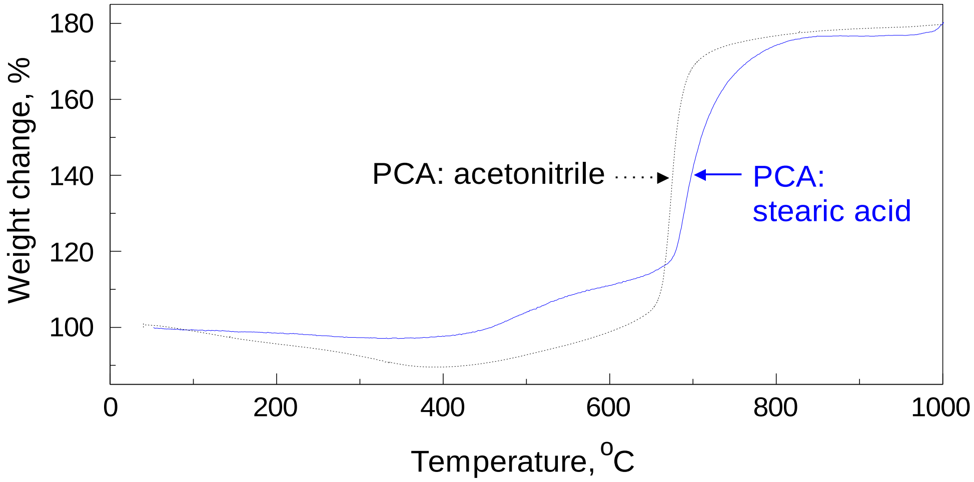

Figure 4.9 TG traces for samples prepared using stearic acid vs. acetonitrile as PCA. Both samples were prepared using the planetary mill with 4 hours milling time.

Ignition temperatures were measured in the heated filament experiment while varying the heating rate for the composite powders as well as for the powder blend. Ignition temperatures measured at heating rates of 20±8 $\times 10^3$ K/s are shown in Figure 4.10. The error bars show standard deviations over at least 7 measurements for each material. The blend ignited at about 1140 °C. This temperature is determined by ignition of the micron-sized magnesium powder. The ignition temperature was reduced by about 100 °C for the milled powders, which is consistent with the reduced temperature of the first oxidation step, representing selective oxidation of magnesium. The composite prepared using the washed boron ignited at a slightly lower temperature compared to the material prepared with as-received boron powder. Not shown are samples prepared using the shaker mill, which ignited at temperatures slightly higher than their analogs prepared using the planetary mill.

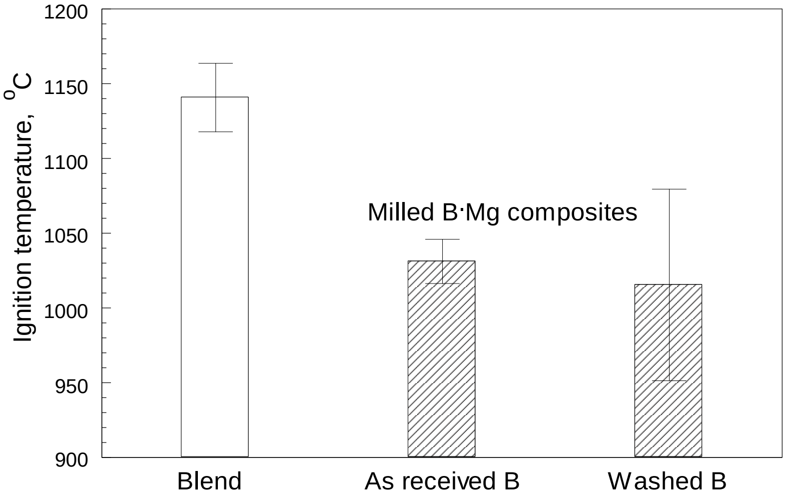

Figure 4.10 Ignition temperatures of the B-Mg powder blend and composite B·Mg powders prepared using planetary mill using both as-received and washed boron powders; milling time was 4 hours, stearic acid was used as PCA.

Both, heated filament ignition temperature measurements and data obtained from TG traces and characterizing onset temperatures for the first and second oxidation steps are summarized in the Kissinger plot (Kissinger 1957) in Figure 4.11. The presented data are not meant to quantify the reaction kinetics; rather it was of interest to see whether ignition temperatures can be correlated with one of the observed oxidation steps. A direct extrapolation of neither trend obtained from the TG measurements at low heating rates points to the range of ignition temperatures. This likely suggests that ignition is driven by more than one process observed in TG, and that additional reactions might be triggered at high heating rates, which are undetectable or insignificant in the TG measurements. The second oxidation step observed in the low-heating rate TG experiments occurs in the same temperature range as ignition, observed at much higher heating rates. Therefore, it is very unlikely that the second oxidation step plays any role in causing the powder ignition. Conversely, the first oxidation step occurs at substantially lower temperatures, and thus it is possible that this reaction assists ignition of the rapidly heated powders.

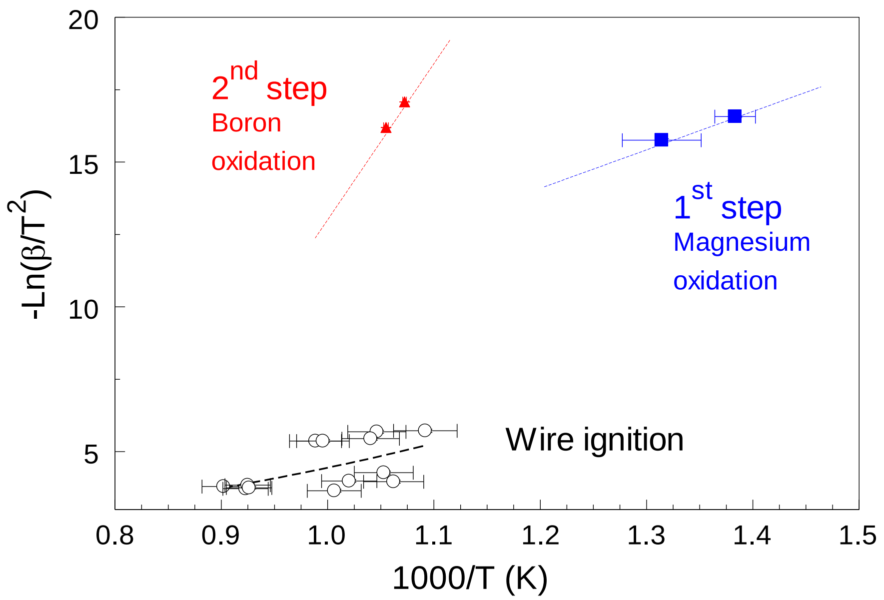

Figure 4.11 Kissinger plot for B·Mg composite powders prepared in planetary mill combining ignition data with onset temperatures for the first and second oxidation steps. Washed boron was used; milling time was 4 hours, stearic acid served as PCA.

Figure 4.12 compares the results of the CVE experiments between composites prepared with washed vs. as-received boron. Powder blends did not ignite. Shown are the ratios of maximum pressure to initial pressure in the chamber (typically, 1 atm), P_{max}/P_{ini}, and the maximum rate of pressure rise, dP/dt_{max}. The former represents the energy released in the explosion, and the latter shows the rate of reaction. Results are shown for the samples prepared in planetary mill. No substantial effect of washing boron prior to preparing the composite powder is noted. Most likely, the effect is smaller than can be identified from the obtained data with the relatively large error bars. The measured pressure rise can be compared to that predicted for the reactive material by a calculation assuming that the reaction occurs adiabatically and yields thermodynamically favorable products using a NASA CEA code (McBride and Gordon 1996). The calculated pressure rise is 11.43 atm, suggesting that the combustion efficiency is close to 58 %. A separate calculation was performed treating boron powder as an inert material; that calculation predicted the pressure rise of 7.04 atm, which is close to that observed in the experiments. However, in a recent study (Abraham et al. 2016), CVE experiments were performed with the same 4.65-g mass load of pure Mg powder. The maximum experimental pressure was only 5.4 atm. Because a higher pressure was observed in the present experiments, where each load contained much less magnesium, it is certain that boron combustion contributed to the observed pressure rise.

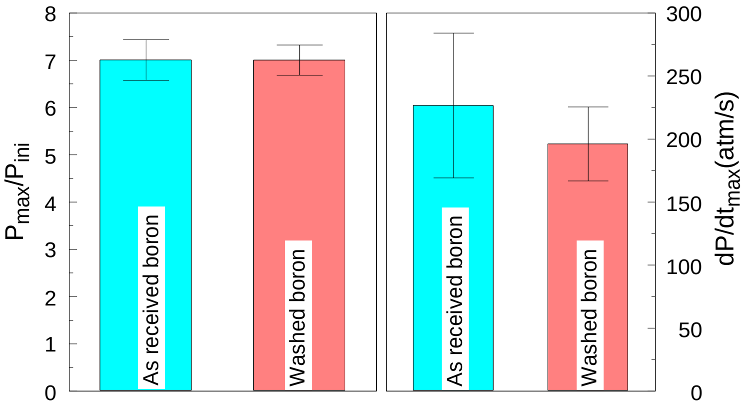

Figure 4.12 Results of CVE experiments with composite materials prepared in the planetary mill (samples PM and WPM). The labels show type of boron used to prepare composites.

Characteristic pressure traces recorded in the ESD ignition tests are shown in Figure 4.13. As in the CVE experiments, powder blends did not ignite. The pressure increase several milliseconds after the spark shows ignition of an aerosolized powder cloud (Monk, Schoenitz, and Dreizin 2016b; Williams, Patel, and Dreizin 2014). The pressure peak positions in the range of times of ca. 40 – 80 ms suggest the times for complete combustion of the aerosolized powder. Two pressure traces shown in Figure 4.13 represent typical samples prepared using the planetary mill with both as-received and washed boron powders. It is observed that the ignition delay is shorter, the pressure peaks sooner, and the peak pressure is higher for the sample prepared using washed boron powder. Monitoring the mass of the loaded sample holder before and after the experiment showed that slightly more powder was typically ejected for the sample prepared using the washed powder. When the maximum pressures were normalized by the mass of the ejected powder, the results became essentially the same for both materials. Comparison of temporal peak positions for multiple runs showed that the effect noted in Figure 4.13 was sustained, i.e., the powder prepared using the washed boron generated peak pressures at consistently shorter times, 46.8±10 ms vs. 58.6±8.3 ms for the powder prepared using as-received boron.

In an additional experiment, pure Mg powder was ignited by ESD and respective pressure signals were recorded. The pressure was normalized per gram of Mg powder lifted from the sample holder. It was then compared to the pressure produced by the ignited composite material, also normalized per mass of the lifted powder and accounting for the mass fraction of magnesium there. Thus, the maximum pressures were obtained per gram of Mg for both pure Mg (2450 kPa/g Mg) and composite powder (6890 kPa/g Mg). The composite material produced a substantially higher pressure, suggesting a significant contribution of boron to the generated combustion energy, a result consistent with that discussed earlier for the CVE experiments.

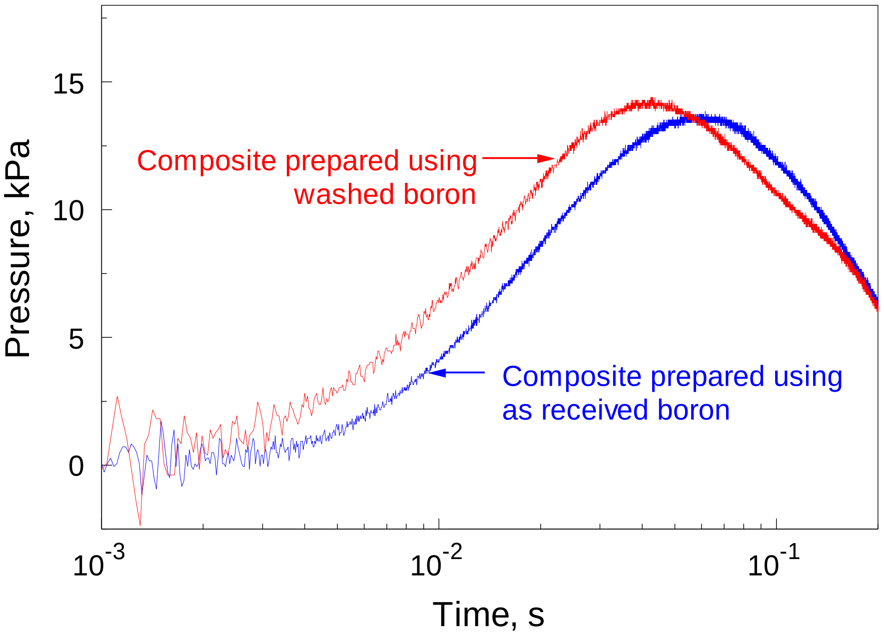

Figure 4.13 Pressure traces obtained with the composite B·Mg powders prepared using planetary mill and ignited using electrostatic discharge (samples PM and WPM).

4.6 Discussion

Milling changes structure and properties of the composite B·Mg powders. The first oxidation step caused by the selective oxidation of Mg shifts to consistently lower temperatures at longer milling times (Figs. 4.6 and 4.7). This suggests an increasingly greater reactive surface for magnesium due to its refinement in the composite structure. However, the mass changes observed for both first and second oxidation steps decrease for milling times exceeding 4 hours in the present PM experiments. The temperature of the second oxidation step also becomes slightly higher at such longer milling times. These observations suggest that formation of magnesium boride becomes significant, making the milled material less attractive as a high energy density fuel. Magnesium boride is more stable thermodynamically than nanocomposite B·Mg and thus may be more difficult to ignite. The heat of combustion will also be reduced by the heat of formation of the magnesium boride, -91.96 kJ/mol (Chase 1998), about 17% of the heat of magnesium oxidation. Thus, selection of the appropriate milling conditions is important; in the present efforts, the milling time of 4 hours using the planetary mill and yielding the most attractive material corresponds to the milling dose of 12 hours, calculated as product of ball to powder mass ratio and the milling time, following (Ward et al. 2005; Santhanam and Dreizin 2012). The milling dose is proportional to the energy transferred to the material from the milling tools. It is independent of the type of the mill used as long as the energy of individual impacts causing the energy transfer exceeds a certain threshold necessary to achieve plastic deformation of the powder particles being milled. For the SM-prepared materials, the milling dose varied from 10 to 60 hours, with a step of 10 hours, depending on the milling time. Hence, all materials, except for those milled for 1 hour were processed longer than necessary, causing a partial reaction between boron and magnesium. The milling dose for the 1-hour SM sample was 10 hours, which is less than 12 hours needed for the optimized material. This explains the observed lower reactivity for the SM-prepared materials as compared to the PM-prepared powder milled during 4 hours.

Acetonitrile serving as a solvent to treat the commercial boron powder, removes, at least partially, oxidized and hydrated surface layer. Subsequent washing boron in toluene and hexane helps to effectively separate the dissolved oxides, and to prevent extensive re-oxidation in ambient air, most likely because of formation of carbon-containing molecular complexes at the boron surface. It is of interest to understand the nature of such complexes better, which could be a focus of a future research effort. Using acetonitrile as a PCA during milling apparently makes boron even more reactive, as noted by a very sharp and strong second oxidation step observed in Figure 4.9. However, a significant low-temperature mass loss observed for the same sample suggests that effective separation of the dissolved oxides is more difficult, or reactions between acetonitrile and boron and/or magnesium. The products of this reaction become unstable and decompose while the sample is being heated. This decomposition must be an endothermic process, undesirable for the materials expected to ignite readily upon heating. Therefore, acetonitrile should be used as a solvent, but not a PCA for milling.

Mechanically milled composite B·Mg powders ignite at a lower temperature than the pure Mg serving as a starting material (Figure 4.10). This result correlates with the reduced temperature of magnesium oxidation observed in the TG measurements. Therefore, ignition is likely to be primarily driven by selective oxidation of magnesium, which occurs earlier in the milled material because of its developed Mg surface area produced by milling. This hypothesis is further supported by comparison of kinetic trends for the two oxidation step and ignition temperature, as illustrated in Figure 4.11.

The benefits of washing the commercial boron powder with acetonitrile before preparing the composite materials are best illustrated in Figs. 4.8 and 4.13. The initial mass loss caused by removal of the hydrated boron oxide layer during the sample heating is reduced after the boron powder is washed. It is also observed that the ignition initiated by ESD occurs consistently faster for the samples prepared using the washed boron. No significant differences in the ignition and combustion characteristics were observed for samples prepared using washed and as received boron in both the heated filament ignition and CVE experiments. A principal difference of the ESD ignition from other experiments is a very high heating rate generated by the spark. At lower heating rates, in the filament ignition tests and CVE flame propagation, substantial vapor pressure of Mg could have been built during powder heating, to make the vapor-phase oxidation of Mg a substantial heat source leading to temperature runaway and ignition. The vapor-phase oxidation of magnesium would be unaffected by the presence of an oxidized boron surface or even an increased concentration of MgO in the material. At the high heating rates provided by ESD, evaporation of Mg is expected to be negligible. It is most likely that heterogeneous reactions led to ignition in that case. The heterogeneous reactions are expected to occur faster for the samples prepared using the washed boron, in which MgO formation during milling was reduced because of the reduced amounts of boron oxide and hydroxide.

Finally, it is important to emphasize that comparisons with reference experiments employing pure Mg powder for both ESD-ignition and CVE show the evidence of boron combustion. Thus, for the prepared composite materials, selective oxidation of magnesium, leading to ignition does not impede, but instead assists continuing boron oxidation.

4.7 Conclusions

Attractive mechanically milled B-Mg composite powders with 40 wt-% Mg are prepared using a milling dose of 12 hours. Ignition of these powders is caused by selective oxidation of magnesium, but ignition temperatures are lower than those of pure magnesium. Following the ignition, boron continues to react, contributing to the released combustion heat and pressure generated by the flame. Washing a starting commercial boron powder used to prepare the composites with acetonitrile helps removing its surface oxide layer, which reduces formation of MgO when boron and magnesium powders are ball milled. An increased amount of reactive Mg in the prepared composite and reduced amount of boron oxide and hydroxide diminish an endothermic loss of moisture from the heated powder and lead to a stronger first oxidation step due to the selective Mg oxidation. Both effects are accelerating the heterogeneous oxidation of magnesium leading to the powder ignition. Heterogeneous reactions are particularly important for the composite powders exposed to a high-heating rate initiation source, such as an electric spark.

CHAPTER 5

BORON-BASED REACTIVE MATERIALS WITH HIGH CONCENTRATIONS OF IODINE AS A BIOCIDAL ADDITIVE

5.1 Abstract

Metal-based iodine-bearing reactive materials are of interest as additives to energetic formulations aimed to defeat biological weapons of mass destruction. This work was aimed to develop a material including a boron-based thermite with the maximized iodine concentration. The thermite was prepared mechanochemically, and $Ca(IO_3)_2$ served as an oxidizer. First, a $B{\cdot}I_2$ composite powder was prepared starting with 40 wt% of iodine. This composite retains up to 30 % of iodine, which is released in three steps upon heating. The main iodine loss occurs at temperatures exceeding 673 K (400 °C). The binary $B{\cdot}I_2$ powder was used as a starting material to prepare the final thermite with the total concentration of iodine of 57.6 wt %. The thermite comprises loose agglomerates with particle sizes in the range of 1 – 10 µm, with submicron boron-iodine particles embedded in $Ca(IO_3)_2$. Combustion tests of the ternary composite thermite powder in an air-acetylene flame showed the flame temperatures close to 2050 K, and solid residue in the form of fine oxidized spheres with boron and calcium oxides mixed homogeneously. A correlation between particle sizes and their burn times is reported as well.

5.2 Introduction

Specialized agent-defeat munitions are needed to neutralize stockpiles of chemical and biological weapons (Eneh 2012). Bio-agent defeat often relies on halogens. In particular, compositions releasing iodine have been explored recently (He, Zhang, and Shreeve 2013b;

Vo et al. 2013). Metals are included in explosives to increase their energy density, and thus reactive materials combining highly exothermic metallic fuels with iodine have been studied as potential components of advanced explosive formulations, e.g., (Abraham et al. 2014; Aly et al. 2014; Zhang et al. 2012; Zhang, Schoenitz, and Dreizin 2010a, 2010b). Although such materials must be stable at room temperature and easy to handle, they should burn rapidly and release copious amounts of iodine in order to be of practical interest (Henderson et al. 2015).

Previous research showed that that iodine could be mechanochemically stabilized in metal-based powders (Zhang et al. 2012; Grinshpun et al. 2012; Zhang, Schoenitz, and Dreizin 2010a; Wang et al. 2016; Abraham et al. 2015). It was found that up to 20 wt. % of iodine can be stabilized in aluminum. Both, binary $Al{\cdot}I_2$ and ternary composites, e.g., $Al{\cdot}B{\cdot}I_2$, containing 20 wt. % of iodine were described and characterized. Kinetics of iodine release upon heating a ternary $Al{\cdot}B{\cdot}I_2$ composite suggests that iodine can be partially retained in both aluminum and boron (Abraham et al. 2015). However, the maximum concentration of iodine that can be retained in a mechanochemically prepared binary $B{\cdot}I_2$ composite was not established.

In addition to including iodine as a component of a metal fuel, iodine can be effectively included in reactive materials as part of an oxidizer. For example, extensive studies addressed thermites using I_2O_5 as an oxidizer (Clark and Pantoya 2010; Farley and Pantoya 2010; Feng et al. 2013; Martirosyan 2011). While very reactive, this oxidizer is also hygroscopic and thus is difficult to handle in ambient air. Other iodine-rich oxidizers were suggested (Johnson and Higa 2013; Sullivan et al. 2011b, 2011a), some of which, e.g., calcium iodate, $Ca(IO_3)_2$, are more stable and easier to work with than iodine pentoxide (Ruz-Nuglo and Groven 2015a). Recently, thermite samples combining commercial aluminum or boron with $Ca(IO_3)_2$ were prepared and characterized (Wang et al. 2017a).

This work is aimed to determine the maximum iodine concentration that can be retained in a binary, $B \cdot I_2$ composite, and to combine such a composite with a stable, iodine rich oxidizer $Ca(IO_3)_2$ to prepare an energetic composition with the maximized iodine concentration.

5.3 Materials and Experimental Techniques

A commercial 95-% pure amorphous boron powder by SB Boron was used in this work to prepare all boron-iodine composite materials. For some samples, it was preliminarily functionalized by washing it in acetonitrile (99.5% pure by Alfa Aesar), generally following the methodology described elsewhere (Chintersingh, Schoenitz, and Dreizin 2016). This processing removes $B(OH)_3$ and partially dissolves B_2O_3 from the powder particle surfaces. To enhance washing, the suspension of boron in acetonitrile was ultrasonicated using a titanium horn powered by a 20-kHz Branson 910BC system following the procedure established recently (Liu et al. 2017). The suspension stratified, with the bottom layer representing the cleanest boron, which was loosely agglomerated. The material from the bottom layer was separated and dried in argon. This processed powder has its particle surface functionalized as a result of reaction with acetonitrile, protecting the powder from rapid re-oxidation upon its exposure to room air (Liu et al. 2017).

Both, as-received and functionalized boron powders were further milled with iodine (99% pure chips from Sigma Aldrich) in a shaker mill (SM) by SPEX Certiprep, 8000 series. For reference experiments, a commercial boron oxide (99.98% pure by Alfa Aesar) was also milled with iodine. Milling experiments used flat-ended steel vials and 3/8” (9.5 mm) diameter carbon steel balls. Each vial contained 5 g of powder and 50 g of balls, so that the ball to powder mass ratio (BPR) was set to 10. No process control agent was added. Compositions with the initial concentrations of iodine of 30, 40, and 50 wt. % were prepared. The milling times were set to 2, 4, and 6 hours. Milling vials were sealed in a glovebox under argon before milling. The vials with milling products were also opened in the same glovebox. The recovered powder was stored in closed but not sealed glass bottles. A list of the prepared binary boron-iodine samples with their respective milling conditions is given in Table 5.1.

Table 5.1 Prepared Boron-iodine Composite Samples

Sample Identifier	Boron	Iodine concentration, wt%	Milling times, hr
C-B$_{70}$I$_{30}$-4	Commercial	30	4
C-B$_{60}$I$_{40}$-2	Commercial	40	2
C-B$_{60}$I$_{40}$-4	Commercial	40	4
C-B$_{60}$I$_{40}$-6	Commercial	40	6
C-B$_{50}$I$_{50}$-6	Commercial	50	6
F-B$_{70}$I$_{30}$-4	Functionalized (washed in acetonitrile)	30	4
F-B$_{60}$I$_{40}$-4	Functionalized (washed in acetonitrile)	40	4
B2O3$_{60}$I$_{40}$-4	Commercial*	40	4

*Commercial B_2O_3 was used instead of Boron

Following characterization of the samples descried in Table 5.1 (see results below), C-B$_{60}$I$_{40}$-4 was selected as the most promising binary material. It was combined with $Ca(IO_3)_2$ (98% pure, from Sigma Aldrich) to prepare a thermite. The thermite was prepared by milling the starting components for 1 hour in custom-made high-pressure vials using a planetary mill (Retsch PM-400 MA). Each powder batch contained 21.6g of $Ca(IO_3)_2$ and 8.4g of C-B$_{60}$I$_{40}$-4, yielding product with a total of 57.6 wt% of iodine. This thermite composition has an equivalence ratio of 2.24 (B:$Ca(IO_3)_2$). The BPR was set to 10; the same steel balls as described above were used. In each vial, 15 mL of n-hexane (95% pure from Alfa Aesar) was used as a process control agent. As before, the milling vials were sealed and opened inside an argon-filled glovebox. Prepared thermite powders were dried and stored in glass vials.

Thermo-gravimetric (TG) analysis was used to test the stability of binary boron-iodine materials using a TA instrument model Q5000IR analyzer. The samples were heated to 900 °C in argon at a rate of 5 °C/min. The purge flow of argon was 10 mL/min, and sample flow of argon was 20 mL/min. No TG measurements were performed for thermite samples to minimize the contamination of the furnace with highly corrosive iodine vapors.

Prepared thermite powders were examined using a LEO 1530 Field Emission Scanning Electron Microscope (SEM). SEM images were used to obtain particle size distributions of the prepared thermites, necessary for interpretation of combustion experiments.

A 532nm Thermo Fisher Scientific DXR Raman Microscope was used to detect the surface molecular structure and composition of boron-iodine materials.

Combustion of thermite particles was studied by injecting them into an air-acetylene flame, following the methodology described in detail elsewhere (Corcoran, Hoffmann, and Dreizin 2013; Corcoran et al. 2015). Powder samples were loaded on a screw feeder and injected axially into a premixed flame using nitrogen carrier gas. The gas flow rate of nitrogen was 2 standard cubic feet per hour (SCFH). The powder entered the flame through a 2.38-mm diameter tube at a speed of 6 m/s. The premixed flame was obtained combining compressed air fed at 10 SCFH and acetylene fed at 0.9 SCFH. The equivalence ratio of the flame was 1.65. Optical emission of the burning particles was captured using a photomultiplier tube (PMT, Hamamatsu model R3896-03) equipped with a 700-nm interference filter. The pulse durations recorded by the PMT were interpreted as particle burn times. The distribution of the measured particle burn times was correlated with the measured particle size distribution to determine the effect of particle size on its burn time. In addition, the time-resolved spectra were captured using a 32-channel multianode PMT, Hamamatsu model H7260, coupled with a spectrometer covering the wavelength range of 430-641 nm. The spectra were used to evaluate the temperature histories of the burning thermite particles.

Ignition of the prepared thermite was measured using an electrically heated filament. The details of the setup are described elsewhere (Shoshin et al. 2006b; Ward et al. 2006b). The sample was mixed with hexane and coated as a slurry on a nickel-chromium wire. After hexane dried, the wire was heated electrically by a DC current. Heating rates varied from 1500 to 30000 K/s. The wire temperature was measured in real time by an infrared pyrometer. The ignition of the powder coating was captured using a high-speed camera (MotionPro500 by Redlake) operated at 500 fps. The filament temperature at the ignition instant was treated as the powder ignition temperature.

5.4 Results

5.4.1 Binary boron-iodine materials

Preliminary TG experiments addressed the effect of milling time on iodine stabilization in boron. In addition, a possible interaction between B_2O_3 and iodine in the composite material was addressed replacing boron with boron oxide as a starting component. The results are shown in Figure 5.1. The boron-iodine samples were milled for 2, 4, and 6 hours; the sample with B_2O_3 as a starting material was milled for 4 hours.

For the 2-hour milled sample, C-$B_{60}I_{40}$-2 (see Table 5.1 for the sample details), the initial low-temperature mass loss is very significant. Thus, most of iodine is not stabilized and evaporates immediately when the heating starts, and the material is exposed to an argon flow. As the heating continues, a low-temperature mass loss starts at about 323 K (50 °C). About 8-9% of the sample mass is then lost before the sample is heated to 473 K (200 °C). This likely represents release of unattached or weakly bound iodine. The presence of such unattached iodine, and its release at low temperatures, were observed earlier for other metal-iodine composites prepared mechanochemically (Abraham et al. 2015; Aly et al. 2014; Zhang, Schoenitz, and Dreizin 2010a). After a short plateau, the mass of the sample starts to decrease again at about 673 K (400 °C). This high-temperature mass loss represents release of iodine that must be chemically bound to boron; for the 2-hour milled sample it includes about 15% of the sample mass, or slightly more than one third of the initial mass of iodine. The nature of this bond remains to be understood. Raman spectroscopy patterns for boron were identical to those of boron-iodine composites, while no patterns typical of elemental iodine were detected for the composite materials. Additional studies of the nature of this and other similar metal-iodine bonds obtained in the mechanochemically prepared materials are of interest and planned for the future work.

For the sample with the same nominal composition, but milled for 4 hours, C-$B_{60}I_{40}$-4, the initial mass loss step disappears and the mass loss step beginning at about 323 K (50 °C, the first mass loss step for this material) is reduced dramatically to about 2 %. The second mass loss step begins at nearly the same temperature, 673 K (400 °C), as for the 2-hour milled sample. Its magnitude is increased to almost 25 % of the sample mass. It is followed by the third, high-temperature mass loss step beginning at about 773 K (500

°C) and releasing iodine at a lower rate upon heating. Milling for 4 hours stabilized iodine better, and it was therefore used in subsequent experiments.

The TG traces for C-$B_{60}I_{40}$-6 and C-$B_{50}I_{50}$-6 samples milled for 6 hours are shown by dashed lines. The initial mass loss for these materials was partially offset by a slow oxidation. The oxidation could involve trace oxygen present in the furnace; qualitatively, it indicates that the samples contained very fine particles with a highly developed reactive interface area. The main, second mass loss step occurred at nearly the same temperature and at about the same rate as for C-$B_{60}I_{40}$-4. The third mass loss step is substantially weaker than for the 4-hour milled material. For C-$B_{60}I_{40}$-6, the overall mass loss was smaller in magnitude than for C-$B_{60}I_{40}$-4, suggesting that milling longer than 4 hours results in a lower concentration of iodine stabilized in the material. For C-$B_{50}I_{50}$-6, the overall mass loss was nearly the same as for C-$B_{60}I_{40}$-4, suggesting that a smaller fraction of iodine was retained when more iodine was used in the initial mixture. Therefore, an increase in the initial iodine concentration above 40 wt % did not lead to further increase in the concentration of iodine stabilized in the composite.

Results shown in Figure 5.1 also suggest that B_2O_3 does not stabilize iodine as well as elemental boron. The first, low-temperature mass loss step for the B2O3$_{60}I_{40}$-4 sample is very strong, nearly 15 %. At higher temperatures, a two-step mass loss is observed, qualitatively similar to that occurring for C-$B_{60}I_{40}$-4, but releasing less iodine.

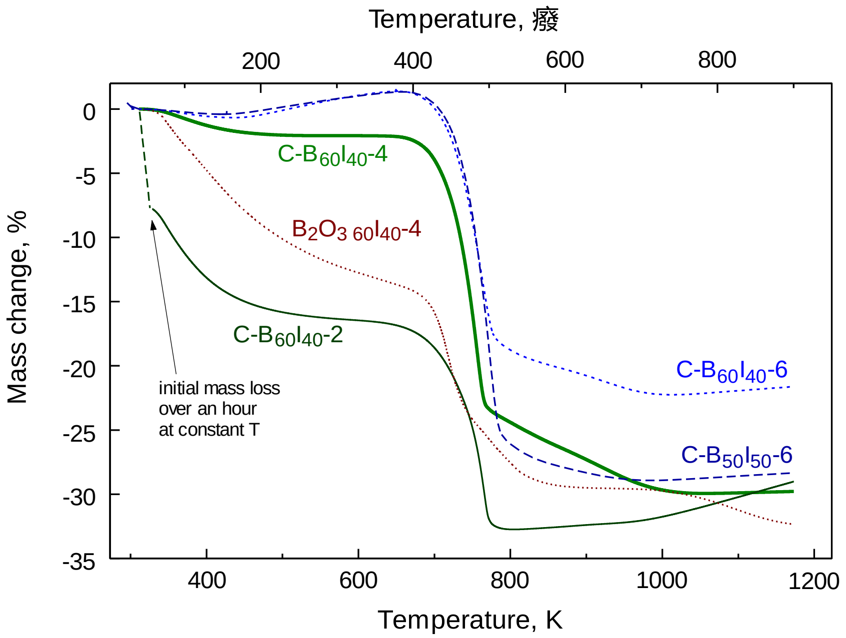

Figure 5.1 TG traces for boron-iodine and boron oxide-iodine composites prepared using different milling times. Samples are heated in argon at 5 K/min.

TG traces for different boron-iodine composite materials milled for 4 hours (cf. Table 5.1) heated in argon are shown in Figure 5.2. For these composites, the mass loss occurs in three main steps: the first starting around 323 K (50 °C), the second beginning around 673 K (400 °C), and the third, starting at about 773 K (500 °C). The first step is relatively small, ca. 2±0.5 % of the sample mass, and is similar for all samples, including that prepared using the surface-functionalized boron [23], for which the amount of the $B(OH)_3$ is markedly reduced. Therefore, for all samples this initial mass loss step is attributed to release of iodine, which is not chemically bound to boron. The main iodine release occurs at substantially higher temperatures, suggesting that iodine is well-stabilized in the boron matrix. The second mass loss step is the fastest; it is markedly different for the samples prepared with different starting iodine concentrations. For C-$B_{70}I_{30}$-4 prepared with 30% of iodine, the second step represents the loss of about 10% of the sample mass.

For samples C-$B_{60}I_{40}$-4 and F-$B_{60}I_{40}$-4, containing initially 40% of iodine and prepared using commercial and functionalized boron powders, respectively, the mass loss during the second step is between 20 and 25% of the sample mass. For the sample using the surface-functionalized boron, the second step begins at a slightly lower temperature and is somewhat smaller than that observed for the material prepared using the as-received commercial boron. For all materials, the third step immediately follows the second one; the mass is reduced more slowly, and the total mass loss amounts to about 7±1 % of the sample mass for all materials.

Based on the total mass loss observed, it is concluded that up to 20.3% of iodine was retained in the sample prepared with 30% of iodine initially. This includes about 2% of unbound iodine released at low temperatures. Samples prepared with 40% of iodine retained nearly 30% of it, including 2 – 2.5 % of unbound iodine. Thus, nearly 28% of iodine was stabilized in the boron matrix, representing the highest concentration of iodine included in a binary metal-iodine composite prepared to date.

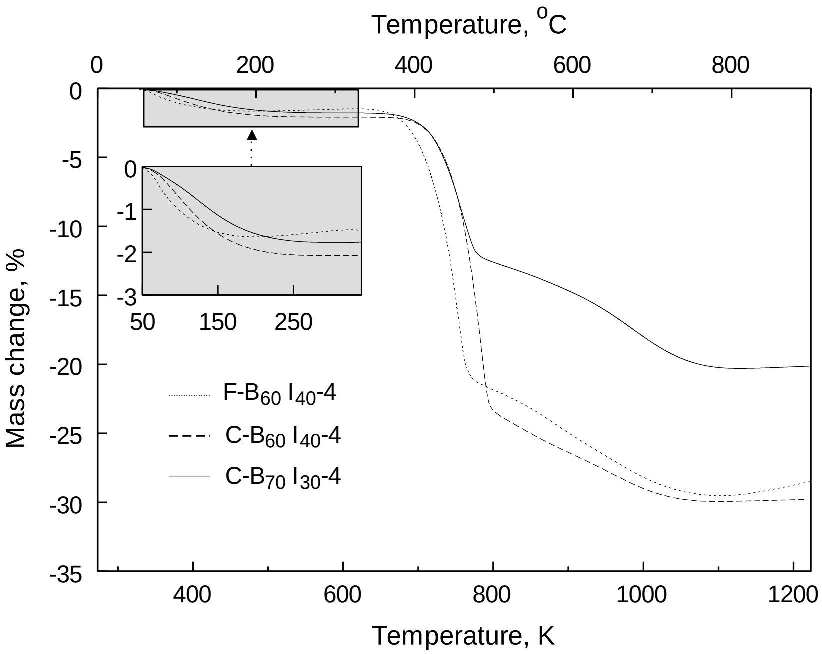

Figure 5.2 TG traces of binary boron-iodine samples milled for 4 hours heated in argon at 5 K/min.

5.4.2 Composite thermites

Surface functionalization did not result in a tangible difference in the observed stability or iodine release by the produced boron-iodine composite materials. Therefore, the binary composite prepared using as-received commercial boron, C-$B_{60}I_{40}$-4, was used as a starting material to prepare thermite with $Ca(IO_3)_2$ as an oxidizer. An SEM image showing the thermite is presented in Figure 5.3. $Ca(IO_3)_2$ appears as a bright coating on darker, boron-rich particles. The primary particles have dimensions varied from submicron to 3 – 5 µm. The particles are heavily agglomerated, although the agglomerates appear to be relatively porous. Shown is a relatively large agglomerate. Most particles have similar agglomerated structures, although the sizes of agglomerates vary significantly.

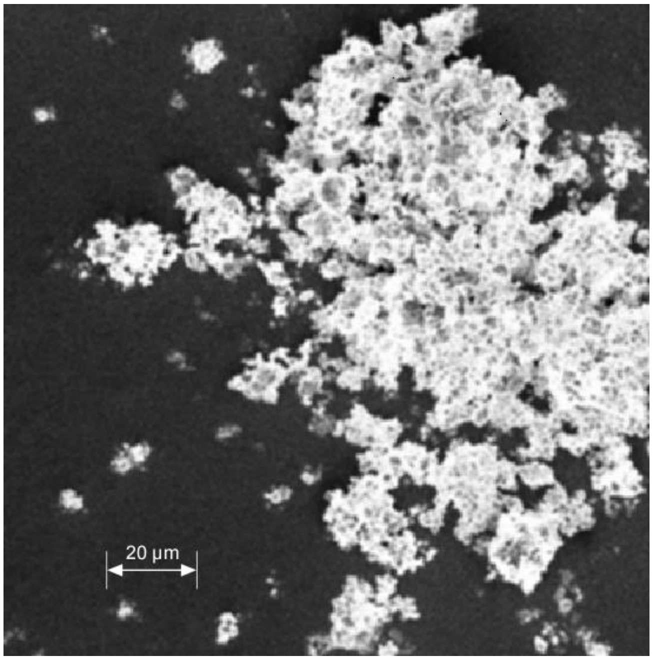

Figure 5.3 SEM image of the prepared thermite with C-$B_{60}I_{40}$-4 as a fuel and $Ca(IO_3)_2$ as an oxidizer. The image is obtained using backscattered electrons. Particles rich in boron, which is a lighter element, appear darker.

Multiple SEM images were collected and processed using ImageJ to identify particles and measure their sizes accounting for the fractal dimension of the agglomerates (Chintersingh et al. 2016b). Agglomerates were treated as single particles, assuming that they coalesce and burn without de-agglomerating while being injected into the flame. The obtained particle size distribution is shown in Figure 5.4. It is based on processing a total of 50 images containing 1976 particles. The fractal dimension was 1.86 which is similar to those of boron, 1.8 (Chintersingh et al. 2016b) and $B{\cdot}Ca(IO_3)_2$, 1.85 (Wang et al. 2017a).

This size distribution was correlated with the measured distribution of the particle burn times (see below).

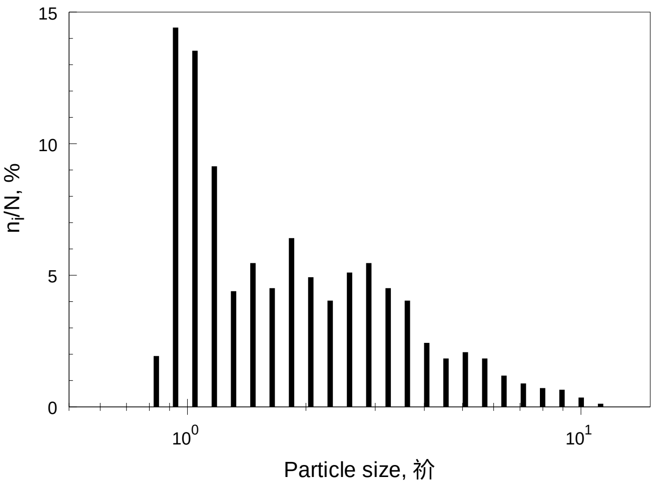

Figure 5.4 Particle size distribution for the thermite containing mechanically milled C-B$_{60}$I$_{40}$-4 and Ca(IO$_3$)$_2$ powders.

5.4.3 Combustion of thermite particles

A typical sequence of optical emission pulses produced by the ignited particles is shown in Figure 5.5. Peaks produced by burning particles are relatively well distinguished from the background emission of the air-acetylene flame. Most peaks are well separated from one another, representing individual burning particles. One such peak is shown in the inset in Figure 5.5. The duration was measured for such peaks and interpreted as the burn time. Some peaks overlapped, as for example the sequence starting at about 100 ms in Figure 5.5. Such overlapped peaks were discounted from further analysis.

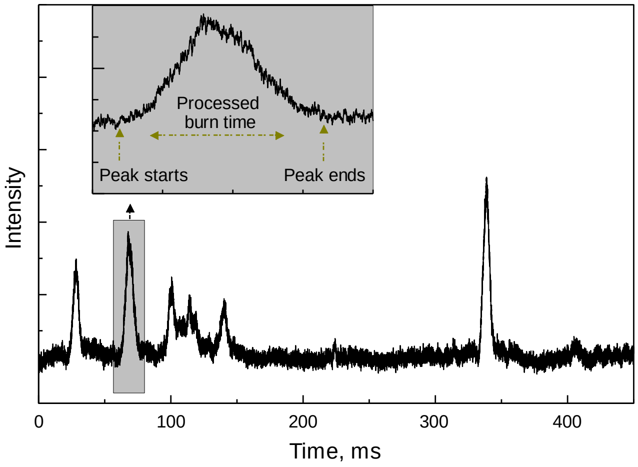

Figure 5.5 Sequence of emission peaks produced by burning particles and measured using a PMT equipped with a 700-nm interference filter.

A distribution of the peak durations is shown in Figure 5.6. A total of 320 individual particle peaks were included in this analysis. For most particles, the burn times vary in the 5-20 ms range. The average burn time is 11.9 ms.

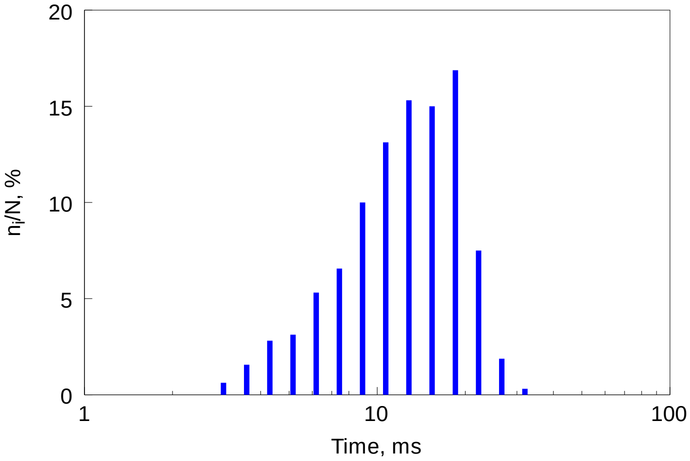

Figure 5.6 Distribution of pulse durations for burning C-$B_{60}I_{40}$-4·$Ca(IO_3)_2$ particles injected in an air-acetylene flame.

The distribution of the burn times was correlated with the particle size distribution obtained from SEM images (Figure 5.4). The results are shown in Figure 5.7. Due to the different shapes of size (Figure 5.4) and burn time (Figure 5.6) distributions, the correlations shown in Figure 5.7 are not straight lines. A change in the slope is observed for particles of about 1 µm. This could be explained by a real change in the combustion mechanisms for particles of different sizes. Conversely, this could simply indicate a bias in the measurement of either particle size distribution or burn time. Although it remains unclear why there is a distinct change in slope in the shown correlation, the range of burn times corresponding to the experimental range of particle sizes is well identified. For reference, similar results are also shown for as-received commercial boron particles (Chintersingh et al. 2016b) and for the composite $B \cdot Ca(IO_3)_2$ powder described elsewhere (Wang et al. 2017a). The burn times are indistinguishable among different materials for particles greater than ca. 5 µm. For finer particles, pure boron powder has shortest burn times. The longest burn times are observed for the binary $B \cdot Ca(IO_3)_2$ composite. The material prepared in this effort and containing C-$B_{60}I_{40}$-4 as a fuel and a similar thermite using as received commercial boron as a fuel have the same burn time vs. particle size trends for particles greater than 1 µm. For finer particles, the burn times for the material using C-$B_{60}I_{40}$-4 as a fuel become shorter because of the mentioned above change in slope of the obtained correlation. This results in a greater overall effect of particle size on their burn time, accounting for the entire range of burning particle sizes for C-$B_{60}I_{40}$-4$\cdot Ca(IO_3)_2$ thermite.

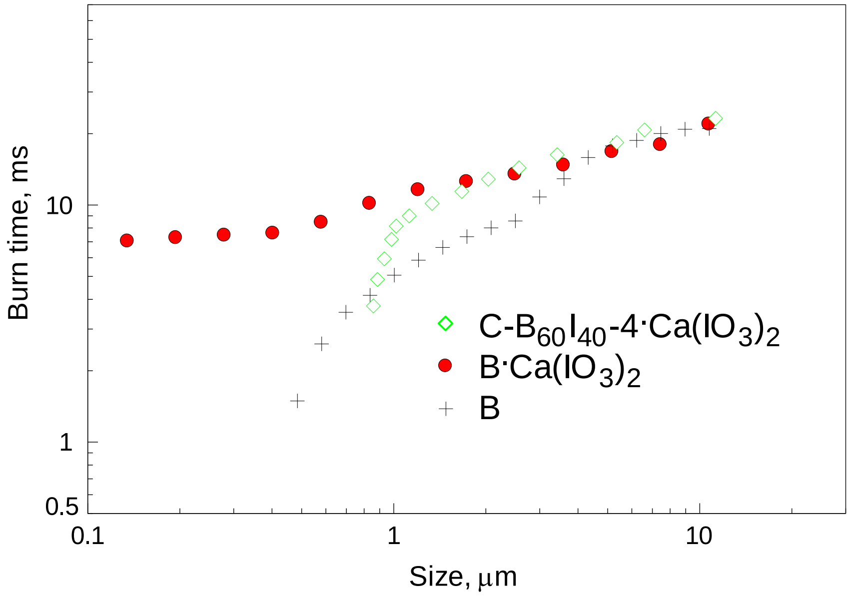

Figure 5.7 Burn time vs. size for thermites of C-$B_{60}I_{40}$-4·$Ca(IO_3)_2$ and B·$Ca(IO_3)_2$ (Wang et al. 2017a) and for elemental boron (Chintersingh et al. 2016b).

An example of an emission pulse produced by a burning thermite particle recorded by the 32-channel PMT equipped with a spectrometer is shown in Figure 5.8. Each solid line is a time-resolved emission trace recorded at a particular wavelength. The amplitude of the emission generally becomes stronger at longer wavelengths. The measurement was used to estimate the combustion temperature, assuming that the particle is a gray-body emitter, so that the spectrum could be described by Planck's equation, where temperature served as an adjustable parameter (Monk, Schoenitz, and Dreizin 2016a). The temperature obtained as a function of time is also shown in Figure 5.8 as a dashed blue line. The apparent increases in the temperature observed when the emission intensities become weak both at the beginning and end of the pulse suggest an erroneous measurement due to the low emission signal. Thus, the time-dependent temperature measurement for individual particles could not be obtained. However, around the maximum pulse amplitude, the temperature is expected to be measured reasonably well. It is close to 2050 K, representing the maximum temperature of a burning particle. This result is similar to that reported for the B·Ca(IO_3)$_2$ thermite (Wang et al. 2017a).

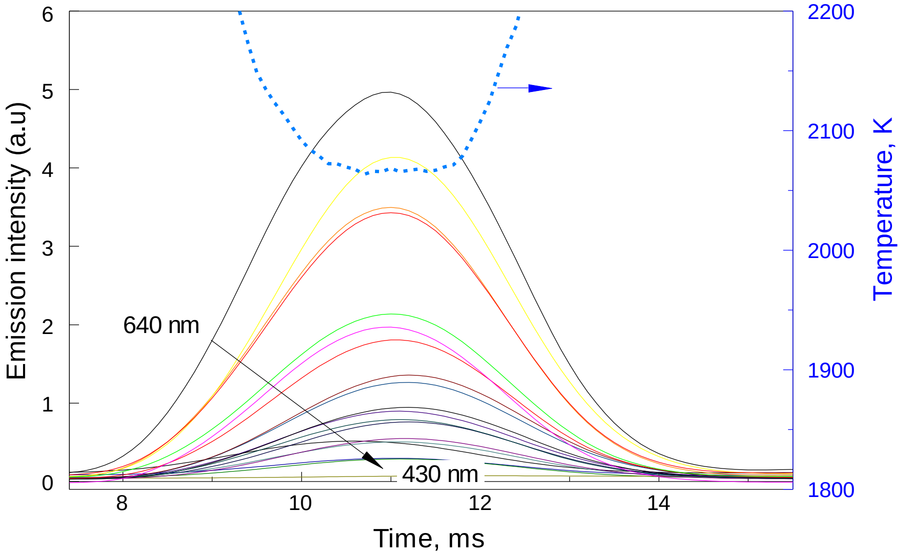

Figure 5.8 Emission traces produced by a burning thermite particle recorded by the 32-channel PMT equipped with a spectrometer. Each trace represents emission at a selected wavelength between 430 and 640 nm. A temperature trace is also shown obtained by fitting the emission spectrum to Planck's formula.

Condensed combustion products were collected on a silicon wafer, which was swiped across the flame. The products were collected approximately 5 cm above the burner nozzle. An SEM image of a typical product particle is shown in Figure 5.9. Collected particles were of nearly perfect spherical shape. They have a color suggesting that there is no detectable separation between different product phases. Energy-dispersive spectroscopy (EDS) showed the presence of calcium and oxygen. Boron peak overlaps with that of oxygen and thus is difficult to detect, although the presence of boron is assumed. The sizes of the product particles were similar to or smaller than that shown in Figure 5.9. Thus, most products particles were finer than the original thermite agglomerates.

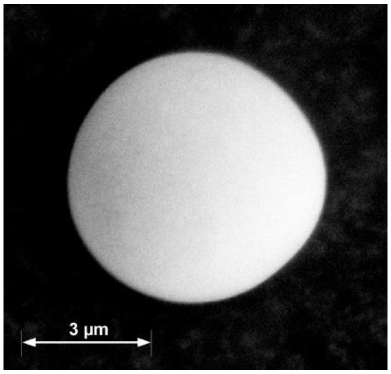

Figure 5.9 SEM image of a combustion product particle of C-$B_{60}I_{40}$-4·$Ca(IO_3)_2$ thermite burned in an air-acetylene flame.

5.4.4 Ignition of thermite particles

Ignition temperatures obtained from the heated filament experiments are shown in Figure 5.10; the measurements for C-$B_{60}I_{40}$-4·$Ca(IO_3)_2$ prepared in this study are compared to the earlier measurements for B·$Ca(IO_3)_2$ (Wang et al. 2017a). Each point represents a single run. The powder coating thickness could not be maintained constant between different runs, which likely explains the scatter in the experimental data. The average ignition temperature for C-$B_{60}I_{40}$-4·$Ca(IO_3)_2$ is 574±29 K, which is noticeably lower than 645±28 K determined for B·$Ca(IO_3)_2$ composite.

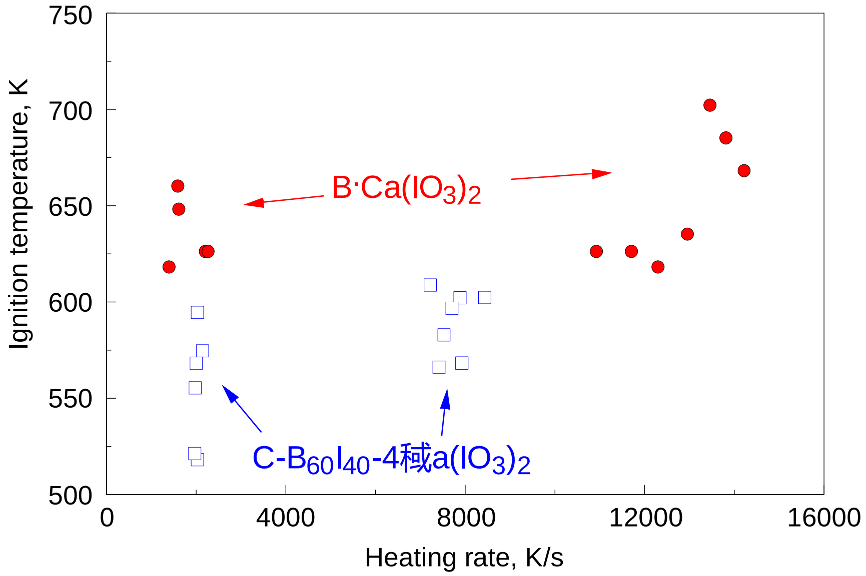

Figure 5.10 Ignition temperatures for C-$B_{60}I_{40}$-4·Ca(IO_3)$_2$ prepared here and for B·Ca(IO_3)$_2$ (Wang et al. 2017a).

5.5 Discussion

The iodine loss from the binary B·I_2 composites prepared here occurs in three distinct steps (cf. Figs. 5.1, 5.2). The first, low-temperature mass loss step representing release of unattached iodine was observed for all metal-iodine composite materials prepared mechanochemically (Zhang, Schoenitz, and Dreizin 2010a; Abraham et al. 2015; Abraham et al. 2014). This mass loss is commonly reduced when milling times increase and iodine is included in the metal matrix. Indeed, the mass loss decreased markedly when the milling time increased from 2 to 4 hours. An additional effect of slight mass gain observed here for the samples milled for 6 hours suggests that longer milling yields particles with a greater surface area, capable of oxidation with even trace amounts of oxygen. Such a low-temperature reactivity is undesirable for a practically useful material.

The low-temperature mass loss representing release of unbound iodine occurs around the same temperature range as dehydration of the as-received commercial boron (Liu et al. 2017; Chintersingh, Schoenitz, and Dreizin 2016). However, the low-temperature mass loss is smaller for the boron-iodine composites than for the dehydration of the commercial boron surface alone, even accounting for the amount of boron in the composite. This dehydration was also dramatically different for the as-received and surface-functionalized boron samples (Chintersingh, Schoenitz, and Dreizin 2016; Liu et al. 2017). However, no difference in the low-temperature mass loss step was observed here between C-$B_{60}I_{40}$-4 and F-$B_{60}I_{40}$-4 composites (Figure 5.2), prepared using as received and surface-functionalized boron, respectively. Thus, dehydration is assumed not to affect the present measurements. The results could imply that milling boron with iodine removes or replaces the hydrated boron oxide from the boron particle surfaces, thereby reducing the associated initial mass loss step, which becomes indistinguishable for boron-iodine composites prepared with both as received and surface functionalized boron powders.

The second mass loss step starting from 673 K (400 °C) is similar to the second iodine loss step observed earlier for the ternary $Al\cdot B\cdot I_2$ materials (Abraham et al. 2015). It is the most well defined and rapid among the three observed mass loss steps. Because it occurs in both ternary and binary $B\cdot I_2$ composites, it is likely to represent decomposition of a metastable boron-iodine compound. Interestingly, this mass loss step is also observed for $B_2O_3\cdot I_2$ composite, although it is less pronounced in the latter case. Thus, boron and iodine are bonded in different boron-containing compounds mechanochemically processed with iodine. This bonding stabilizes iodine in the solid at temperatures substantially higher than 483 K (210°C), the boiling point of the most stable known boron-iodine compound,

BI_3 (Samsonov et al. 2012). The third, final mass loss occurs over a rather broad temperature range; it must represent release of iodine most strongly bonded to boron.

Milling binary $B\cdot I_2$ composite with $Ca(IO_3)_2$ yields a material with micron- and submicron $B\cdot I_2$ particles embedded in a loosely agglomerated $Ca(IO_3)_2$ matrix (Figure 5.3). Considering relative stability of $Ca(IO_3)_2$, such a structure could further help retain iodine in the composite material. There is a significant number of agglomerated particles with dimensions exceeding 3 μm (Figure 5.4) and fewer superfine particles than was observed for mechanochemically prepared thermites using commercial boron with calcium iodate (Wang et al. 2017a). Respectively, the average, number-based particle size of the C-$B_{60}I_{40}$-4 thermite prepared here is 2.2 μm, compared to 1.6 μm reported in Ref. (Wang et al. 2017a) for a similar $B\cdot Ca(IO_3)_2$ material.

The relatively featureless shapes of emission pulses produced by the present thermite material (Figure 5.5) are qualitatively similar to those observed for $B\cdot Ca(IO_3)_2$ thermites described earlier (Wang et al. 2017a). The average flame temperatures are the same for both materials (Figure 5.7). The adiabatic flame temperatures calculated using NASA CEA code (McBride and Gordon 1996) for the compositions including boron, calcium iodate, and iodine as fuels burning in an air-acetylene flame vary very little, from 2442 to 2437 K with the assumed iodine concentration in the $B\cdot I_2$ composite varied from 10 to 40%. This calculated temperature is somewhat higher than the experimental value of ca. 2050 K, which is readily explained by heat losses from the particle flames to the surroundings.

The burn times for coarser agglomerates are identical for both composites using $Ca(IO_3)_2$ as an oxidizer with boron or boron-iodine composite as a fuel (cf. Figure 5.7).

There is an apparent difference in the burn time for finer particles, which represent the least agglomerated composites. The reliability of the present trends shown in Figure 5.7 based on correlations between the measured particle size and burn time distributions may be inadequate to conclude that this difference is, indeed significant. However, if it is, it might suggest that iodine release from $B \cdot I_2$ composite particles helps break up fine agglomerates accelerating their combustion. This effect may be less noticeable in coarser particles, where break up of $Ca(IO_3)_2$-held agglomerates is more difficult. The same effect of iodine release from $B \cdot I_2$ composite particles can also explain a lower ignition temperature, observed for $B \cdot I_2 \cdot Ca(IO_3)_2$ compared to that of $B \cdot Ca(IO_3)_2$ composite material (Figure 5.10). Release of iodine generates a fresh surface in the cracks and deagglomerates coarser particles; both effects assist ignition of the heated powder.

Finally, the morphology of the collected condensed combustion products (Figure 5.8) suggests that large agglomerates break up and burn primarily in the vapor phase. Qualitatively, this is in agreement with the observation of the jets comprising fine particulates and gaseous flame generated by combustion of the consolidated $B \cdot Ca(IO_3)_2$ composite in Ref. (Wang et al. 2017a). The vapor-phase combustion is attractive for many applications, where combustion products are expected to expand and generate a pressure pulse.

5.6 Conclusions

Mechanochemical processing of boron and iodine yields a material with up to 30 wt % of iodine stabilized in the solid composite at temperatures below 673 K (400 °C). There is always a small (ca. 2 – 2.5 %) amount of iodine released at lower temperatures, which is expected to be lost during handling and storage of such composite materials. The main iodine release occurs when the material is heated to about 673 K (400 °C); it likely represents breakdown of a metastable boron-iodine compound. Release of iodine continues when the sample is heated further, up to about 1023 K (750 °C).

The milling conditions are identified here for preparation of boron-iodine composites in a laboratory shaker mill: milling time of 4 hours, ball to powder mass ratio of 10. Prepared binary composites can be used as a fuel in mechanochemically prepared thermites with $Ca(IO_3)_2$ as an oxidizer. Produced thermites comprise loosely agglomerated micron-sized particles of $Ca(IO_3)_2$ with embedded finer particles of $B{\cdot}I_2$ composite. The material contains 57.6 wt % if iodine. The prepared composites ignite when heated to ca. 574 K, almost 100 K lower than the ignition temperature of respective binary $B{\cdot}Ca(IO_3)_2$ thermites. Qualitatively, binary $B{\cdot}Ca(IO_3)_2$ thermites described earlier (Wang et al. 2017a) burn similarly to their analogs prepared here, in which boron is replaced with a boron-iodine composite material. The flame temperature is close to 2050 K, the combustion is dominated by the vapor-phase reaction, generating fine, spherical oxide particles including both boron and calcium oxides mixed homogeneously.

CHAPTER 6

PREPARATION, IGNITION, AND COMBUSTION OF MAGNESIUM-CALCIUM IODATE REACTIVE NANO-COMPOSITE POWDERS

6.1 Abstract

Arrested reactive milling is used to prepare a composite thermite powder combining magnesium metal with calcium iodate, $Ca(IO_3)_2$. Upon ignition, this material generates iodine, a biocidal species capable of effective inactivation of aerosolized microorganisms. The prepared material is metal-rich with a fuel /oxidizer ratio of 4. It contains 29 wt% of iodine. The material is a micron-sized powder with each particle having a magnesium matrix and nanosized inclusions of calcium oxide. A similar composite with a stoichiometric ratio of fuel to oxidizer is found to be unstable in air. The prepared metal-rich composite was characterized using thermo-gravimetric analysis, ignition experiments using an electrically heated filament, and particle combustion experiments in both air and the combustion products of an air-acetylene flame. The powder was found to readily release iodine upon heating. It ignited in two distinct stages, with the first, low-temperature ignition prompted by iodine release, and second stage ignition caused by reaction of any remaining magnesium. In an air-acetylene flame, the powder particles burned in two distinct stages, unlike other similar materials. In air, only one combustion stage was distinguished. Combustion of the prepared powders in air occurs much faster than in the products of the air-acetylene flame; burn rates of the prepared composite powders in both air and products of air-acetylene flame are slightly lower than those of pure magnesium burning in the same environments.

6.2 Introduction

Proliferation of chemical and biological weapons and related weapon stockpiles (Eneh 2012) prompted recent interest in developing specialized materials capable of defeating aerosolized chemical and biological agents (Clark and Pantoya 2010; Farley and Pantoya 2010; Feng et al. 2013; He, Hooper, and Shreeve 2016; Henderson et al. 2015; Smith, McCollum, and Pantoya 2016; Wu et al. 2017). Biological agent-defeat weapons often rely on halogens such as iodine (He, Zhang, and Shreeve 2013a; Clark and Pantoya 2010; Farley and Pantoya 2010; Feng et al. 2013; Grinshpun et al. 2012; He, Hooper, and Shreeve 2016; Henderson et al. 2015; Hobosyan, Kazansky, and Martirosyan 2012; Johnson and Higa 2013; Smith, McCollum, and Pantoya 2016; Wang et al. 2015; Wu et al. 2017; Zhang et al. 2012) to passivate spores. Halogens are volatile and may therefore be difficult to work with. Thus, the challenges in developing halogen-containing reactive materials are to enable high concentration of halogen released upon ignition, while achieving a stable and easy to handle material, which can be incorporated in an energetic formulation and stored safely before use. In addition, the material must be easily ignited and combustible with a high burn rate and an energy release comparable to that of common metal additives to energetic formulations, e.g., aluminum, magnesium, etc.

Significant previous efforts focused on preparing materials with a metal matrix containing elemental iodine stabilized mechanochemically (Grinshpun et al. 2012; Grinshpun et al. 2017; Zhang et al. 2012; Zhang, Schoenitz, and Dreizin 2010a; Abraham et al. 2014; Aly et al. 2014; Liu, Schoenitz, and Dreizin 2017; Wang et al. 2016; Zhang, Schoenitz, and Dreizin 2010b). It was found that up to 20 wt % of iodine can be retained in a metal-matrix composite. Higher iodine concentrations may be desired for some applications, and thus other components carrying iodine need to be explored. For example, recently it was shown that calcium iodate can serve as both an effective oxidizer and iodine carrier in such materials (Wang et al. 2017b; Oxley et al. 2017).

In recent experiments, where the biocidal effect produced by combustion products of reactive materials could be assessed for short, sub-second bioaerosol exposure times, it was observed that for very short exposures, combustion products of magnesium are very effective (Nakpan et al. 2018). In addition, magnesium ignites readily and thus can serve as a useful metal additive for energetic formulations, for which the rate of reaction and biocidal efficiency are of primary importance. Therefore, this work is focused on preparation and characterization of ignition and combustion for composite magnesium-calcium iodate powders. Their biocidal effectiveness will be tested and discussed separately.

6.3 Preparation of $Mg{\cdot}Ca(IO_3)_2$ Nanocomposite Thermite Samples

99.8% pure, -325 mesh Mg powder by Alfa Aesar and 98% pure $Ca(IO_3)_2$ by Sigma Aldrich were used as starting materials for preparation of the thermite powders. Three thermite samples were prepared by arrested reactive milling (Dreizin and Schoenitz 2009). The milling conditions are shown in Table 6.1. The sample ID shows its approximate molar composition followed by SM or PM for shaker and planetary mills, respectively. $5Mg{\cdot}Ca(IO_3)_2$-SM and $20Mg{\cdot}Ca(IO_3)_2$-SM had respectively stoichiometric and fuel rich compositions with equivalence ratios of 1 and 4. $5Mg{\cdot}Ca(IO_3)_2$-SM was prepared using 0.7 g of Mg and 2.3 g of $Ca(IO_3)_2$; $20Mg{\cdot}Ca(IO_3)_2$-SM was prepared using 1.65 g of Mg and 1.35 g of $Ca(IO_3)_2$. Starting materials were added into a 50 mL flat-end steel milling vials with 30 g of 9.5 mm diameter carbon steel balls. 2 mL of hexane was added as process control agent (PCA). Milling was conducted in a shaker mill (SPEX Certiprep, 8000 series) for one hour with room-temperature air-jet cooling for the milling vials. The stoichiometric sample was found to be pyrophoric in air; therefore, only the fuel-rich composition was explored further to prepare larger scale samples.

A larger, 30-g batch of the fuel rich thermite, sample $20Mg\cdot Ca(IO_3)_2$-PM, was prepared using 16.5 g of Mg and 13.5 g of $Ca(IO_3)_2$ milled using Retsch PM-400 MA planetary mill. The material was milled in a custom-made steel vial with 18-mm thick walls and lid attached by seven 7.9-mm diameter bolts (thread size 5/16”), capable of withstand high-pressure that might develop in case of an accidental ignition of the material during milling. The powder was loaded together with 300 g of 9.5 mm diameter carbon steel balls and 20 mL hexane serving as PCA. The milling time was 1 hour. The milling vials were sealed in argon before milling. After milling, the materials were recovered and stored in argon. Preliminary assessment of reactivity of the prepared samples was made recovering approximately 0.1 g of powder and burning it in open air. The powder was placed on a filter paper, and the paper was ignited using a gas lighter. Reactive powders burned with a bright flash.

As noted above, $5Mg\cdot Ca(IO_3)_2$-SM self-ignited while being handled in air. The combustion was slow, suggesting also that the sample might have rapidly aged while being exposed to air even prior to ignition. Stoic metric sample is not stable, because excessive metal-oxidizer fresh surface was created during milling. $20Mg\cdot Ca(IO_3)_2$-SM was stable in room air; it burned rapidly when ignited on a filter paper, indicating a good reactivity.

$20Mg\cdot Ca(IO_3)_2$-PM behaved similarly to $20Mg\cdot Ca(IO_3)_2$-SM in preliminary reactivity assessments. Thus, all further experiments were performed with $20Mg\cdot Ca(IO_3)_2$-PM.

Table 6.1 Prepared Reactive Composite Samples

Sample ID	Eq. Ratio	Powder mass, g	PCA: Hexane, mL	Milling equipment	Preliminary observations (igniting powder on a filter paper)
$5Mg\cdot Ca(IO_3)_2$-SM	1	3	2	Shaker mill	Pyrophoric at 40 ºC, low reactivity
$20Mg\cdot Ca(IO_3)_2$-SM	4	3	2	Shaker mill	Stable at low temperature high reactivity
$20Mg\cdot Ca(IO_3)_2$-PM	4	30	20	Planetary mill	Stable at low temperature high reactivity

6.4 Experimental Techniques

Stability of the prepared material and reactions leading to its ignition were characterized using thermo-gravimetric (TG) analysis using a Netzsch STA409PC/PG. Typically, the powder load was 15 mg in each run. The experiments were performed in pure Ar (flowrate 50 mL/min) and mixed Ar/O_2 flows (flowrates of 80 and 20 mL/min for Ar and O_2, respectively). To avoid ignition, the temperature was increased only up to 723 K (450 °C) at 2 K/min. Residues quenched at different temperatures were collected for further x-ray diffraction analysis.

Ignition of the prepared materials was characterized using an electrically heated filament setup (Ward et al. 2006a). The powder was mixed with hexane and coated on a

0.51-mm diameter nickel-chromium wire. After hexane dried out, the wire was heated by a DC current. Different voltages were applied on the wire to get different heating rates from 800 to 35,000 K/s. Seven runs were conducted for each heating rate. The temperature of the wire was monitored as a function of time by a custom-built pyrometer using a germanium switchable gain detector (PDA30B2 by Thorlabs). A lens was focused on an uncoated portion of the wire; it was placed at the inlet of a fiber optics cable, transmitting the wire emission to the detector. The output of the pyrometer was calibrated using a black body emission source (BB-4A by Omega Engineering). A high-speed camera (MotionPro500 by Redlake) at 500 fps was used to record the ignition event. Additionally, a second photosensor (DET110 by Thorlabs, Inc.) with the field of view including both coated and uncoated portions of the wire was used to record the optical emission produced by the igniting powder. Correlating the temperature trace and the instant the optical emission produced by the igniting powder was detected, the ignition temperature was obtained.

Particle combustion experiments were conducted in two environments: room temperature air and combustion products of an air-acetylene flame. In both experiments, material was loaded into a custom powder feeder and aerosolized by a flow of air or nitrogen. Details of the powder feeder design are available in the literature (Corcoran, Hoffmann, and Dreizin 2013). The powder was fed in the laser beam or in the premixed air-acetylene flame. See Refs. (Corcoran, Hoffmann, and Dreizin 2013; Corcoran et al. 2015; Chintersingh et al. 2016b) for experimental details on particles burning in the products of the air-acetylene flame and Refs. (Chintersingh, Schoenitz, and Dreizin 2018; Wang, Schoenitz, and Dreizin 2017) for details on combustion of laser-ignited particles in air. Briefly, in experiments using laser ignition, the powder was carried by compressed air flow (flowrate 2.3 L/min) and raised vertically, crossing a horizontally directed CO_2 laser beam focused to about 250 µm. The particle velocity was close to 1 m/s (Liu, Schoenitz, and Dreizin 2018a). The laser power was set to 87.5 W to reliably ignite all powder particles crossing the beam. In the experiments involving combustion products of a hydrocarbon flame, a premixed air-acetylene flame was produced. Flow rates of air and acetylene were 4.75 and 0.425 L/min, respectively. The adiabatic flame temperature was predicted to be 2610 K (Wang, Corcoran, and Dreizin 2015; McBride and Gordon 1996); mole fractions of the main flame products CO, CO_2, H_2O, and OH were respectively 0.18, 0.05, 0.07 and 0.004 (with the balance of N_2). Powder was fed along the axis of a cylindrical, premixed air-acetylene flame by a 0.944 L/min nitrogen flow.

In both cases, optical emission pulses produced by burning particles were recorded by R3896-03 Hamamatsu photomultipliers (PMTs) equipped with 700 and 800 nm interference filters. Data were acquired by LabVIEW software by National Instruments. Burning temperatures were obtained from the ratio of light emission signals acquired at two different wavelengths accounting for a calibration of the filtered PMTs using emission from a tungsten filament heated to different temperatures. The pulse durations were treated as burn times and statistical distributions of the burn times were obtained. These distributions were correlated with the measured particle size distributions, to obtain the effect of particle size on burn time (Corcoran et al. 2013b; Wang, Corcoran, and Dreizin 2015).

In order to account for possible size classification and agglomeration of powder particles while passing through the feeder, the particle size distributions were measured for the powder samples passed through the feeder. An SEM stub coated with a conductive, double sided adhesive carbon tape was used to collect powder particles exiting the nozzle at the approximate locations of the laser beam and expected particle ignition when entering the air-acetylene flame. The collected powder samples were imaged by SEM at different magnifications. The powder particle size distribution was then obtained following the method described in Ref. (Chintersingh et al. 2016a).

6.5 Results

An overview and high magnification images of the prepared material taken using a LEO 1530 Field Emission Scanning Electron Microscope (SEM) are shown in Figure 6.1. The images are acquired using backscattered electrons, so that Mg appears darker and $Ca(IO_3)_2$ appears lighter gray. Figure 6.1a shows that particle sizes vary from submicron to tens of microns. All particles appear to consist of well mixed Mg and $Ca(IO_3)_2$. A close-up image in Figure 6.1b shows that nano-sized $Ca(IO_3)_2$ particles coat the surface of Mg. A similar mixing of Mg and nano-sized inclusions of $Ca(IO_3)_2$ is observed in the particle cross-sections. X-ray diffraction analysis of the prepared powder performed using PANalytical Empyrean diffractometer operated at 45 kV and 40 mA using unfiltered Cu Kα radiation (λ = 1.5438 Å) shows the presence of Mg and $Ca(IO_3)_2$ while no reaction products, e.g., MgO were detected.

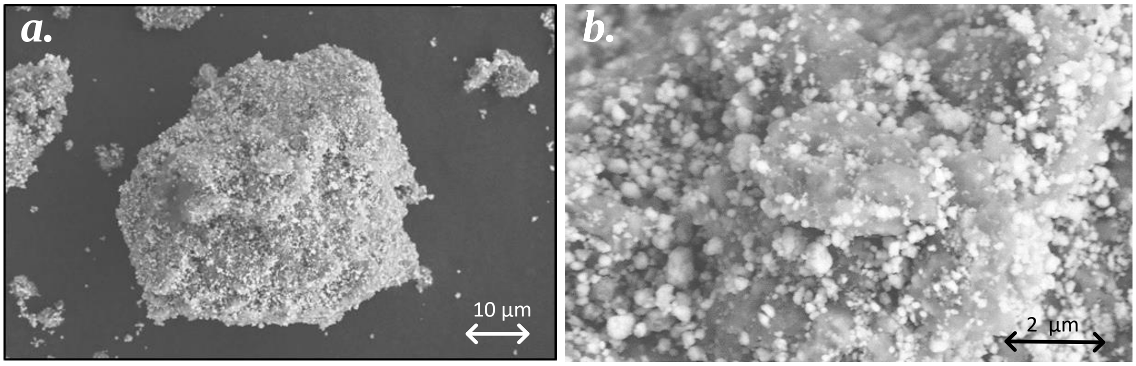

Figure 6.1 SEM images of 20Mg·Ca$(IO_3)_2$–PM powder taken with backscattered electrons: *a*. Particle shapes; *b*. Particle surface. Mg appears grey; Ca$(IO_3)_2$ appears white.

Particle size distribution for the 20Mg·Ca$(IO_3)_2$–PM sample is obtained by analyzing SEM pictures. It is shown in Figure 6.2. The mode of the number based distribution is close to 7.5 µm, and the average size is close to 6 µm. A long tail for finer particle sizes appears to extend beyond ca. 1 µm, the resolution limit achieved in the present measurements. However, it is not expected that very fine, submicron particles unresolved by the present analysis produced optical emission peaks comparable to those produced by much larger particles dominating in the powder. Instead, it is likely that such very small emission peaks are treated as noise during signal processing. Thus, further correlation of the measured emission peak durations of burning particles with their size distribution should be meaningful.

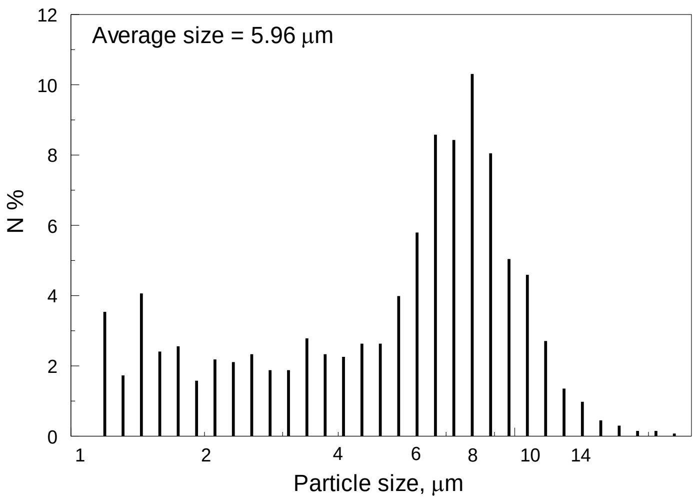

Figure 6.2 Particle size distribution obtained from SEM images for 20Mg·Ca(IO_3)$_2$–PM powder fed through the powder feeder.

TG results for experiments in both oxidizing and inert environments are shown in Figure 6.3. In both experiments, the samples start to lose mass at low temperatures. In argon, the mass loss was continuous over the entire temperature range. The initially slow mass loss rate lasted up to about 190 °C and a mass loss of about 1.6 %. The mass loss rate increased between about 190 °C and 390 °C up to a total mass loss of about 4 %. At that temperature, the mass loss rate increased further and remained high until the end of the experiment. The last observed step of the mass loss amounted to a total of ca. 11%. The total mass loss over the entire temperature range was close to 17.8%, which is approximately 60% of the total iodine content.

The stepwise nature of the mass loss was more prominent in the experiments in oxygen. First, in the temperature range of 50 - 150 °C, the material lost 2.3 % of its total mass. The sample almost did not lose any mass between 150 and 250 °C. The mass loss accelerated notably above 250 °C and continued to about 315 °C, resulting in a total of 3.1 % mass loss in this relatively narrow temperature range. Upon further heating, the sample mass increased by ca. 0.9 wt% while the temperature reached 385 °C. At still higher temperatures, the mass loss accelerated again, similar to the experiment in Ar. The mass loss during this last observed step was 6.5 %.

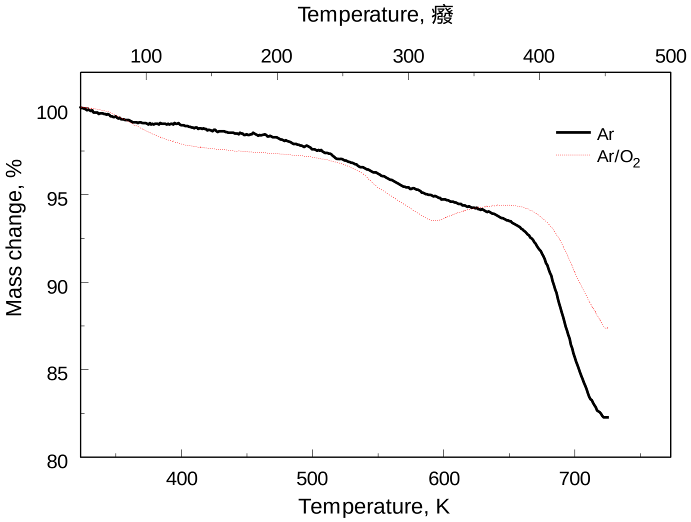

Figure 6.3 TG traces of $20Mg{\cdot}Ca(IO_3)_2$ heated to 450 °C at 2 °C/min in pure argon and argon oxygen gas flows.

To better understand the processes resulting in the detected mass changes, several samples were heated to and quenched from intermediate temperatures and examined using XRD. Results are shown in Figure 6.4. For the sample heated in Ar (Figure 6.4a), shown are XRD patterns for as-milled powder, powder heated to 300 °C (quenched before the last, fastest weight loss step), and heated to the final temperature of 450 °C. In the as-milled powder, the strongest peaks observed in the pattern are assigned to Mg and $Ca(IO_3)_2$. In the sample heated to 300 °C, peaks of $Ca(IO_3)_2$ become slightly weaker while a pattern indicative of formation of MgO appears. The MgO pattern becomes strong at 450 °C, while the pattern of $Ca(IO_3)_2$ is no longer distinguished. Peaks of Mg are prominent in all samples.

In oxygen-containing environment (Figure 6.4b), the XRD pattern for the sample heated to 300 °C is similar to that observed in the inert environment, although the peaks of MgO are slightly weaker. At 375 °C, i.e., before the main mass loss step begins following a weak mass gain (see Figure 6.3), the peaks of Mg effectively disappear while a strong MgO pattern emerges. The pattern for $Ca(IO_3)_2$ is also observed, although it is weaker than that in the as-milled powder. Finally, at 450 °C, only the MgO pattern remains clearly observed.

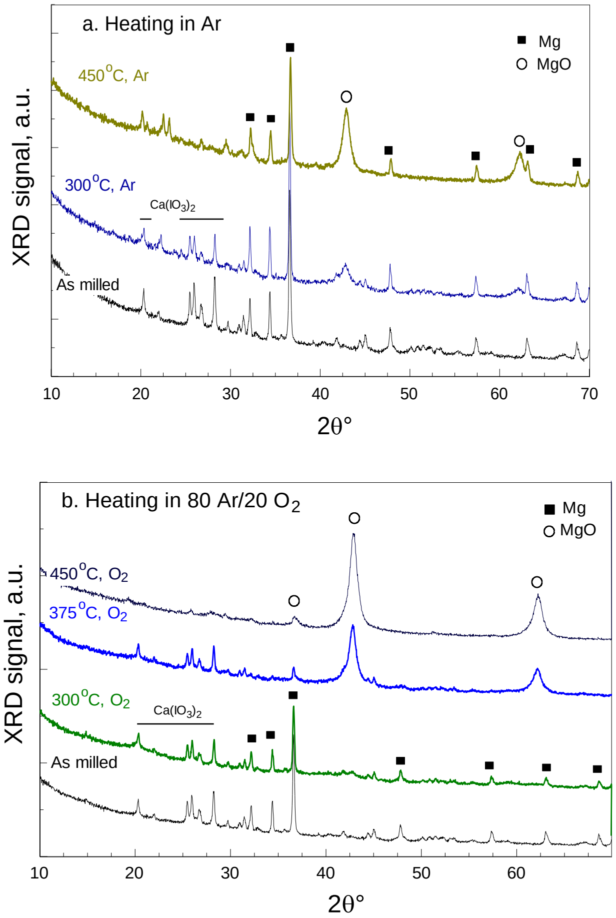

Figure 6.4 XRD patterns for $20Mg{\cdot}Ca(IO_3)_2$-PM and its quenched residue a. Heated residue quenched at 300 and 450 °C in Ar b. Heated residue quenched at 300, 375, and 450 °C in $80Ar/20O_2$.

Ignition experiments using an electrically heated wire showed an unusual, two-stage pattern for the powder ignition. This is illustrated in the sequence of high-speed video frames shown in Figure 6.5. The wire is invisible in the first frame shown (0 ms), and its location is schematically marked by dashed lines. Upon heating, powder ignites at a very low temperature, before the heated wire becomes luminous (122 ms in Figure 6.5). The following combustion event is fast, and as the wire heating continues, emission from the powder coating subsides and becomes undetectable. However, at a higher temperature, a secondary ignition event is systematically detected, as seen in the frame corresponding to 224 ms.

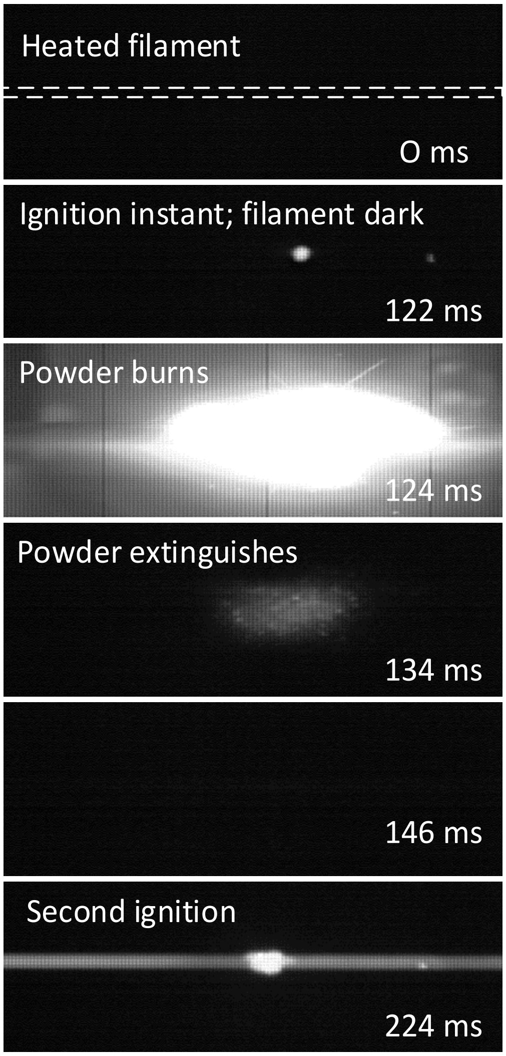

Figure 6.5 Selected frames of the video illustrating ignition of 20Mg·$Ca(IO_3)_2$-PM

The same two-stage ignition pattern is detected by the photodiode recording emission from the coated wire, as shown in Figure 6.6. Both light emission from the photodiode, and temperature recovered from the emission from the uncoated portion of the wire are shown. The temperature is measured reliably when it exceeds ca. 550 °C; it is clear that the first ignition event occurs at a lower temperature. The temperature for this event is estimated extrapolating the temperature vs. time curve to lower temperatures. The second ignition produces a much weaker optical emission peak; it is also observed on the background of a significant emission from the heated wire.

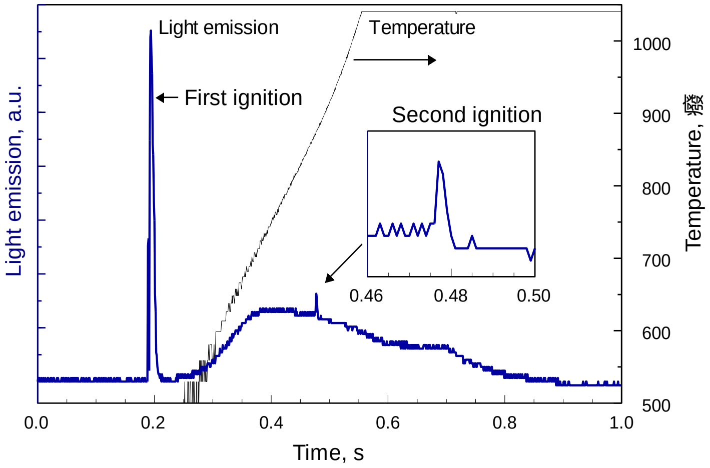

Figure 6.6 Characteristic photodiode signal monitoring emission from the powder sample ignited as a coating on an electrically heated wire.

The ignition temperature measurements were performed at different heating rates; the results are shown in Figure 6.7. The temperatures for the first and second ignition stages are shown separately. In addition, the ignition temperature for pure Mg powder was measured; it is also shown in Figure 6.7. It is apparent that the effect of heating rate on the first stage ignition temperature is significantly weaker than for the second stage ignition. Thus, first ignition event has a lower activation energy than the second ignition event observed for the prepared composite material. Interestingly, the temperatures and the heating rate dependence for the second ignition event nearly coincide with those for pure Mg.

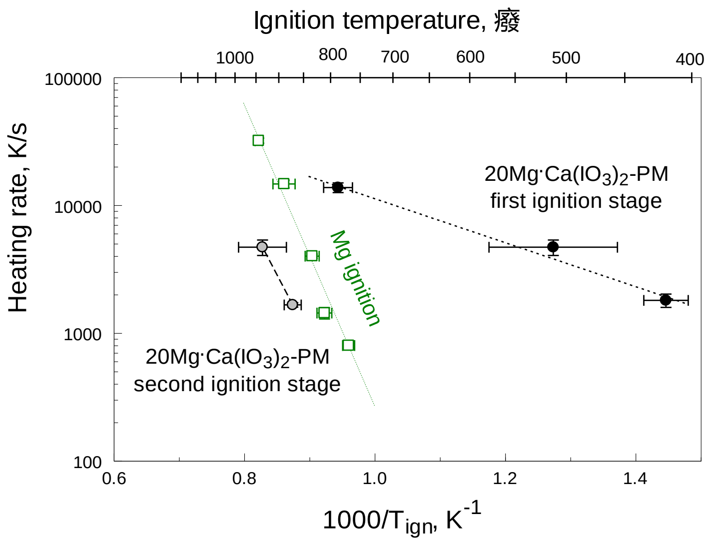

Figure 6.7 Ignition temperatures of $20Mg\cdot Ca(IO_3)_2$-PM and Mg at different heating rates

Emission traces of $20Mg\cdot Ca(IO_3)_2$–PM particles ignited by the laser beam and burning in air and ignited and burning in the products of an air-acetylene flame are shown in Figure 6.8 a, and b, respectively. Emission filtered at both 700 and 800 nm was recorded and is shown in Figure 6.8. For the particle burning in air, Figure 6.8a, the emission pulse is very short and relatively featureless, similar to those reported for combustion of pure Mg particles in the same experiment (Liu, Schoenitz, and Dreizin 2018a). The temperature trace is also shown in Figure 6.8a. Although the temperature vs. time behavior does not appear reasonable (it exhibits a minimum, rather than a maximum expected based on the emission trace), the range of temperatures measured while the emission signal is strong likely represents the flame temperature, at least approximately. This temperature range is rather low, 1200 – 1400 K, and it is right around the boiling point of Mg. Similar temperature readings were obtained for multiple burning particles. A histogram representing average temperatures for different emission pulses is shown in Figure 6.9. The temperatures were averaged over a portion of the emission pulse while its signal exceeded half of its peak value for each pulse. A dashed line shows the boiling temperature for Mg, making it clear that the measured temperatures are grouped around it.

For particles injected in the air-acetylene flame, the emission pulses have an unusual, two-peak structure, Figure 6.8b. The first peak is very sharp; it is followed by a comparable or even stronger second peak, extended in time. Unfortunately, because of the additional emission produced by the hydrocarbon flame, the temperature measurements for these experiments were not successful.

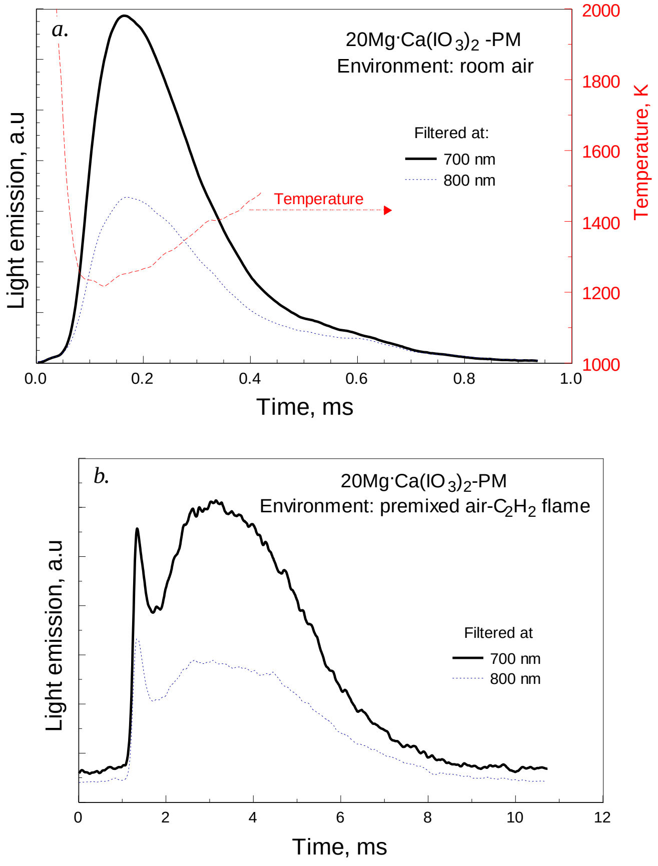

Figure 6.8 Emission pulses produced by burning 20Mg·Ca$(IO_3)_2$-PM particles a. Ignited by the laser beam and burning in air. b. Ignited and burning in products of a premixed air-C_2H_2 flame.

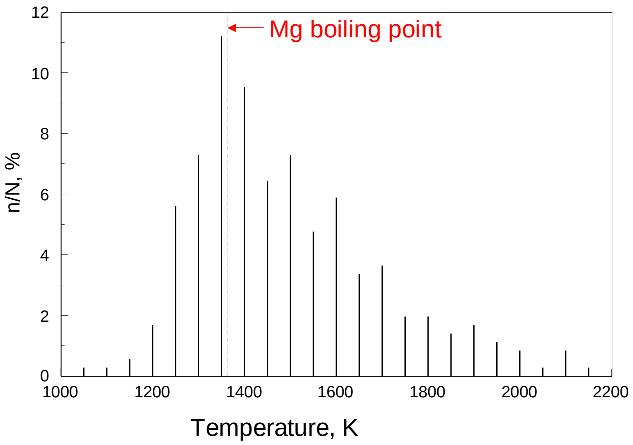

Figure 6.9 Distribution of temperatures for 20Mg·Ca(IO_3)$_2$-PM particles ignited by laser beam and burning in air averaged during the time the particle emission exceeds half of its peak value.

Statistical distributions of the measured emission pulse durations for particles burning in both environments are shown in Figure 6.10. In agreement with qualitative observations illustrated in Figure 6.8, the emission pulses are much longer for the particles burning in the air-acetylene flame compared to those burning in air. Separately, durations of the first peak in the two-peak structure of the emission pulses recorded in the flame were analyzed. The result of this analysis is shown as an inset in Figure 6.10; the time scale of the inset (0.3 – 2 ms) is the same as in the main plots in Figure 6.10. The duration of the first peak occurring in the air-acetylene flame is close to that of the entire emission pulse produced by the same particles ignited by laser beam and burning in air.

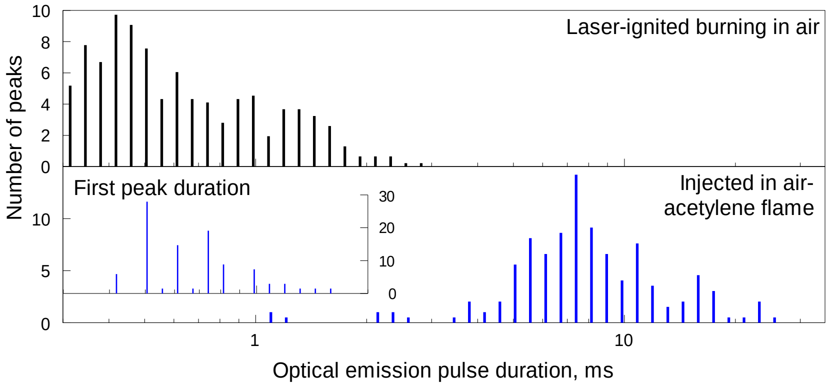

Figure 6.10 Distributions of $20Mg \cdot Ca(IO_3)_2$ particle emission pulse durations for the combustion experiments in air and products of an air-acetylene flame. The inset shows duration of the first peak observed only in air-acetylene flame.

Correlating particle size distributions shown in Figure 6.2 with the distribution of durations of the emission pulses produced by burning particles yielded trends shown in Figure 6.11 and reflecting the effect of particle sizes on their burn times. For comparison, similar trends are shown that were obtained recently for the Mg powder that was used as the starting material for preparation of the present composite (Liu, Schoenitz, and Dreizin 2018b). As expected from Figs. 6.8 and 6.10, the burn times for the composite powder are much shorter in air than in the products of an air-acetylene flame. For both environments, pure Mg powder burns slightly faster than the composite. It also appears that the effect of particle size on its burn time is generally stronger for the composite than for the pure Mg powders.

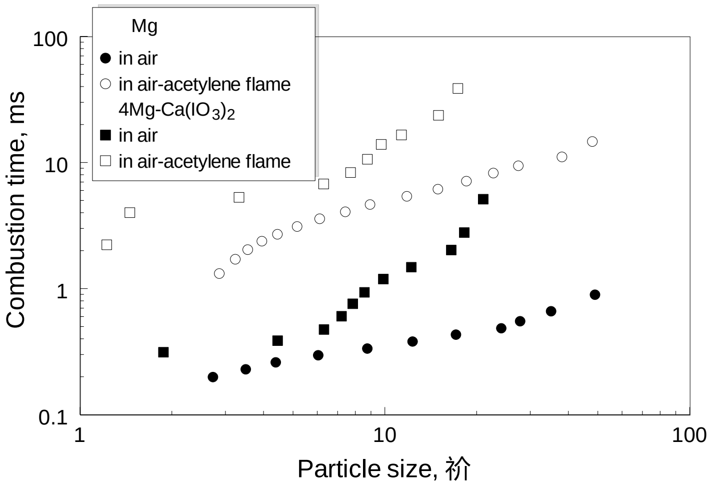

Figure 6.11 Effect of particle size on its combustion time for $20Mg{\cdot}Ca(IO_3)_2$–PM and Mg powders burning in air and products of an air-acetylene flame.

6.6 Discussion

The composite powder $20Mg{\cdot}Ca(IO_3)_2$–PM prepared in this work contains 29 wt % of iodine, is easily handled in air, and is highly reactive. It also contains oxidized calcium (about 6.4 wt %), which cannot be reduced by oxidation of magnesium, and thus necessarily diminishes the material's overall energy density. The mixing between Mg and $Ca(IO_3)_2$ is quite homogeneous and the composite consists of roughly equiaxial particles with Mg matrix and nanosized inclusions of $Ca(IO_3)_2$. A large fraction of iodine is released when the composite is heated to relatively low temperatures; however, the low-temperature iodine release is incomplete. Results of TG measurements (Figure 6.3) show that when the material is heated to about 700 K, close to 10 wt % of iodine (or one third of that available initially) is still retained, although calcium iodate has decomposed and significant fraction of magnesium has already oxidized (even in argon), as seen from XRD patterns in Figure 6.4. Assuming that, as reported earlier (Fujii et al. 1977; Pechkovskii and Sofronova 1965), the first stage of decomposition of $Ca(IO_3)_2$ results in the formation of $Ca_5(IO_6)_2$ with all excess iodine removed, but all oxygen retained to oxidize magnesium, the weight loss is estimated to be 23 %. The experimentally observed weight loss is slightly lower than 20 %, suggesting that even the first stage of decomposition of $Ca(IO_3)_2$ may be incomplete. The measured TG traces, including multiple stages of weight loss, suggest that this first stage of $Ca(IO_3)_2$ decomposition includes several processes, characterized by their specific rates. The present measurements are insufficient to identify such processes and their respective rates, while it is clear that the decomposition occurs at temperatures as low as 50 °C, when the TG measurement begins (Figure 6.3).

Such low temperature reactions, releasing iodine and commonly generating fresh surface in the heated sample often lead to ignition of reactive materials. Extrapolating the trend for ignition temperature vs. heating rate for the first stage ignition (Figure 6.7) to the range of low heating rates points to room temperature at the heating rate of ca. 100 K/s, which is still greater than that used in the TG measurements. It can thus be suggested that the initial steps of $Ca(IO_3)_2$ decomposition occurring at very low temperatures lead to ignition of the prepared materials. It is interesting that the oxidation of magnesium in this first process is incomplete despite the availability of surrounding air, and the remainder of magnesium ignites when the temperature approaches that of ignition of pure magnesium. The magnesium igniting at the high temperature must have adhered to the wire, and thus it was not exposed to the high-temperature flame developed during the first stage ignition. Probably only a small fraction of magnesium remained unoxidized, explaining the relatively weak emission observed during the second ignition. When the second ignition occurs, it is reasonable to assume that $Ca(IO_3)_2$ was fully decomposed and its only remaining effect on the reactive material was an increase in the material's heat capacity (or reduction in its energy density) due to the presence of oxidized calcium. Because of that, the ignition temperature measured here is slightly higher than that of pure Mg.

The two-stage combustion observed for the prepared material in the air-acetylene flame (Figure 6.8b) is also likely associated with the two-stage decomposition of $Ca(IO_3)_2$. The material ignites readily, triggered by the first stage of this decomposition process. However, oxidation of Mg in the metal-rich composite is mostly driven by its reactions with surrounding gas phase oxidizing species, CO_2, CO, and H_2O, and the rate of such oxidation is lower than that of the oxidation of Mg by O_2, generated when $Ca(IO_3)_2$ decomposes. Initial release of O_2 boosts initial burn rate of the composite particles; when this oxygen is consumed, the combustion continues at a lower rate while the remainder of Mg reacts with products of the hydrocarbon flame.

For the particles ignited by the laser beam in air, oxygen is the only oxidizer available, whether it is produced by decomposing $Ca(IO_3)_2$ or comes from air. Thus, the very rapid reaction started by decomposition of $Ca(IO_3)_2$ continues at the same rate, leading to much shorter overall burn times. It is interesting that the measured flame temperature is close to the boiling point of Mg, which suggests that the emission from the standoff flame is weak and the emission comes predominantly from the burning particle surface. This measured temperature is substantially lower than 3119 K obtained as the adiabatic flame temperature for the prepared composite material burning in air using the NASA CEA code (McBride and Gordon 1996). Therefore, combustion is rate-limited by the surface reaction kinetics, and occurs without forming a vigorous vapor-phase flame.

6.7 Conclusion

A reactive composite material combining magnesium with calcium iodate, and containing 29 wt% of iodine was prepared by mechanical milling. The material was metal-rich with 75% of magnesium expected to react with surrounding oxidizers rather than the products of decomposition of calcium iodate. The prepared material was stable and easy to handle; similarly prepared composites with lower magnesium content are unstable and difficult to store and handle. The material releases iodine readily upon heating; however, release of iodine occurs over a rather broad range of temperatures, likely following multiple reactions involved in decomposition of calcium iodate. Prepared powders ignited readily upon heating, and the ignition occurred in two steps. The first ignition step occurred between 400 and 800 °C, depending on the heating rate. The second ignition step occurred close to 900 °C, just slightly above the ignition temperature of pure magnesium. Combustion of the prepared powders in the products of air-acetylene flame also proceeds in two steps as indicated by the recorded optical emission traces produced by burning particles. It is proposed that the two-stage patterns in both ignition and combustion are associated with the two-stage decomposition of calcium iodate. Combustion of the prepared powders in air occurs much faster than in the products of the air-acetylene flame; the two-step combustion pattern is not observed for experiments in air. Burn rates of the prepared composite powders in both air and products of air-acetylene flame are slightly lower than those of pure magnesium burning in the same environments.

CHAPTER 7

IODINE RELEASE BY COMBUSTION OF COMPOSITE Mg·Ca(IO_3)$_2$ POWDER

7.1 Abstract

Concentration of iodine generated by combustion of a reactive material (RM) powder, Mg·Ca(IO_3)$_2$, injected in an air-acetylene flame was measured as a function of height above the flame using absorption of collimated emission from a tunable laser diode. The absorption by atomic iodine was sufficient to be quantified when the powder feed rate into the flame was close to 50 mg/s. The measurements were compared to calculations using a simplifying assumption that iodine is released by burning RM particles at a constant rate during their combustion. The calculated iodine profiles were produced using a computational fluid mechanics model considering iodine released by burning RM particles. The particle size distribution was taken into account as well as the experimentally determined trend of particle burn times vs. their sizes. The predicted iodine release was split between molecular and atomic iodine according to the ratio between these species expected to be in thermal equilibrium at the flame temperatures. Both calculated and measured iodine concentrations exhibit similar increase and decrease as a function of height, suggesting that a constant rate of iodine release by a burning RM particle during its entire burn time may be a reasonable assumption. However, the absolute values of the measured concentrations of atomic iodine are lower than those predicted. This discrepancy may be attributed to formation of other iodine-bearing species expected to be metastable for the temperatures involved.

7.2 Introduction

Reactive materials (RMs) generating biocidal combustion products are desired to enable prompt inactivation of harmful spores and bacteria that can be released in an explosion involving biological weapons of mass destruction (Eneh 2012). Biocidal species are expected to de-functionalize bio-weapon agents before they are dispersed to contaminate surrounding areas (Clark and Pantoya 2010; Farley and Pantoya 2010; Feng et al. 2013; He, Hooper, and Shreeve 2016; Henderson et al. 2015; Wu et al. 2017). Halogens and, in particular, iodine were shown to be effective as such biocidal species (Grinshpun et al. 2012; Feng et al. 2013; Johnson and Higa 2013; Grinshpun et al. 2017; Wu et al. 2017; Nakpan et al. 2018). Research thus focused to design iodine-bearing RMs capable of releasing both heat and iodine rapidly upon ignition; often such materials have thermite compositions with iodine-containing oxidizers (Liu, Schoenitz, and Dreizin 2017, 2019; Wang, Kline, et al. 2018; Clark and Pantoya 2010; Sullivan et al. 2011a; Wang et al. 2015; Wang et al. 2017b). A quantitative model was recently proposed linking thermal and chemical effects of the iodine-bearing combustion products with their biocidal effectiveness (Wang, Schoenitz, et al. 2018). In order to describe these effects quantitatively, spatial distributions of both iodine-containing species and temperature were required. Obtaining the temperature distribution may be based on heat transfer analysis accounting for combustion models for the RM particles, typically derived from laboratory particle combustion experiments (Wang et al. 2016; Wang, Mohan, and Dreizin 2016; Wang, Schoenitz, and Dreizin 2017; Liu, Schoenitz, and Dreizin 2018a). In order to describe distribution of iodine, mass transfer was considered with a simplifying assumption of iodine being continuously released by each burning RM particle at a constant rate during its entire burn time. However, no data has been available to validate that assumption. More generally, the information about real time release of iodine or other iodine-bearing biocidal species by burning RM powders is lacking. This work begins addressing this deficiency by quantifying release of atomic iodine from a burning nanocomposite thermite powder including an iodine-bearing oxidizer.

7.3 Experimental Section

An experimental setup involving powders of different RMs fed into a laminar air-acetylene flame was used to characterize biocidal efficiency of many iodine bearing materials (Grinshpun, Adhikari, et al. 2010; Grinshpun, Li, et al. 2010; Grinshpun et al. 2012; Grinshpun et al. 2017; Nakpan et al. 2018). The same experimental configuration was adopted here. The concentration of iodine at different heights above the RM particle-seeded flame was probed optically using a method based on tunable diode laser absorption spectroscopy (Hodgkinson and Tatam 2013). The concentration of atomic iodine was measured directly by tunable diode laser absorption spectroscopy of the F'=3 triplet of the hyperfine structure in the 1315 nm atomic iodine transition. The laser source was a 10 mW Qphotonics distributed feedback laser (QDFBLD-1300-5) controlled by a Thorlabs laser driver (CLD 1015). The signal to the driver was provided by a BK Precision 4052 function generator. A ThorLabs DET20C photodiode was used as the detector. A similar experiment was described recently elsewhere (Murzyn et al. 2018).

The RM used in this experiment was a thermite with Mg fuel and $Ca(IO_3)_2$ oxidizer, shown in previous research to be stable in room air, while it ignites readily and burns vigorously upon heating (Oxley et al. 2017; Liu, Schoenitz, and Dreizin 2017; Wang et al.

2017b). Details of its preparation and characterization are available elsewhere (Liu, Schoenitz, and Dreizin 2019). Briefly, the RM was prepared by arrested reactive milling (Dreizin and Schoenitz 2009). 99.8% pure, -325 mesh Mg powder by Alfa Aesar and 98% pure $Ca(IO_3)_2$ by Sigma Aldrich were used as starting materials. The composite powder was metal-rich with a fuel/oxidizer equivalence ratio of 4, considering a reaction $5Mg+Ca(IO_3)_2 \rightarrow 5MgO+CaO+I_2$. It contained 29 wt% of iodine.

A schematic diagram of the experimental setup is shown in Figure 7.1. In previous experiments, RM powder was fed in the flame at a constant rate of about 1 mg/s. Flow rates of air, acetylene and nitrogen were 4.75, 0.425 and 0.944 L/min, respectively. In preliminary experiments, the same flow parameters were used. It was observed that the concentration of iodine released was too low for a reliable detection. Respectively, the experiment was modified. Instead of a continuous flow, a charge of 10 mg of the RM powder was puffed in the flame using pressurized nitrogen. The nitrogen feed line was disconnected from a plastic tube connected to the nozzle. A weighed batch of powder was loaded in that tube. The line with nitrogen flowing was then re-connected so that a puff of powder injected in the flame was produced. For each puff, the concentration of iodine was measured at a selected height above the burner tip. The heights of the laser beam collimator above the nozzle varied from 3 to 10 cm at a 1 cm increment. The absorption could be quantified during a certain time following a single puff. This time varied depending on the height at which the optical system was located. The absorption was measured during ca. 160 ms when the detector was located at the height where the strongest absorption was observed (see below). This gave an effective puff duration and thus the average feed rate for the RM powder as 62.5 mg/s.

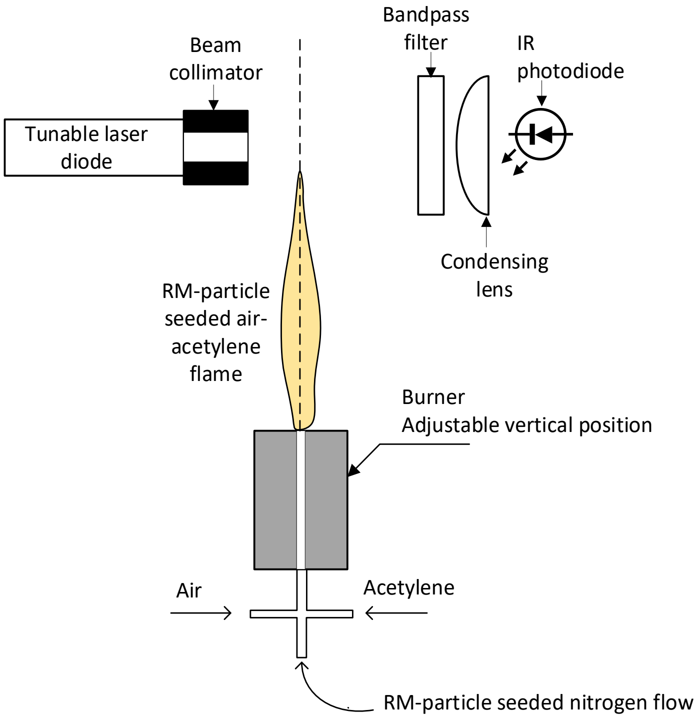

Figure 7.1 Schematic diagram of the experimental setup for measuring laser light absorption by atomic iodine

Concentration of atomic iodine, n_{iodine}, is proportional to absorbance of the laser beam, which can be described as an 11.75 cm-long cylinder with the diameter of 2 mm:

$$n_{iodine} = 24\left[\frac{\left(\frac{cW_{lu}}{h\tilde{\nu}B_{lu}L}\right)}{g_i + g_j + g_k}\right] \tag{7.1}$$

where W_{lu} is Integrated Absorbance of the Transmission Curve, B_{lu} is the summation of all Einstein *B* coefficients for the *F'*=3 transitions being scanned over, *L* is the path length, it is set to be 11.75 cm, *c* is the speed of light, *h* is Planck's constant, $\tilde{\nu}$ is the transition wavenumber, and n_{iodine} is the number density of atomic iodine in number per cubic meter.

As the integrated absorbance includes contributions from all three hyperfine states, $g_i + g_j + g_k$ it is the summation of all *2F*+1 degeneracies of the hyperfine components in the blended triplet structure. The partition function was taken at a fixed value of 24.

7.4 Experimental Results

Characteristic traces measuring the concentration of elemental iodine as a function of time for several nominally identical RM puffs are shown in Figure 7.2. These measurements were taken at the height of 5 cm above the burner tip. Each temporal concentration profile likely represents the distribution of the RM powder injected in the flame during the puff. Profiles are complicated in shape, representing the superposition of iodine release pulses produced by individual burning particles. The duration of each pulse is equal to or shorter than individual particle burn time. Although the exact shapes of individual traces are not reproduced, the general features including a relatively long raise time and a faster decay are repeatable.

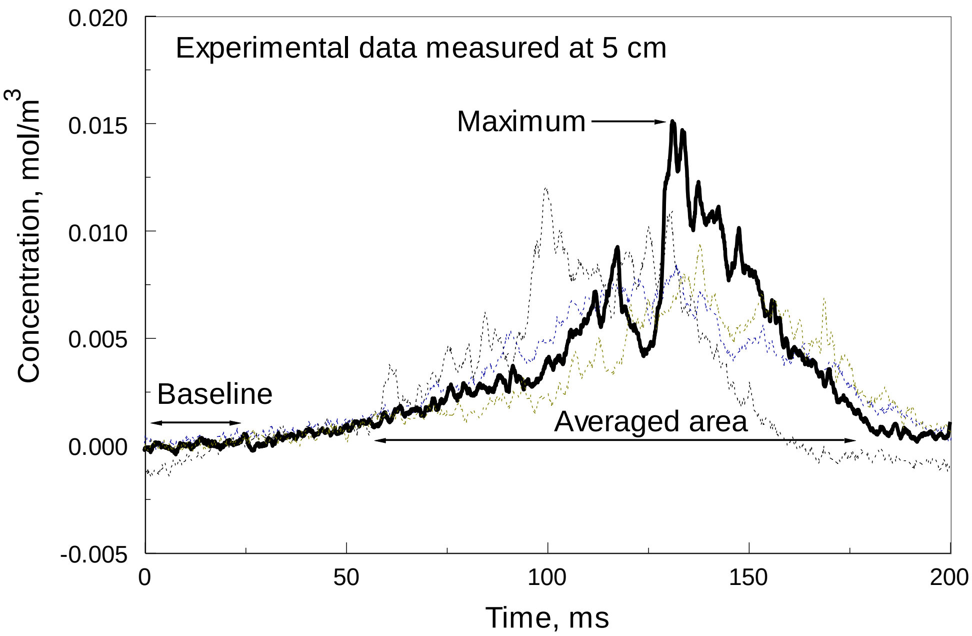

Figure 7.2 Characteristic traces showing concentration of atomic iodine inferred by the laser absorption measurements. The height is 5 cm above the burner.

For each recorded trace, the time duration, its maximum value, as well as the average concentration were determined. The time duration was measured when the signal exceeded the baseline level by 300%. The results of these data analyses are summarized in Table 7.1.

Table 7.1 Summary of Experimental Results

Measurement height (cm)	Baseline error (mmol/m^3)	Maximum concentration (mmol/m^3)	Average concentration (mmol/m^3)	Residual time (ms)
3	0.21±0.12	10.12±3.19	2.22±0.52	0.13±0.02
4	0.21±0.07	8.9±0.59	4.47±0.49	0.17±0.02
5	0.23±0.13	11.44±1.94	3.47±0.63	0.15±0.02
6	0.22±0.01	13.91±3.15	4.98±0.76	0.16±0.01
7	0.16±0.03	12.02±2.01	4.15±0.51	0.2±0.02
8	0.16±0.01	14.39±2.20	3.24±0.42	0.17±0.00
9	0.24±0.01	10.81±1.4	1.44±0.21	0.19±0.02
10	0.21±0.02	4.02±0.21	1.41±0.12	0.12±0.05

7.5 Computational Approach Predicting Iodine Release

For comparison with experimental data, the concentration of iodine was simulated computationally. Following earlier work (Wang, Schoenitz, et al. 2018), it was assumed that iodine is released at a constant rate during the time the RM particles burn. A separate calculation was performed assuming that the iodine release rate is ten times faster than the particle burn rate. This latter approach could be justified considering that iodine is much more volatile than magnesium or its combustion products. Comparing outcomes of both calculations with the experiment helps in determining which description represents the reality better.

As earlier (Wang, Schoenitz, et al. 2018), the concentration profile of iodine was obtained using COMSOL 5.2a software. This calculation accounts for various particle sizes and their respective burn times, affecting the iodine release in experiments. A 2D axisymmetric model was considered with the geometry shown in Figure 7.3. The diameter of the computational domain was 5.875 cm to match the optical path length of the laser beam used in experiments. The boundaries of the computational domain were kept at room temperature and pressure. Open boundaries allowed species to enter or leave the domain. The model describing the air-acetylene flame was the same as in a previous work (Chintersingh et al. 2016b), where it was validated by measurements of the flame temperature and flow velocity profiles. The experimental flowrates for air, nitrogen, and acetylene were used to determine the equivalence ratio in the flame. The concentrations of the main flame product species: CO_2, CO, H_2O, and N_2, were obtained from thermodynamic equilibrium calculations for the air-acetylene flame using CEA NASA code (McBride and Gordon 1996). These flame product species were introduced in the computational domain at the height of 0.25 cm above the nozzle, where the flame front was observed in experiments. The bottom inset in Figure 7.3 shows the configuration of the burner nozzle. The top inset describes how iodine injection into the flame was modeled. The total rate of the iodine injection and rate of injection at different heights above the burner were determined accounting for the distribution of the burn times of the RM particles and for the average RM powder feed rate.

The specific geometry at which iodine entered the system was represented by two elements in the model shown in Figure 7.3. Half of iodine was introduced using a line-source placed at the axis of symmetry of the computational domain. The second half was released from a series of point sources located 1 mm away from the axis of symmetry. The distance between the point sources was 1 mm. This setup represented the experimental configuration, in which RM particles releasing iodine were focused around the vertical axis within an approximately 1-mm diameter cylinder. A simpler, one-dimensional configuration was also considered, in which iodine was released along the axis of symmetry only. However, in this case a stable solution could not be obtained from the numerical model.

Iodine release was assumed to begin when particles ignited, which occurred at a specific vertical location, 3 cm, where the ignition temperature was attained based on experimentally observed particle streaks originating from this height. The iodine releasing elements were located at and above that location. As discussed below, the rate of iodine release by individual particles varied for different calculations.

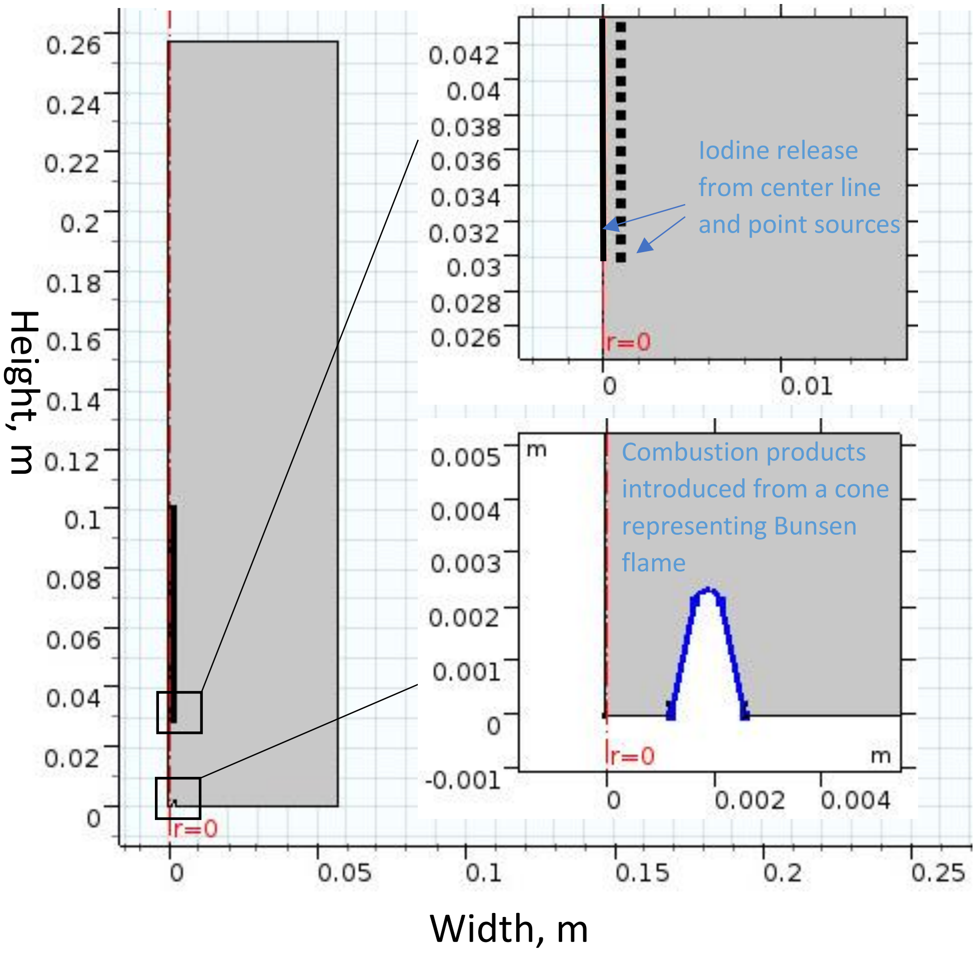

Figure 7.3 Schematic diagram of the computational domain used in COMSOL

The specific format for the iodine input in COMSOL required it to be expressed through mass source strength ($\dot{Q}_I$, units: mol/m/s) for both line and point sources. It was calculated as:

$$\dot{Q}_I \left[\frac{mol}{m \cdot s}\right] = \frac{\dot{q}_h}{\Delta h} \tag{7.2}$$

where $\dot{q}_h \left[\frac{mol}{s}\right]$ is the iodine release rate at the height h and Δh [m] is the height of the control volume for which the rate is determined.

The value of $\dot{q}_h$ was obtained as a sum of all iodine released by particles burning at that height:

$$\dot{q}_h = \sum_{i=p}^{n} \dot{N}_i \frac{m_i f}{\tau_i} \cdot \frac{\Delta h}{v_h} \tag{7.3}$$

where $\dot{N}_i$ [s^{-1}] represents the steady rate at which particles of a specific size bin are fed, m_i [g] and τ_i [s] are the particle mass and burn time, respectively, f [mol/g] is the mole fraction of iodine in the material, v_h [m/s] is the flow velocity at the height h. The summation is made for all size bins, for which the particles are burning at the height, h. In other words:

For $i \geq p$:

$$\tau_i > \int_0^h \frac{dh}{v} \tag{7.4}$$

Note that distribution of iodine among different species including atomic and molecular iodine was neglected in this analysis. All released iodine was treated as I_2. A correction necessary to account for neglecting different iodine-bearing species is discussed below.

The values $\dot{N}_i$ were determined taking into account the measured particle size distribution and the effective feed rate for the powder. The particle size distribution is shown in Figure 7.4. It is shown in terms of the mass fraction for each size bin. The integrated mass of powder fed into the flame during one puff was taken as 10 mg; the mass of one load. To obtain the feed rate, this mass was distributed in time over 160 ms, the residual time for one puff, see Table 7.1.

The burn time, τ, as a function of the particle size was taken from previous work; for reference, it is also shown in Figure 7.4 (Liu, Schoenitz, and Dreizin 2019).

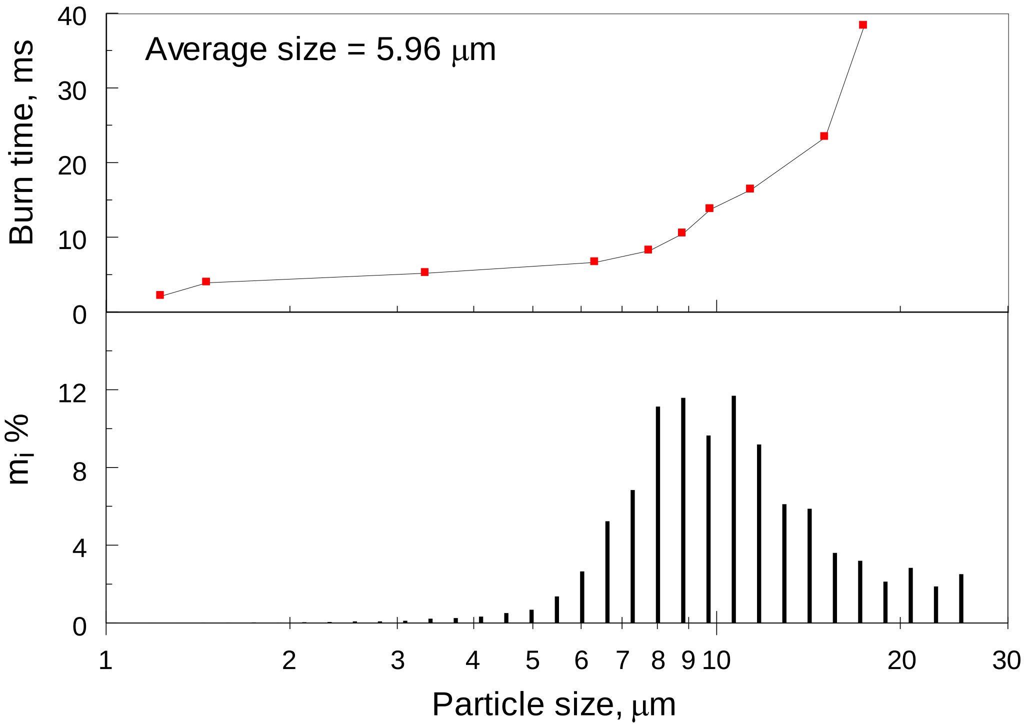

Figure 7.4 Burn time as a function of particle size and particle size distribution of the RM powder ($Mg{\cdot}Ca(IO_3)_2$) used in this work (Liu, Schoenitz, and Dreizin 2019).

The calculated rate of iodine release as a function of height is shown in Figure 7.5. This result describes the situation when it is assumed that iodine is released continuously during the entire particle burn time. The rate is affected by two factors: number of burning particles of different sizes and the velocity of the particles as a function of height. The rate keeps increasing before 6 cm, representing a situation when particles of all size bins are burning while the velocity is decreasing with height. After 6 cm, the particles start to burn out and the rate of iodine release starts decreasing.

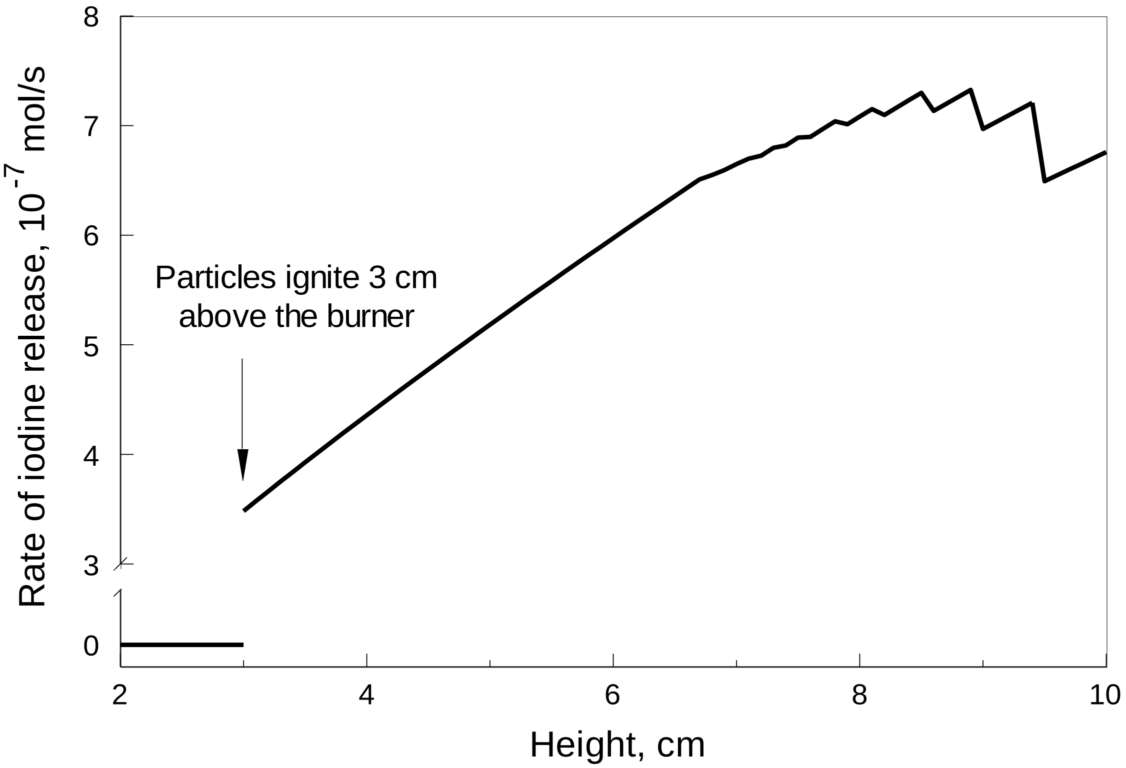

Figure 7.5 Rate of iodine release at different heights.

7.6 Calculated Iodine Release

The calculated steady state temperature and concentration profiles generated by COMSOL are shown in Figure 7.6. Illustrated is only the case when iodine is released during the entire burn time by each particle. It is first noted that the computational domain is sufficiently large so that effectively no changes from ambient temperatures or gas compositions are observed near the domain boundaries. The high-temperature zone is relatively well localized around the flame. All gas species present in the flame do not significantly dissipate horizontally. Iodine as well as other combustion products remain concentrated within a relatively narrow, 1-2 mm diameter cylinder around the axis of symmetry. Additional details describing iodine distribution are shown in Figure 7.7. The iodine concentration increases with height at the flame's axis of symmetry; it also rapidly decays away from the center of the flame. Iodine is barely detected just 5 mm away from the center.

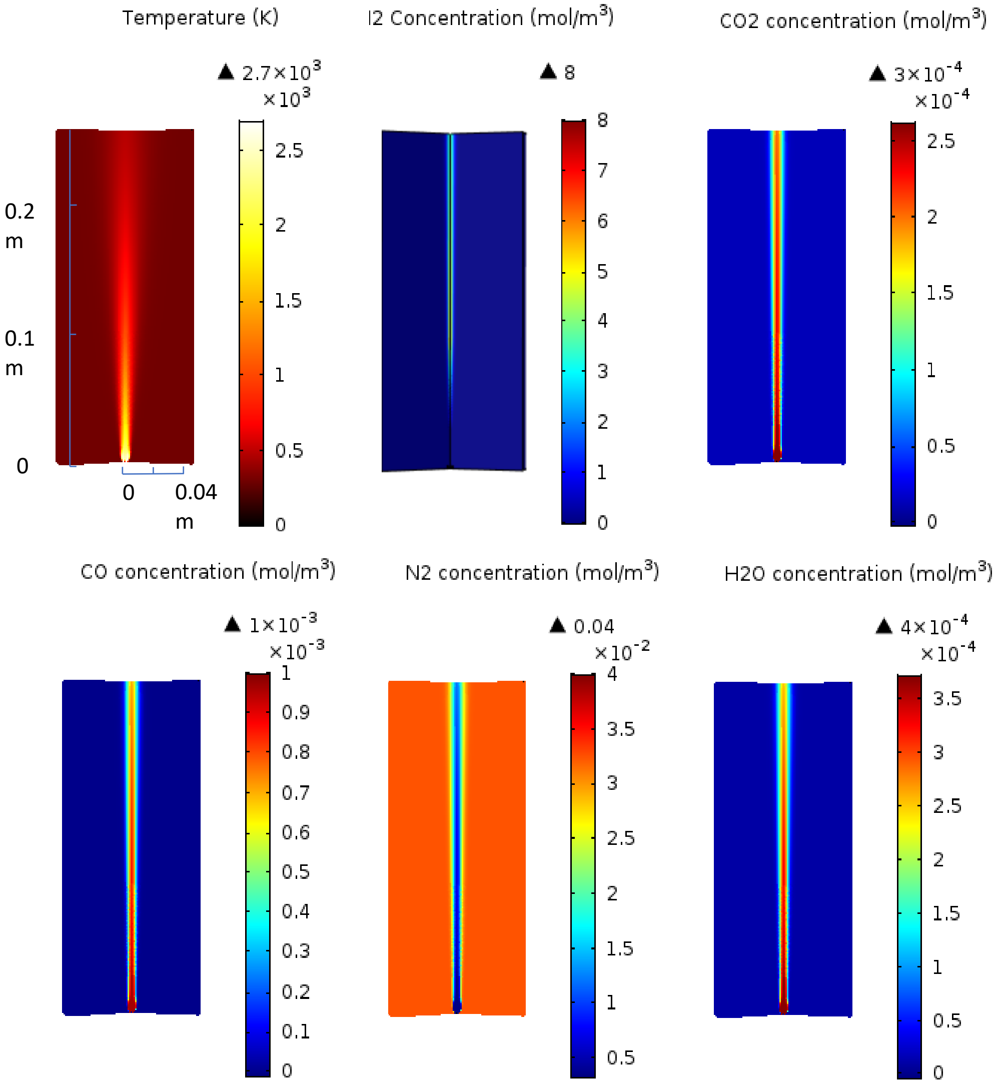

Figure 7.6 Temperature and species distributions predicted by COMSOL model. Note that iodine concentration represents I_2 as the only iodine bearing species considered in the calculation.

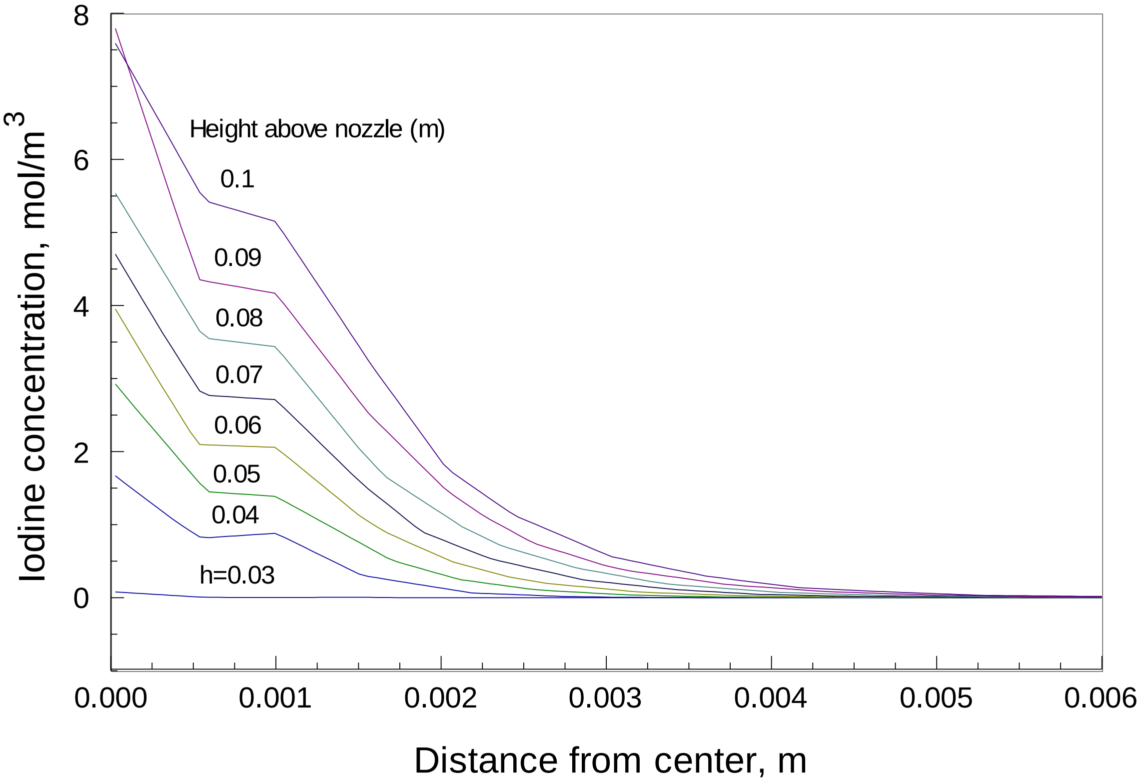

Figure 7.7 Simulated radial iodine concentration distributions at different heights.

7.7 Comparison of Calculations and Measurements

To compare the measured data given in Table 7.1 with calculation results shown in Figs. 7.6 and 7.7, iodine concentrations along the height can be considered. However, the results of calculations treated all released iodine as atomic. In experiment, multiple iodine-bearing species could have formed. An initial correction for the calculated results could be made considering the ratio of molecular to atomic iodine existing when iodine is exposed to the experimental temperatures. A set of calculations was made using the NASA CEA code (McBride and Gordon 1996) considering iodine exposed to air at 1 atm heated to different temperatures varied from 800 to 1900 K, a temperature range encountered in the range of heights of interest. Presence of both atomic and molecular iodine was accounted for. The results showed that the atomic iodine percentage varied from 8.1 to 99.8% in this temperature range. This ratio along with the temperature map (Figure 7.6) were accounted for to convert the total descriptive I_2 concentrations, as predicted in Figs. 7.6 and 7.7 to respective atomic iodine concentrations. The final comparisons of the predicted and measured concentrations of atomic iodine are shown in Figure 7.8. Two cases are shown for the predicted atomic iodine profiles: for the assumptions that iodine is released during the entire particle burn time and that iodine is released ten times faster than the particle burns out.

The experimental data are lower than both predicted profiles; the discrepancy is much greater for the case of rapid iodine release, however, for the assumed iodine release during the entire burn time, the effect of height on the iodine concentration is represented well. For the accelerated iodine release, the iodine concentration peaks at a lower height than observed experimentally.

The present calculated atomic iodine profiles were obtained assuming that all iodine is distributed among I_2 and I species. Accounting for other iodine-bearing species that can form in the flame, such as CaI_2, MgI_2, HI, etc., can further decrease the amount of elemental iodine and thus improve the agreement with the measurements. The equilibrium calculations suggest that formation of such species is very significant at high temperatures, while they become negligible at temperatures below 1500 K. It is unclear whether equilibration can occur fast enough, however. Thus, presence of metastable iodine-bearing species could be significant in affecting the accuracy of experimental assessment of iodine present in the combustion products of RMs.

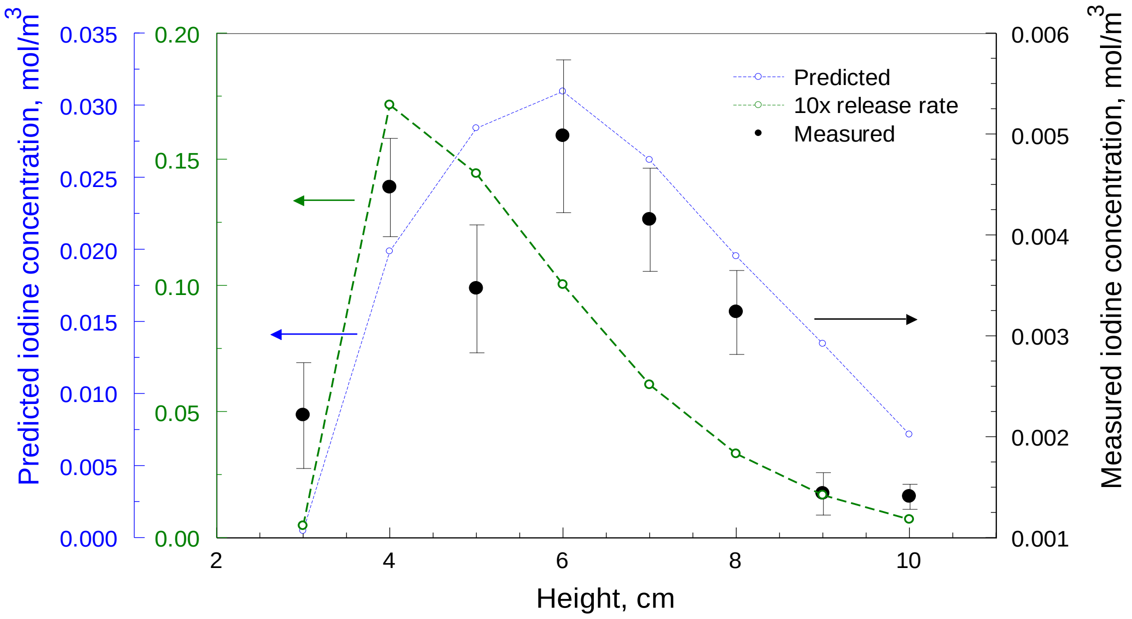

Figure 7.8 Comparison between modeled data and experimental data

The agreement between predicted and measured trends describing changes in iodine concentration as a function of height indicates that the simplifying assumption suggesting that iodine is released at a constant rate during the particle combustion may indeed be acceptable.

7.8 Conclusions

The sensitivity of iodine concentration measurements using tunable diode laser absorption spectroscopy was insufficient to detect iodine released by a RM powder containing ca. 29 wt % of iodine and fed into an air-acetylene flame at approximately 1 mg/s. Increasing the mass feed rate of the RM to ca. 50 mg/s made the measurements possible. The measured atomic iodine concentration profiles as a function of height were compared to those predicted using a computational fluid mechanics model accounting for iodine emitted by burning RM particles. For calculations, two assumptions for iodine release rate were considered: iodine was assumed to be released at a constant rate either equal to or ten times exceeding the rate of particle combustion. The calculated iodine vs. height profiles were corrected accounting for the ratio between atomic and molecular iodine in equilibrium as a function of temperature. Measured elemental iodine concentration is lower than those predicted using both assumptions for the iodine release rate; the discrepancy is smaller when iodine is released at the same rate as the rate of combustion. Assuming the iodine release occurring at the same rate as particle combustion, both measurements and calculations show similar peaks in the iodine concentration vs. height traces; however, the peak is predicted at a lower height when an accelerated iodine release is assumed. Results suggest that the assumption of iodine release at the rate equal to the particle burn rate describes the experiments better. A systematic discrepancy between the measured and predicted iodine concentration levels may be due to existence of metastable iodine bearing species different from molecular or atomic iodine.

CHAPTER 8

CONCLUSIONS

Among high energy density metals, boron and magnesium could potentially be used in biocidal applications as a fuel or fuel additive. Understanding combustion mechanisms and behaviors of metals are crucial. Boron has its naturally grown oxide layer, which hinders the combustion. Efforts in this work focused on using surface modification methods and chemical reaction to reduce the boron oxide layer. Oxide layer of boron could be reduced to 2.5% to its initial value after ultrasonically washing 95% pure boron in acetonitrile. Additional boron surface functionalization by toluene leads to a more stable powder in air than initial powder, however, commercial 99% pure boron is more stable based on the microcalorimetric measurements in humid air. A functionalized washed powder has lower apparent activation energy of oxidation comparing to the starting commercial 95% pure boron and commercial 99% pure boron, suggesting that a shorter ignition delay is achievable upon its thermal initiation. The results suggest that boron has different oxidation mechanisms at different temperatures. At low temperatures, (close to room temperature or slightly above) slow oxidation (aging) of boron is affected by impurities of boron surface, such as MgO. At high temperature, reaction rate is limited by the diffusion through a growing B_2O_3 layer. Surface modified material is found to be a more attractive fuel for practical use.

Combustion of fine Mg is characterized in various oxidizing environments since Mg is a fuel shown to generate directly biocidal combustion products. Burn times in air are less than 1 ms for fine Mg particles with size less than 10 µm. The burn time and particle size correlation follows a t~d$^{0.5}$ trend. Combustion product is MgO particles with size similar to the initial Mg. No luminescent halo or smoke cloud was observed, suggesting that Mg smoke was not produced during combustion. Both burn times and burning temperatures decreased when particles were introduced into combustion zone by faster carrier air flow. The experimental results suggest that Mg oxidation occurs very near to the boiling Mg surface and the rate is controlled by both surface kinetics and oxygen diffusion. MgO crystals form directly on particle surface and/or deposit onto liquid Mg from nearby standoff flame zone, leading to non-spherical combustion product particles with the size close to that of unburned Mg. Fine Mg oxidizes slower in products of premixed C_2H_2/air flame and H_2O, suggesting that air is a more effective oxidizer for Mg than H_2O or mixture of CO/CO_2 and H_2O.

Combustion of composite Mg·S particles as a fuel potentially generating biocidal products is also explored and tested. The combustion follows a two-step process. When the composite is introduced into a CO_2 laser beam, sulfur is rapidly evaporated from the particle side heated by the laser, leading to a sudden velocity change for the igniting particle. Once sulfur is removed, the particles burn similarly as pure Mg.

Both boron and magnesium are mechanically milled into a reactive composite where magnesium is expected to promote boron combustion. During milling, Mg reacts with boron oxide and forms MgO. Milled composite has a lower ignition temperature compared to pure magnesium. Selective initial ignition of magnesium provides energy leading to combustion of boron. Boron powders with or without surface modification (by acetonitrile wash) are used to prepare such composites. Experimental results show that amount of boron oxide and formation of MgO are reduced in the sample with surface treatment. Such material contains increased amount of reactive Mg and has a stronger first oxidation step due to selective Mg oxidation. Thinner boron oxide layer and a greater energy released by Mg oxidation leads to a faster ignition of the composite, especially when a high-heating rate source, such as electric spark are employed.

B-I_2 materials with iodine as a fuel additive are prepared by mechanical milling. Milling conditions and compositions are optimized. 30 wt% of iodine can be stabilized in the solid composite up to 400 ^oC. A major iodine-releasing step with a quick release rate occurs when the material is heated to 400 ^oC; it represents the breakdown of boron-iodine metastable compound. Iodine release slows down after 500 ^oC, it is finished at 750 ^oC.

$B\cdot I_2$ composite then mechanically milled with $Ca(IO_3)_2$ to form a biocidal thermite. Produced thermite is loosely agglomerated, B-I_2 composite is embedded with micron-size particles of $Ca(IO_3)_2$. $B\cdot I_2\cdot Ca(IO_3)_2$ ternary system is developed as a reactive material with high iodine concentration. Such composite contains 57.6 wt% of iodine. The material ignites at 300 ^oC, around 100 ^oC lower than ignition temperature of $B\cdot Ca(IO_3)_2$ binary composite which uses boron as a fuel instead of $B\cdot I_2$. Ternary $B\cdot I_2\cdot Ca(IO_3)_2$ composite was found to burn similarly to the binary $B\cdot Ca(IO_3)_2$ composite which is described elsewhere (Wang et al. 2017b). The flame temperature is close to 2050 K, and combustion is dominated by vapor-phase reaction, producing fine spherical oxide particles in which boron and calcium oxides are mixed homogeneously.

$Mg\cdot Ca(IO_3)_2$ binary thermite system is developed and tested due to the biocidal property of both MgO and I_2. The prepared mechanically milled thermite with metal rich composition is stable and easy to handle. Such material contains 29 wt% of iodine and releases iodine upon heating. The iodine releasing steps correlate with the decomposition of $Ca(IO_3)_2$ at low heating rates. Ignition of such material occurs in two steps. The first step occurs within 400-800 ^oC depending on the heating rate. The second step of ignition occurs at 900 ^oC, which is similar to the ignition temperature for the pure Mg. Combustion of the material in products of an air-C_2H_2 flame shows particle emission pulses with double peak features. Material burns much faster in air and the two-steps pattern is not observed. The burn rate of such material is slightly slower than that of pure Mg with same size in the same oxidizing conditions.

The iodine released by the above material ignited in the products of an air-C_2H_2 flame is simulated using COMSOL and compared with the experimental atomic concentration measured by tunable diode laser absorption. Simulations use a computational fluid mechanics and compare two assumptions about the iodine release rate by a burning particle. One approach assumes that iodine is released at a constant rate during the entire particle burn time; the other assumes that iodine is released during the first 10% of the particle burn time. The results of simulations follow correlate with the experimental data better when the iodine is assumed to be released at a constant rate during the entire particle burn time. However, the predicted atomic iodine concentration is systematically lower than that of experiment. This discrepancy may be due to additional metastable iodine-bearing combustion products other than the ones considered in simulation, which only accounted for molecular and atomic iodine.

REFERENCES

Abraham, A., J. Obamedo, M. Schoenitz, and E. L. Dreizin. 2015. 'Effect of composition on properties of reactive Al·B·I2 powders prepared by mechanical milling', *Journal of Physics and Chemistry of Solids*, 83: 1-7.

Abraham, A., M. Schoenitz, and E. L. Dreizin. 2013. "Metal-based reactive materials with biocidal reaction products." In *Particle Technology Forum 2013 - Core Programming Area at the 2013 AIChE Annual Meeting: Global Challenges for Engineering a Sustainable Future*, 441-42.

Abraham, A., S. Zhang, Y. Aly, M. Schoenitz, and E. L. Dreizin. 2014. 'Aluminum-iodoform composite reactive material', *Advanced Engineering Materials*.

Abraham, Ani , Ziyue Zhong, Ruodong Liu, Sergey A. Grinshpun, Michael Yermakov, Reshmi Indugula, Mirko Schoenitz, and Edward L. Dreizin. 2016. 'Preparation, ignition and combustion of Mg·S reactive nanocomposites', *Combustion Science and Technology*, 188: 1345-64.

Aly, Y., and E. L. Dreizin. 2015. 'Ignition and combustion of Al·Mg alloy powders prepared by different techniques', *Combustion and Flame*, 162: 1440-47.

Aly, Y., S. Zhang, M. Schoenitz, V. K. Hoffmann, E. L. Dreizin, M. Yermakov, R. Indugula, and S. A. Grinshpun. 2014. 'Iodine-containing aluminum-based fuels for inactivation of bioaerosols', *Combustion and Flame*, 161: 303-10.

Aly, Yasmine, Mirko Schoenitz, and Edward L. Dreizin. 2013. 'Ignition and combustion of mechanically alloyed Al-Mg powders with customized particle sizes', *Combustion and Flame*, 160: 835-42.

Andrey, D., P. Zbinden, M. K. Wah, and W. Lee. 2001. 'A routine quality control method for the determination of iodine in human and pet food by ICP-MS', *Atomic Spectroscopy*, 22: 299-305.

Arnold, Werner, and Ernst Rottenkolber. 2009. 'Combustion of boron loaded explosives', *Int. Annu. Conf. ICT*, 40th: 37/1-37/10.

Badiola, C., and E. L. Dreizin. 2012. 'On weak effect of particle size on its burn time for micron-sized aluminum powders', *Combustion Science and Technology*, 184: 1993-2007.

Badiola, C., and E.L. Dreizin. 2013. 'Combustion of micron-sized particles of titanium and zirconium ', *Proceedings of the Combustion Institute*, 34: 2237-43.

Badiola, C., R. J. Gill, and E. L. Dreizin. 2011. 'Combustion characteristics of micron-sized aluminum particles in oxygenated environments', *Combustion and Flame*, 158: 2064-70.

Chase, M.W. 1998. 'NIST-JANAF Themochemical Tables, Fourth Edition.', *J. Phys. Chem. Ref. Data, Monograph 9*: 1-1951.

Chen, C., Y. H. Wang, K. Z. Pan, and X. L. Chen. 2009. 'Thermal-characteristic research of boron', *Guti Huojian Jishu/Journal of Solid Rocket Technology*, 32: 663-66.

Chen, D. M., W. H. Hsieh, T. S. Snyder, V. Yang, T. A. Litzinger, and K. K. Kuo. 1991. 'Combustion behavior and thermophysical properties of metal-based solid fuels', *Journal of Propulsion and Power*, 7: 250-57.

Chintersingh, K. L., Q. Nguyen, M. Schoenitz, and E. L. Dreizin. 2016a. 'Combustion of boron particles in products of an air–acetylene flame', *Combustion and Flame*, 172: 194-205.

Chintersingh, K. L., M. Schoenitz, and E. L. Dreizin. 2016. 'Oxidation kinetics and combustion of boron particles with modified surface', *Combustion and Flame*, 173: 288-95.

Chintersingh, K. L., Schoenitz, M., and Dreizin, E. L. 2018. 'Combustion of boron and boron–iron composite particles in different oxidizers', *Combustion and Flame*, 192: 44-58.

Chintersingh, K. L., M. Schoenitz, and E.L. Dreizin. 2017. 'Combustion of boron and boron-iron composite particles in different oxidizers', *Combustion and Flame*, under review

Chintersingh, Kerri-Lee, Quang Nguyen, Mirko Schoenitz, and Edward L. Dreizin. 2016b. 'Combustion of boron particles in products of an air–acetylene flame', *Combustion and Flame*, 172: 194-205.

Clark, B. R., and M. L. Pantoya. 2010. 'The aluminium and iodine pentoxide reaction for the destruction of spore forming bacteria', *Physical Chemistry Chemical Physics*, 12: 12653-57.

Conkling, J.A., and C. Mocella. 2010. *Chemistry of Pyrotechnics: Basic Principles and Theory, Second Edition* (CRC Press).

Corcoran, A. L., S. Wang, Y. Aly, and E. L. Dreizin. 2015. 'Combustion of mechanically alloyed Al·Mg powders in products of a hydrocarbon flame', *Combustion Science and Technology*, 187: 807-25.

Corcoran, A., S. Mercati, H. Nie, M. Milani, L. Montorsi, and E. L. Dreizin. 2013a. 'Combustion of fine aluminum and magnesium powders in water', *Combustion and Flame*, 160: 155-60.

Corcoran, A., Mercati, S., Nie, H., Milani, M., Montorsi, L., and Dreizin, E. L. 2013b. 'Combustion of fine aluminum and magnesium powders in water', *Combustion and Flame*, 160: 2242-50.

Corcoran, A.L., V.K. Hoffmann, and E.L. Dreizin. 2013. 'Aluminum particle combustion in turbulent flames', *Combustion and Flame*, 160: 718-24.

Davis, A. 1963. 'Solid propellants: The combustion of particles of metal ingredients', *Combustion and Flame*, 7: 359-67.

DeLuca, L. T., E. Marchesi, M. Spreafico, A. Reina, F. Maggi, L. Rossettini, A. Bandera, G. Colombo, and B. M. Kosowski. 2010. 'Aggregation versus agglomeration in metallized solid rocket propellants', *International Journal of Energetic Materials and Chemical Propulsion*, 9: 91-105.

Dreizin, E. L. 2000. 'Phase changes in metal combustion', *Progress in Energy and Combustion Science*, 26: 57-78.

Dreizin, E. L. 2003. 'Effect of Phase Changes on Metal-Particle Combustion Processes', *Combustion, Explosion and Shock Waves*, 39: 681-93.

Dreizin, E. L., C. H. Berman, and E. P. Vicenzi. 2000. 'Condensed-phase modifications in magnesium particle combustion in air', *Combustion and Flame*, 122: 30-42.

Dreizin, E.L., and M. Schoenitz. 2009. "Nano-composite energetic powders prepared by arrested reactive milling." In *US Patent 7,524,355*

Eneh, O. C. 2012. 'Biological weapons-agents for life and environmental destruction', *Research Journal of Environmental Toxicology*, 6: 65-87.

Farley, C., and M. Pantoya. 2010. 'Reaction kinetics of nanometric aluminum and iodine pentoxide', *Journal of Thermal Analysis and Calorimetry*, 102: 609-13.

Feng, J., G. Jian, Q. Liu, and M. R. Zachariah. 2013. 'Passivated iodine pentoxide oxidizer for potential biocidal nanoenergetic applications', *ACS Applied Materials and Interfaces*, 5: 8875-80.

Florko, A. V., S. V. Kozitskii, A. N. Pisarenko, and A. M. Matsko. 1986. 'Study of combustion of single magnesium particles at low pressure', *Combustion, Explosion, and Shock Waves*, 22: 159-63.

Foelsche, R. O., R. L. Burton, and H. Krier. 1999. 'Boron particle ignition and combustion at 30-150 ATM', *Combustion and Flame*, 117: 32-58.

Fujii, K., W. Kondo, W. Mizuta, and T. Kumagai. 1977. 'The calcium-iodine cycle for the thermochemical decomposition of water', *International Journal of Hydrogen Energy*, 2: 413-21.

Gaulé, G.K. 2013. *Boron: Volume 2: Preparation, Properties, and Applications* (Springer US).

Glassman, Irvin. 1960. 'Combustion of metals--physical considerations', *Progr. Astron. Rocketry*, 1: 253-8.

Gremyachkin, V. M., A. G. Istratov, and O. I. Leipunskii. 1979. 'Theory of combustion of a boron particle in oxygen in high-temperature environment', *Combustion, Explosion, and Shock Waves*, 15: 691-98.

Grinshpun, S. A., A. Adhikari, C. Li, T. Reponen, M. Yermakov, M. Schoenitz, E. Dreizin, M. Trunov, and S. Mohan. 2010. 'Thermal inactivation of airborne viable Bacillus subtilis spores by short-term exposure in axially heated air flow', *Journal of Aerosol Science*, 41: 352-63.

Grinshpun, S. A., A. Adhikari, M. Yermakov, T. Reponen, E. Dreizin, M. Schoenitz, V. Hoffmann, and S. Zhang. 2012. 'Inactivation of aerosolized Bacillus atrophaeus (BG) endospores and MS2 viruses by combustion of reactive materials', *Environmental Science and Technology*, 46: 7334-41.

Grinshpun, S. A., C. Li, A. Adhikari, M. Yermakov, T. Reponen, M. Schoenitz, E. Dreizin, V. Hoffmann, and M. Trunov. 2010. 'Method for studying survival of airborne viable microorganisms in combustion environments: Development and evaluation', *Aerosol and Air Quality Research*, 10: 414-24.

Grinshpun, S. A., M. Yermakov, R. Indugula, A. Abraham, M. Schoenitz, and E. L. Dreizin. 2017. 'Aluminum-based materials for inactivation of aerosolized spores of Bacillus anthracis surrogates', *Aerosol Science and Technology*, 51: 224-34.

Guo, Y., W. Zhang, X. Zhou, and T. Bao. 2013. 'Magnesium boride sintered as high-energy fuel', *Journal of Thermal Analysis and Calorimetry*, 113: 787-91.

He, C., J. P. Hooper, and J. M. Shreeve. 2016. 'Iodine-Rich Imidazolium Iodate and Periodate Salts: En Route to Single-Based Biocidal Agents', *Inorganic Chemistry*, 55: 12844-50.

He, C., J. Zhang, and J. M. Shreeve. 2013a. 'Dense iodine-rich compounds with low detonation pressures as biocidal agents', *Chemistry - A European Journal*, 19: 7503-09.

He, Chunlin, Jiaheng Zhang, and Jean'ne M. Shreeve. 2013b. 'Dense Iodine-Rich Compounds with Low Detonation Pressures as Biocidal Agents', *Chemistry - A European Journal*, 19: 7503-09.

Henderson, J., A. W. Longbottom, A. M. Milne, J. M. Lightstone, C. Milby, D. Stamatis, F. R. Svingala, A. L. Daniels, M. Bensman, M. Bohmke, and K. Miller. 2015. 'Experiments and Modeling for Biocidal Effects of Explosives', *Propellants, Explosives, Pyrotechnics*, 40: 712-19.

Hobosyan, M. A., A. Kazansky, and K. S. Martirosyan. 2012. "Nanoenergetic composite based on I 2O 5/Al for biological agent defeat." In *Technical Proceedings of the 2012 NSTI Nanotechnology Conference and Expo, NSTI-Nanotech 2012*, 599-602.

Hodgkinson, J., and R. P. Tatam. 2013. 'Optical gas sensing: A review', *Measurement Science and Technology*, 24.

Hsieh, Wen-Hsin, Arie Peretz, I. Te Huang, and Kenneth K. Kuo. 1991. 'Combustion behavior of boron-based BAMO/NMMO fuel-rich solid propellants', *Journal of Propulsion and Power*, 7: 497-504.

Hussmann, B., and M. Pfitzner. 2010. 'Extended combustion model for single boron particles - Part I: Theory', *Combustion and Flame*, 157: 803-21.

Jain, A., K. Joseph, S. Anthonysamy, and G. S. Gupta. 2011. 'Kinetics of oxidation of boron powder', *Thermochimica Acta*, 514: 67-73.

Johnson, Curtis E., and Kelvin T. Higa. 2013. "Iodine-rich biocidal reactive materials." In *Materials Research Society Symposium Proceedings*, 2013.46/1-13/46/6. Boston, MA: Cambridge University Press.

Judprasong, Kunchit, N. Jongjaithet, and Visith Chavasit. 2015. 'Comparison of methods for iodine analysis in foods', *Food Chemistry*, 193.

Karmakar, S., N. Wang, S. Acharya, and K. M. Dooley. 2013. 'Effects of rare-earth oxide catalysts on the ignition and combustion characteristics of boron nanoparticles', *Combustion and Flame,* 160: 3004-14.

King, M. K. 1973. 'Boron particle ignition in hot gas streams', *Combustion Science and Technology*, 8: 255-73.

King, Merrill K. 1972. 'Boron ignition and combustion in air-augmented rocket afterburners ', *Combustion Science and Technology*, 5: 155-64.

King, M. K. 1982. "Ignition and combustion of boron particles and clouds." In *Journal of Spacecraft and Rockets*, 294-306.

Kissinger, H. E. 1957. 'Reaction Kinetics in Differential Thermal Analysis', *Analytical Chemistry*, 29: 1702-06.

Koch, E. C. 2011. *Metal-Fluorocarbon Based Energetic Materials*.

Law, C. K. 1973. 'A Simplified Theoretical Model for the Vapor-Phase Combustion of Metal Particlest', *Combustion Science and Technology*, 7: 197-212.

Law, C. K. 1976. 'Models for Metal Particle Combustion with Extended Flame Zones', *Combustion Science and Technology*, 12: 113-24.

Law, C. K., and F. A. Williams. 1974. 'Combustion of magnesium particles in oxygen-inert atmospheres', *Combustion and Flame*, 22: 383-405.

Legrand, B., M. Marion, C. Chauveau, I. Gökalp, and E. Shafirovich. 2001. 'Ignition and combustion of levitated magnesium and aluminum particles in carbon dioxide', *Combustion Science and Technology*, 165: 151-74.

Liang, D., J. Liu, H. Li, J. Zhou, and K. Cen. 2017. 'Generation and Evolution of Surface Oxide Layer of Amorphous Boron during Thermal Oxidation: A Micro/nanofabricated Slice Measurement', *Propellants, Explosives, Pyrotechnics*, 42: 532-40.

Liu, J. Z., J. F. Xi, W. J. Yang, Y. R. Hu, Y. W. Zhang, Y. Wang, and J. H. Zhou. 2014. 'Effect of magnesium on the burning characteristics of boron particles', *Acta Astronautica*, 96: 89-96.

Liu, Lin-lin, Pei-jin Liu, and Guo-qiang He. 2015. 'Ignition and combustion characteristics of compound of magnesium and boron', *J. Therm. Anal. Calorim.*, 121: 1205-12.

Liu, X., J. Gonzales, M. Schoenitz, and E.L. Dreizin. 2017. 'Effect of purity and surface functionalization on stability and oxidation kinetics of boron powders', *Thermochimica Acta*, 652: 17-23.

Liu, X., M. Schoenitz, and E. L. Dreizin. 2017. 'Boron-based reactive materials with high concentrations of iodine as a biocidal additive', *Chemical Engineering Journal*, 325: 495-501.

Liu, X., Schoenitz, M., and Dreizin, E. L. 2018a. 'Combustion of Mg and composite Mg·S powders in different oxidizers', *Combustion and Flame*, 195: 292-302.

Liu, X., Schoenitz, M., and Dreizin, E. L. 2018b. 'Combustion of Mg and composite Mg·S powders in different oxidizers', *Combustion and Flame*.

Liu, X., Schoenitz, M., and Dreizin, E. L. 2019. 'Preparation, ignition, and combustion of magnesium-calcium iodate reactive nano-composite powders', *Chemical Engineering Journal*, 359: 955-62.

Maček, A. 1973. 'Combustion of boron particles: Experiment and theory', *Symposium (International) on Combustion*, 14: 1401-11.

Maček, A., and J. M. Semple. 1971. 'Combustion of boron particles at elevated pressures', *Symposium (International) on Combustion*, 13: 859-68.

Martirosyan, K. S. 2011. 'Nanoenergetic Gas-Generators: Principles and applications', *Journal of Materials Chemistry*, 21: 9400-05.

McBride, B.J., and S. Gordon. 1996. "Computer Program for Calculation of Complex Chemical Equilibrium Compositions and Applications II. Users Manual and Program Description." In. NASA RP 1311.

Mohan, S., M. A. Trunov, and E. L. Dreizin. 2007. "Heating and ignition of metallic particles by a CO2 Laser." In, 16859-70. Reno, NV.

Monk, I., M. Schoenitz, and E. L. Dreizin. 2016a. 'Modes of Ignition of Powder Layers of Nanocomposite Thermites by Electrostatic Discharge', *Journal of Energetic Materials*: 1-15.

Monk, I., M. Schoenitz, and E.L. Dreizin. 2016b. 'Modes of ignition of powder layers of nanocomposite thermites by electro-static discharge', *Journal of Energetic Materials*: 1-15.

Murzyn, Christopher, Adam Sims, Herman Krier, and Nick Glumac. 2018. 'High speed temperature, pressure, and water vapor concentration measurement in explosive fireballs using tunable diode laser absorption spectroscopy', *Optics and Lasers in Engineering*, 110: 186-92.

Nakpan, W., S. A. Grinshpun, M. Yermakov, R. Indugula, T. Reponen, S. Wang, M. Schoenitz, and E. L. Dreizin. 2018. 'Inactivation of aerosolized surrogates of Bacillus anthracis spores by combustion products of aluminum- and magnesium-based reactive materials: Effect of exposure time', *Aerosol Science and Technology*, 52: 579-87.

Nelson, L. S. 1965. 'Nature of the spearpoints observed during the combustion of zirconium droplets [6]', *Nature*, 207: 741.

Nie, H., Mirko Schoenitz, and Edward L. Dreizin. 2016. 'Oxidation of magnesium: implication for aging and ignition', *The Journal of Physical Chemistry C*, in press.

Overdeep, K. R., K. J. T. Livi, D. J. Allen, N. G. Glumac, and T. P. Weihs. 2015. 'Using magnesium to maximize heat generated by reactive Al/Zr nanolaminates', *Combustion and Flame*, 162: 2855-64.

Oxley, J. C., J. L. Smith, M. M. Porter, M. J. Yekel, and J. A. Canaria. 2017. 'Potential Biocides: Iodine-Producing Pyrotechnics', *Propellants, Explosives, Pyrotechnics*, 42: 960-73.

Pace, K. K., T. A. Jarymowycz, V. Yang, and K. K. Kuo. 1993. "Effect of magnesium-coated boron particles on burning characteristics of solid fuels in high-speed crossflows." In, 332-47. CRC.

Pechkovskii, V., and A. Sofronova. 1965. *Zh. Neorg. Khim.*, 10: 1427-32.

Pivkina, A., P. Ulyanova, Y. Frolov, S. Zavyalov, and J. Schoonman. 2004. 'Nanomaterials for Heterogeneous Combustion', *Propellants, Explosives, Pyrotechnics*, 29: 39-49.

Price, E. W. 1984a. 'Combustion of Metallized Propellants', *Combustion of Metallized Propellants*.

Price, E. W. 1984b. *Combustion of Metallized Propellants* (AIAA: New York).

Quijano, D., A. L. Corcoran, and E. L. Dreizin. 2015. 'Combustion of Mechanically Alloyed Aluminum-Magnesium Powders in Steam', *Propellants, Explosives, Pyrotechnics,* 40: 749-54.

Rosenband, V., and A. Gany. 2011. 'High-reactivity aluminum powders', *International Journal of Energetic Materials and Chemical Propulsion,* 10: 19-32.

Ruz-Nuglo, F., and L. J. Groven. 2015a. "Combustion Characteristics of Calcium Iodate Based Biocidal Formulations." In *2015 AIChE Annual Meeting*. Salt Lake City, UT: AIChE.

Ruz-Nuglo, F., and L. J. Groven. 2015b. 'Combustion Characteristics of Calcium Iodate Based Biocidal Formulations', *2015 AIChE Annual Meeting*.

Samsonov, G.V., V.I. Matkovich, P. Hagenmuller, and T. Lundstrom. 2012. *Boron and Refractory Borides* (Springer Berlin Heidelberg).

Santhanam, P. R., and E. L. Dreizin. 2012. 'Predicting conditions for scaled-up manufacturing of materials prepared by ball milling', *Powder Technology*, 201: 401-11.

Santhanam, P. R., V. K. Hoffmann, M. A. Trunov, and E. L. Dreizin. 2010. 'Characteristics of aluminum combustion obtained from constant-volume explosion experiments', *Combustion Science and Technology*, 182: 904-21.

Sevim, Fatih, Fatih Demir, Murat Bilen, and Hüseyin Okur. 2006. 'Kinetic analysis of thermal decomposition of boric acid from thermogravimetric data', *Korean Journal of Chemical Engineering*, 23: 736-40.

Shoshin, Y. L., M. A. Trunov, X. Zhu, M. Schoenitz, and E. L. Dreizin. 2006a. 'Ignition of aluminum-rich Al-Ti mechanical alloys in air', *Combustion and Flame*, 144: 688-97.

Shoshin, Yuriy L., Mikhaylo A. Trunov, Xiaoying Zhu, Mirko Schoenitz, and Edward L. Dreizin. 2006b. 'Ignition of aluminum-rich Al–Ti mechanical alloys in air', *Combustion and Flame,* 144: 688-97.

Smith, D. K., J. McCollum, and M. L. Pantoya. 2016. 'Effect of environment on iodine oxidation state and reactivity with aluminum', *Physical Chemistry Chemical Physics*, 18: 11243-50.

Sullivan, K. T., N. W. Piekiel, S. Chowdhury, C. Wu, M. R. Zachariah, and C. E. Johnson. 2011a. 'Ignition and combustion characteristics of nanoscale Al/AgIO3: A potential energetic biocidal system', *Combustion Science and Technology*, 183: 285-302.

Sullivan, K. T., N. W. Piekiel, S. Chowdhury, C. Wu, M. R. Zachariah, and C. E. Johnson. 2011b. 'Ignition and combustion characteristics of nanoscale Al/AgIO 3: A potential energetic biocidal system', *Combustion Science and Technology,* 183: 285-302.

Sundaram, D., V. Yang, and R. A. Yetter. 2017. 'Metal-based nanoenergetic materials: Synthesis, properties, and applications', *Progress in Energy and Combustion Science,* 61: 293-365.

Sundaram, V., K. V. Logan, and R. F. Speyer. 1997. 'Reaction path in the magnesium thermite reaction to synthesize titanium diboride', *Journal of Materials Research*, 12: 2657-64.

Ulas, A., K. K. Kuo, and C. Gotzmer. 2001. 'Ignition and combustion of boron particles in fluorine-containing environments', *Combustion and Flame*, 127: 1935-57.

Valov, A. E., Yu A. Kustov, and V. I. Shevtsov. 1994. 'Spectroscopic study of the combustion of solitary magnesium particles in air and in carbon dioxide', *Combustion, Explosion, and Shock Waves,* 30: 431-36.

Vo, T. T., J. Zhang, D. A. Parrish, B. Twamley, and J. M. Shreeve. 2013. 'New roles for 1,1-diamino-2,2-dinitroethene (FOX-7): Halogenated FOX-7 and azo-bis(diahaloFOX) as energetic materials and oxidizers', *Journal of the American Chemical Society*, 135: 11787-90.

Vyazovkin, S. 2001. 'Modification of the Integral Isoconversional Method to Account for Variation in the Activation Energy', *Journal of Computational Chemistry*, 22: 178-83.

Vyazovkin, S., A. K. Burnham, J. M. Criado, L. A. Pérez-Maqueda, C. Popescu, and N. Sbirrazzuoli. 2011. 'ICTAC Kinetics Committee recommendations for performing kinetic computations on thermal analysis data', *Thermochimica Acta*, 520: 1-19.

Vyazovkin, S., and C. A. Wight. 1999. 'Model-free and model-fitting approaches to kinetic analysis of isothermal and nonisothermal data', *Thermochimica Acta*, 340-341: 53-68.

Wang, H., G. Jian, W. Zhou, J. B. DeLisio, V. T. Lee, and M. R. Zachariah. 2015. 'Metal Iodate-Based Energetic Composites and Their Combustion and Biocidal Performance', *ACS Applied Materials and Interfaces*, 7: 17363-70.

Wang, H., D. J. Kline, M. Rehwoldt, and M. R. Zachariah. 2018. 'Ignition and Combustion Characterization of Ca(IO3)2-based Pyrotechnic Composites with B, Al, and Ti', *Propellants, Explosives, Pyrotechnics*, 43: 977-85.

Wang, S., A. Abraham, Z. Zhong, M. Schoenitz, and E. L. Dreizin. 2016. 'Ignition and combustion of boron-based Al·B·I2 and Mg·B·I2 composites', *Chemical Engineering Journal*, 293: 112-17.

Wang, S., X. Liu, M. Schoenitz, and E.L. Dreizin. 2017a. 'Nanocomposite Thermites with Calcium Iodate Oxidizer', *Propellants Explosives Pyrotechnics*, 42: 284-92.

Wang, S., S. Mohan, and E. L. Dreizin. 2016. 'Effect of flow conditions on burn rates of metal particles', *Combustion and Flame*, 168: 10-19.

Wang, S., M. Schoenitz, and E. L. Dreizin. 2017. 'Combustion of Boron and Boron-Containing Reactive Composites in Laminar and Turbulent Air Flows', *Combustion Science and Technology*, 189: 683-97.

Wang, S., M. Schoenitz, S. A. Grinshpun, M. Yermakov, and E. L. Dreizin. 2018. 'Biocidal effectiveness of combustion products of iodine-bearing reactive materials against aerosolized bacterial spores', *Journal of Aerosol Science*, 116: 106-15.

Wang, Song, Amy L. Corcoran, and Edward L. Dreizin. 2015. 'Combustion of magnesium powders in products of an air/acetylene flame', *Combustion and Flame*, 162: 1316-25.

Wang, Song, Xinhang Liu, Mirko Schoenitz, and Edward L. Dreizin. 2017b. 'Nanocomposite Thermites with Calcium Iodate Oxidizer', *Propellants, Explosives, Pyrotechnics*, 42: 284-92.

Ward, T. S., W. Chen, M. Schoenitz, R. N. Dave, and E. L. Dreizin. 2005. 'A study of mechanical alloying processes using reactive milling and discrete element modeling', *Acta Materialia*, 53: 2909-18.

Ward, T. S., M. A. Trunov, M. Schoenitz, and E. L. Dreizin. 2006a. 'Experimental methodology and heat transfer model for identification of ignition kinetics of powdered fuels', *International Journal of Heat and Mass Transfer*, 49: 4943-54.

Ward, Trent S., Mikhaylo A. Trunov, Mirko Schoenitz, and Edward L. Dreizin. 2006b. 'Experimental methodology and heat transfer model for identification of ignition kinetics of powdered fuels', *International Journal of Heat and Mass Transfer*, 49: 4943-54.

Williams, R. A., J. V. Patel, and E. L. Dreizin. 2014. 'Ignition of fully dense nanocomposite thermite powders by an electric spark', *Journal of Propulsion and Power*, 30: 765-74.

Wu, T., A. Sybing, X. Wang, and M. R. Zachariah. 2017. 'Aerosol synthesis of phase pure iodine/iodic biocide microparticles', *Journal of Materials Research*, 32: 890-96.

Xi, J., J. Liu, Y. Wang, D. Liang, H. Li, and J. Zhou. 2014. 'Role of oxalic acid in promoting ignition and combustion of boron: An experimental and theoretical study', *Propellants, Explosives, Pyrotechnics*, 39: 844-51.

Xi, J., J. Liu, Y. Wang, D. Liang, and J. Zhou. 2014. 'Effect of metal hydrides on the burning characteristics of boron', *Thermochimica Acta*, 597: 58-64.

Yeh, C. L., and K. K. Kuo. 1996. 'Ignition and combustion of boron particles', *Progress in Energy and Combustion Science*, 22: 511-41.

Yeh, C. L., K. K. Kuo, M. Klimkiewicz, and P. W. Brown. 1997. 'Environmental scanning electron microscopy studies of diffusion mechanism of boron particle combustion', *Scanning*, 19: 114-18.

Yetter, R. A., G. A. Risha, and S. F. Son. 2009. 'Metal particle combustion and nanotechnology', *Proceedings of the Combustion Institute*, 32 II: 1819-38.

Young, G., C. A. Stoltz, B. P. Mason, V. S. Joshi, R. H. Johansson, T. L. Connell Jr, G. A. Risha, and R. A. Yetter. 2012. 'Combustion of PTFE-Boron compositions for propulsion applications', *International Journal of Energetic Materials and Chemical Propulsion*, 11: 451-71.

Young, G., C. A. Stoltz, D. H. Mayo, C. W. Roberts, and C. L. Milby. 2013. 'Combustion behavior of solid fuels based on PTFE/boron mixtures', *Combustion Science and Technology*, 185: 1261-80.

Young, G., K. Sullivan, M. R. Zachariah, and K. Yu. 2009. 'Combustion characteristics of boron nanoparticles', *Combustion and Flame*, 156: 322-33.

Zhang, S., C. Badiola, M. Schoenitz, and E. L. Dreizin. 2012. 'Oxidation, ignition, and combustion of Al·I 2 composite powders', *Combustion and Flame*, 159: 1980-86.

Zhang, S., M. Schoenitz, and E. L. Dreizin. 2010a. 'Iodine release, oxidation, and ignition of mechanically alloyed Al-I composites', *Journal of Physical Chemistry C*, 114: 19653-59.

Zhang, S., M. Schoenitz, and E. L. Dreizin. 2010b. 'Mechanically alloyed Al-I composite materials', *Journal of Physics and Chemistry of Solids*, 71: 1213-20.